Emittance related topics for fourth generation storage ring light sources

Breunlin, Jonas

2016

Emittance Related Topics for Fourth Generation Storage Ring Light Sources

Jonas Breunlin

Doctoral Thesis
2016

LUND
UNIVERSITY

EMITTANCE RELATED TOPICS FOR
FOURTH GENERATION STORAGE RING LIGHT SOURCES

Printed in Sweden by Tryckeriet i E-huset, Lund, 2016

Cover: MAX IV diagnostic beamline mirror holder. Design by K. Åhnberg.
(photo by J. Breunlin)

MAX IV Laboratory, Lund University
P.O. Box 118
SE–221 00 Lund
Sweden

http://www.maxiv.se

ISBN 978-91-7623-952-0 (printed version)

ISBN 978-91-7623-953-7 (electronic version)

To Rosemarie and Rudolf Breunlin.

ABSTRACT

In this thesis several aspects related to a new generation of storage ring light sources are discussed. Due to a reduction of electron beam emittance, fourth generation storage rings provide synchrotron radiation sources close to the diffraction limit at X-ray wavelengths. This results in a significant increase in photon brightness that is beneficial in a variety of synchrotron radiation based experiments. The MAX IV Laboratory in Lund, Sweden, operates the first storage ring light source of the fourth generation. Its 3 GeV storage ring has a circumference of 528 m and employs a multibend achromat lattice with a horizontal electron beam emittance of 0.33 nm rad.

Beam size and emittance diagnostics of ultralow horizontal and vertical emittance electron beams can be achieved by focusing synchrotron radiation from dipole magnets, to form an image of the beam. When imaging in the visible and near-visible spectral ranges, diffraction and emission effects are dominant. The presented refined methods, however, make it possible and even beneficial to deduce small electron beam sizes from this radiation. Diagnostics of the longitudinal charge distribution in the bunch, based on time-resolved measurements of synchrotron radiation, are of special interest, since bunch lengthening with passive harmonic rf cavities is an essential ingredient in the concept of the storage ring, extending Touschek lifetime and mitigating the effects of intrabeam scattering.

The horizontal emittance in the MAX IV 3 GeV storage ring will lead, after correction of coupling and minimization of vertical dispersion, to a very low vertical emittance, lower than what might be requested by synchrotron radiation experimentalists. Operating with the negative consequences of a too low emittance such as a Touschek lifetime shorter than necessary and an increased intrabeam scattering can, however, be avoided if the vertical emittance is adjusted to a desired level in a controlled way. A scheme is introduced that excites vertical emittance by vertical dispersion while maintaining small source sizes for synchrotron radiation production in the insertion devices, and restores Touschek lifetime.

POPULÄRVETENSKAPLIG SAMMANFATTNING

Vi vet att laddade partiklar sänder ut elektromagnetisk strålning då de tvingas följa en krökt bana. Denna strålning kallas synkrotronstrålning, och upptäcktes i mitten av 1900-talet. Sedan dess har denna typ av strålning funnit tillämpningar inom flera forskningsområden såsom kemi, biologi, medicin och materialvetenskap. För att uppfylla de växande kraven på vissa strålningsegenskaper, är partikelacceleratorer, designade att producera synkrotronljus, under ständig utveckling. Med MAX IV Laboratoriet i Lund, Sverige, och dess 3 GeV lagringsring synkrotronljuskälla, har ett koncept som reducerar elektronstrålens emittans avsevärt, för första gången realiserats. En låg emittans är en viktig parameter, eftersom den möjliggör för forskarna att fokusera synkrotronstrålningen i hög intensitet på ett litet prov. Denna avhandling diskuterar flera utmaningar som uppträder på acceleratorsidan när emittansen i lagringsringen reduceras såsom vid MAX IV anläggningen.

Radiofrekvenskaviteter förser den lagrade elektronstrålen med energi. De harmoniska kaviteterna i MAX IV acceleratorerna har istället till uppgift att sträcka ut elektronklungorna i lagringsringarna, vilket är ett väsentligt krav för att kunna uppfylla designparametrarna. Den resulterande longitudinella formen på elektronklungorna detekteras med hjälp av synkrotronstrålningen i ett diagnostikstrålrör.

Synkrotronstrålningen innehåller också information om storlek och emittans på elektronstrålen. För detta ändamål fokuseras den synliga delen av strålningen, med en lins i diagnostikstrålröret, för att skapa en bild av elektronstrålen. På grund av den lilla strålstorleken, står själva utsändningsprocessen och diffraktion, för de dominanta effekterna i bilden. Ändå presenteras här metoder som möjliggör härledning av elektronstrålens storlek och slutligen dess emittans.

En mycket låg vertikal emittans för med sig nackdelar, såsom en ökad förlust-takt av elektroner från strålen och även en ökad horisontell emittans. Detta beror på växelverkningar mellan elektronerna i

en klunga. En tillvägagångssätt presenteras därför som ökar vertikala emittansen på ett kontrollerat och omvändbart sätt, för att kunna möta kraven från en särskild vetenskaplig applikation med synkrotronljusstrålning, och på det viset undvika de förut nämnda onödiga nackdelarna.

POPULAR SCIENTIFIC INTRODUCTION

Charged particles are known to emit radiation when traveling on a curved path. This radiation is called synchrotron radiation and was discovered in a particle accelerator in the middle of the 20th century. Since then, this radiation has found application in various research fields in chemistry, biology, medicine and material science. To fulfill the growing requirements towards radiation source properties, particle accelerators, designed as synchrotron light sources, are under continuous development. With the MAX IV Laboratory in Lund, Sweden, and its 3 GeV storage ring light source, a concept that reduces the electron beam emittance significantly, is employed for the first time. A low emittance is an important parameter, since it allows scientists to focus the synchrotron radiation at high intensities onto small samples. It leads, however, to several challenges on the particle accelerator side of which some are discussed in this work.

Radio frequency cavities provide energy to the circulating electron beam. The harmonic cavities in the MAX IV accelerators, however, stretch the electron packages circulating in the storage ring, which is an essential requirement to fulfill design parameters. The resulting longitudinal shape of the electron packages is detected from the emitted synchrotron radiation in a diagnostic beamline.

Synchrotron radiation carries information about the transverse size and emittance of the electron beam as well. For this purpose the visible and near-visible part of the radiation spectrum is focused by a lens in the diagnostic beamline, creating an image of the electron beam. Due to the small size of the beam, however, diffraction effects from the emission process of the radiation dominate the image. Methods are presented that allow the deduction of the electron beam size, and eventually the beam emittance, from such diffraction dominated images.

A very low vertical emittance comes with downsides such as an increased loss rate of electrons from the beam or even an increased horizontal emittance. This is due to interaction of electrons within the same bunch. A scheme is presented that increases the vertical beam emittance in a controlled and reversible way, to meet the re-

quirements of the particular scientific application of the synchrotron radiation, and thereby avoiding the aforementioned unnecessary drawbacks.

LIST OF PUBLICATIONS

This thesis is based on the following papers, which will be referred to by their Roman numerals in the text.

I **Improving Touschek lifetime in ultralow-emittance lattices through systematic application of successive closed vertical dispersion bumps**
J. Breunlin, S. C. Leemann, and Å. Andersson.
Physical Review Accelerators and Beams **19**, 060701 (2016).

II **Equilibrium bunch density distribution with passive harmonic cavities in a storage ring**
P. F. Tavares, Å. Andersson, A. Hansson, and J. Breunlin.
Physical Review Special Topics – Accelerators and Beams **17**, 064401 (2014).

III **Methods for measuring sub-pm rad vertical emittance at the Swiss Light Source**
J. Breunlin, Å. Andersson, N. Milas, Á. Saá Hernández, and V. Schlott.
Nuclear Instruments and Methods in Physics Research A **803**, 55-64 (2015).

IV **Emittance diagnostics at the MAX IV 3 GeV storage ring**
J. Breunlin, and Å. Andersson.
In Proceedings of the 7th International Particle Accelerator Conference, IPAC 2016, Busan, Korea. **WEPOW034**, 2908-2910 (2016).

ADDITIONAL PUBLICATIONS

Other work I contributed to resulted in the following publications

1 **Status of the new beam size monitor at SLS**
J. Breunlin, Å. Andersson, Á. Saá Hernández, M. Rohrer, V. Schlott, A. Streun, and N. Milas.
In Proceedings of the 5th International Particle Accelerator Conference IPAC 2014, Dresden, Germany. **THPME169**, 3662-3664 (2014).

2 **Ultra-low vertical beam size instrumentation and emittance determination at the Swiss Light Source**
Á. Saá Hernández, M. Aiba, M. Böge, N. Milas, M. Rohrer, V. Schlott, A. Streun, Å. Andersson, and J. Breunlin.
Beam Dynamics Newsletter No. **62**, 208-221. International Commitee for Future Accelerators ICFA, Fermilab, USA (2013).

3 **The new SLS beam size monitor, first results**
Á. Saá Hernández, N. Milas, M. Rohrer, V. Schlott, A. Streun, Å. Andersson, and J. Breunlin.
In Proceedings of the 4th International Particle Accelerator Conference IPAC 2013, Shanghai, China. **MOPWA041**, 759-761 (2013).

4 **Measuring and improving the momentum acceptance and horizontal acceptance at MAX III**
A. Hansson, Å. Andersson, J. Breunlin, G. Skripka, and E. J. Wallén.
In Proceedings of the 4th International Particle Accelerator Conference IPAC 2013, Shanghai, China. **MOPEA056**, 205-207 (2013).

5 **Studies of the electron beam lifetime at MAX III**
A. Hansson, Å. Andersson, J. Breunlin, G. Skripka, and E. J. Wallén.
In Proceedings of the 4th International Particle Accelerator Conference IPAC 2013, Shanghai, China. **MOPEA057**, 208-210 (2013).

6 **Commissioning experience and first results from the new SLS beam size monitor**
V. Schlott, M. Rohrer, Á. Saá Hernández, A. Streun, Å. Andersson and J. Breunlin, N. Milas,.
In Proceedings of the IBIC 2013, Oxford, UK. **TUPF09**, 519-521 (2013).

7 **Design and expected performance of the new SLS beam size monitor**
N. Milas, M. Rohrer, Á. Saá Hernández, V. Schlott, A. Streun, Å. Andersson and J. Breunlin.
In Proceedings of the IBIC 2012, Tsukuba, Japan. **TUCC03**, 307-309 (2012).

ABBREVIATIONS

BW	bandwidth
CCD	charge-coupled device
FBSF	filament beam spread function
FEL	free electron laser
FWHM	full width half maximum
IBS	intrabeam scattering
ID	insertion device
IR	infrared
MBA	multibend achromat
rf	radio frequency
rms	root mean square
SLS	Swiss Light Source
SPF	Short Pulse Facility
SR	synchrotron radiation
SRW	synchrotron radiation workshop
UV	ultraviolet
VUV	vacuum-ultraviolet

CONTENTS

Papers

INTRODUCTION AND MOTIVATION

Towards the synchrotron storage ring

Particle accelerators have been serving scientists of various disciplines as research tools for almost a century. With the discovery of the atomic nucleus and natural radioactive decay, the demand for artificially created highly energetic particles started. Early particle accelerators were of the electrostatic type, where a high electric potential difference is used to accelerate charged particles. In 1932 the Cockcroft-Walton accelerator achieved a potential of 800 kV to accelerate protons [Cockcroft and Walton, 1932] and enabled the first induced nuclear reaction.

In a linear accelerator, an accelerating electric field can be traversed only once, and the maximum available voltage (and therefore energy gain) is technically limited. This led to developments of repeated acceleration, either in linear, staged accelerators (for example [Alvarez, 1946]), or in circular accelerators such as the *cyclotron* [Lawrence and Edlefsen, 1930], where a magnetic dipole field bends the particle trajectory like a spiral, and therefore the same (alternating) voltage can be used several times for acceleration. The achievable energy in a cyclotron type of accelerator is limited by the magnetic field, required to bend the beam, but also by the fact that the synchronous condition of particle motion through one half of the cyclotron, and the time-dependent accelerating voltage, desynchronize. Therefore, either special magnet designs (the *sector cyclotron*) or a system that adjusts the frequency of the accelerating voltage to match the varying revolution frequency of the particles (the *synchrocyclotron*), is required.

One further development of the circular accelerator is the *synchrotron*, where particles follow a well-defined orbit instead of a spiral. The time in which a particle is accelerated in a synchrotron is therefore not limited by design. To maintain a constant orbit, the magnetic field that bends the particle trajectory must be increased *synchronously* with rising particle energy. It was on such an early synchrotron by General Electric, accelerating electrons up to 70 MeV, that *synchrotron radiation* (SR) was observed for the first time [Elder et al., 1947], see Figure 1.

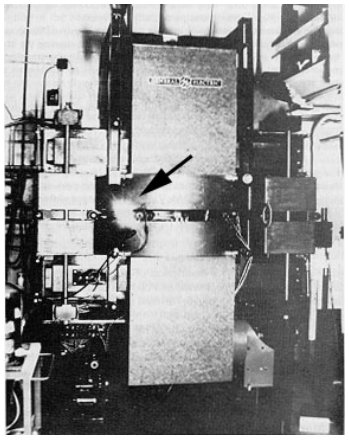

Figure 1. *Photograph of SR from the General Electric 70 MeV synchrotron. The arrow indicates the bright spot between the magnets.*

Such early synchrotrons required relatively large apertures (and therefore magnets) because the particle beam size and divergence were large, limited only by the so-called *weak focusing*. A milestone on the way to the modern synchrotron was therefore the discovery of *strong focusing* by quadrupole magnets [Christofilos, 1950][Courant et al., 1952]. A quadrupole magnet provides a magnetic field configuration that has a similar effect to a beam of charged particles as a lens to a light beam, with the important difference that a quadrupole magnet focuses in one plane, but defocuses in the other. With an adequate combination of focusing and defocusing quadrupoles, however, a net focusing effect can be achieved in both planes.

Strong focusing with quadrupoles exceeds weak focusing effects by orders of magnitude, and reduces therefore the transverse beam dimensions, allowing for compact vacuum chambers and magnets. Together with the longitudinal *phase focusing*, this paved the way for synchrotrons in which particle beams with high energies and intensities, but low emittances, circulate for hours, the so-called *storage rings*.

Particle accelerators as light sources

Particle colliders, of which some are synchrotrons, are built for studies on particle interaction at high energies. In the early days, the SR from the dipole magnets of such electron-electron or electron-positron colliders was used parasitically for scientific purposes. Soon, SR became a research tool in many areas, such as material science, crystallography, chemistry, biology and medical research. The parasitic operation marks the *first generation* of synchrotron light sources, followed by a *second generation* with synchrotron storage rings built exclusively for the production of radiation from bending magnets.

Synchrotron light sources of the *third generation* have been developed further towards low electron beam emittance and are optimized for SR production in dedicated *insertion devices* (IDs), magnetic structures inserted into straight sections of the storage ring for the purpose of SR production at high brightness. Insertion devices consist of a sequence of dipole magnets of opposite polarity causing no net deflection of the electron beam. The characteristics of the SR emitted from IDs depends largely on the ID design, which is led by the requirements of SR experiments, rather than by the dynamics of the stored electron beam. Research facilities operating SR sources of the third generation exist worldwide, operating at energies around 6 GeV (for example SPring-8 in Japan, the Advanced Photon Source (APS) in USA and ESRF in France) or at medium energies up to 3 GeV (for example the Advanced Light Source (ALS) in USA and the Swiss Light Source (SLS) in Switzerland).

The fourth generation of SR sources is the linear accelerator

driven *Free Electron Laser* (FEL). In an FEL, radiation is generated by short electron bunches and long undulators, allowing for an electron-photon interaction and coherent SR production [Schmüser et al., 2009].

The next generation of storage ring light sources

It has been known for about two decades that the horizontal emittance in a storage ring can be decreased by employing a larger number of bending magnets, each with a smaller beam deflection. The *multibend achromat* (MBA) lattice [Einfeld and Plesko, 1993] [Joho et al., 1994] [Einfeld et al., 1995] [Einfeld et al., 2014] employs multiple, relatively shallow bends and strong quadrupole magnets for refocusing in between, to suppress dispersion and therefore lowering the emittance. Matching sections towards both ends of the sequence of bending magnets (that is also called the *arc*) ensures, that the dispersion in the straight sections, where IDs are located, is zero (which makes the arc an *achromat*). The emittance in a MBA lattice can easily be one order of magnitude lower than in a comparable synchrotron light sources of the third generation with two (double-bend achromat) or three (tipple-bend achromat) bending magnets per achromat, justifying the naming *fourth generation storage ring light source* [Hettel, 2014].

The MBA lattice, however, comes with design challenges towards accelerator hardware and beam dynamics that needed to be solved before constructing a storage ring of this type. Small apertures of the vacuum system require distributed pumping, for which the inside of the vacuum tubes is coated with a non-evaporable getter (NEG) material [Al-Dmour et al., 2014]. Small vacuum chamber apertures, together with progresses in the field of magnet technology in terms of magnet performance and manufacturing precision [Johansson et al., 2014], make sufficiently high quadrupole and sextupole gradients feasible, which are a requirement of the MBA lattice.

High quadrupole gradients lead to considerable negative chromaticities, which need to be corrected to achieve a stable electron beam. Chromaticity correction with chromatic sextupole magnets, however, introduces nonlinearities in the dynamics of the electron beam. Only due to a detailed understanding and precise simulation of the nonlinear beam dynamics, countermeasures can be met and a practical design for a fourth generation storage ring light source becomes feasible. MBA lattices for synchrotron light sources have been initiated by the MAX IV Laboratory with its 7-bend achromat storage ring at an electron energy of 3 GeV. The Sirius light source, employing a 5-bend achromat lattice, is under construction at the Brazilian Synchrotron Light Laboratory (LNLS) [Liu et al., 2014]. Furthermore, upgrade plans have been developed for numerous existing light source facilities [Steier, 2014] [Biasci et al., 2014].

In a synchrotron light source the electron beam emittance is an important criterion, since it has significant influence on the *brightness* of the produced radiation, that is the number of photons emitted per second, per mm^2, per mrad^2 and per 0.1% of the bandwidth of the radiation. Today's development in the field is going towards *diffraction limited* light sources in the hard X-ray regime, which means that the electron beam emittance is negligible compared to (or at least approximately equal to) the intrinsic photon beam emittance from the ID [Kim, 1995]. Consequently, diffraction limited operation at a wavelength of 1 Å requires an electron beam emittance of 8 pm rad. In the vertical plane this is already achievable with third generation light sources, while the horizontal emittance in such machines is typically in the few nm rad range.

The Swiss Light Source (SLS) at the Paul Scherrer Institute is a typical third generation light source at a medium electron energy of 2.4 GeV. Due to precise alignment and coupling reduction, the vertical emittance has been decreased to the few pm rad level [Aiba et al., 2012]. Electron beam diagnostics on beams with such low vertical emittance is challenging, but feasible with methods of SR imaging, as shown in [Andersson et al., 2008] and in Paper **III**. An introduction to beam size measurements with visible and near-visible SR is given in Chapter 5 of this thesis.

The MAX IV Laboratory

Inaugurated in 2016, the MAX IV Laboratory in Lund, Sweden, is a facility for SR based science [Tavares et al., 2014]. It hosts a fourth generation 3 GeV storage ring that is optimized for the production of hard X-rays at high brightness, whereas the soft X-ray and vacuum-ultraviolet (VUV) spectral regime is covered by a 1.5 GeV storage ring light source of the third generation. A 3 GeV linear accelerator [Thorin et al., 2014] serves as a full-energy injector to both storage rings, and delivers short electron bunches to the Short Pulse Facility (SPF) where X-ray pulses of 100 fs length are generated [Werin et al., 2009], while upgrade plans to a FEL exist [Curbis et al., 2013].

The 3 GeV storage ring employs a MBA lattice with seven bends per achromat, repeated in 20 cells, with a total circumference of 528 m [Leemann et al., 2009]. A horizontal emittance of 0.33 nm rad is reached with the *bare lattice* (that means without any IDs), which will decrease to 0.2 nm rad when fully equipped. As a consequence, horizontal beam size and beam emittance measurements are challenging and require dedicated diagnostics. A diagnostic beamline, the first of two that will be installed, constructed for imaging with ultraviolet to infrared SR, resolves the 25 µm horizontal beam size and reveals features of SR that have not been observed before in experiment. This is presented in Paper **IV** and a few basic principles are introduced in Chapter 5.

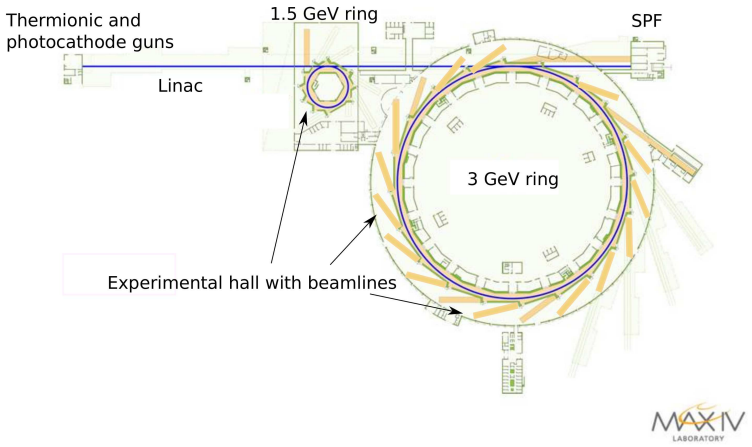

Figure 2. *Schematic layout of the MAX IV Laboratory.* *Drawing by Johnny Kvistholm.*

Narrow vacuum chambers, a requirement of high magnet gradients, increase the risk of collective instabilities due to interactions with the vacuum chamber walls, which limit the maximum stored current. To reach the design current of 500 mA, passive harmonic radio frequency (rf) cavities are an essential ingredient of the 3 GeV storage ring. By elongating the electron bunches with harmonic cavities, the charge density is reduced. This alleviates intrabeam scattering (IBS) and increases the Touschek lifetime to projected values. Both Touschek scattering and IBS are briefly introduced in Chapter 4. Furthermore, harmonic cavities increase the incoherent synchrotron tune spread, which enhances damping of coherent instabilities. The operation mode of passive harmonic cavities and measurements of the bunch shape affected by elongation, are presented in Paper **II**, whereas some of the basic principles of the longitudinal particle motion in an electron storage ring are introduced in Chapter 2.

The vertical emittance in an ultralow-emittance storage ring can become impractically small, even for moderate emittance ratios. Operating at a vertical emittance lower than required for SR production, however, reduces the *Touschek lifetime* unnecessarily and can increase the 6-dimensional emittance due to IBS. A scheme is therefore presented in Paper **I** that, applied after the minimization of vertical dispersion and betatron coupling, increases the vertical emittance in a controlled fashion. By applying pairs of skew quadrupoles, vertical dispersion and betatron coupling bumps are opened and closed within the arcs of the storage ring, in order to maintain good source properties for IDs in the straight sections. The application

of this scheme to the MAX IV 3 GeV storage ring in simulation, together with the expected Touschek lifetime gain from vertical emittance increase, is presented in Paper **I**. Chapter 1 of this thesis gives a brief introduction to the principles of transverse beam dynamics with a focus on dispersion and coupling and on the definition of electron beam and lattice parameters. The mechanisms of excitation and damping of the electron beam by SR, eventually leading to an equilibrium emittance, are described in Chapter 3.

This work is summarized in Chapter 6 and an outlook on possible future developments in connection with this work is given.

CHAPTER 1

TRANSVERSE BEAM DYNAMICS

In this chapter, a brief introduction to the concepts used in the description of transverse particle motion in an accelerator is given. Based on Hamiltonian mechanics and equations of motion, presented in the form of transfer maps, this chapter shall give an idea of how particle dynamics is treated numerically in the simulation code, Tracy-3 [Bengtsson], used for this work. Starting from linear beam dynamics and dispersion, a definition of the transverse beam dimensions, relevant for the transverse beam diagnostics presented in Papers **III** and **IV**, is given. In the context of Paper **I**, a general concept of coupled particle motion and aspects of nonlinear dynamics and lattice imperfections, are briefly introduced in the end of this chapter.

1.1 Hamiltonian for a particle in an accelerator

In general, the dynamics of a particle in an accelerator is determined by electromagnetic fields provided by various accelerator components (mainly magnets and rf cavities). Finding equations of motion under consideration of such fields, and solving them, will therefore allow to calculate the trajectory of the particle. The Hamiltonian formalism of mechanics [Goldstein et al., 2002] is particularly useful to describe the dynamics in an accelerator, since it gives access to conserved quantities in particle motion – the beam emittances.

In principle, the effect of electric and magnetic fields on a charged particle is described by the Lorentz force

$$\boldsymbol{F} = q(\boldsymbol{E} + \boldsymbol{v} \times \boldsymbol{B}). \tag{1.1}$$

Particles in high energy accelerators (and especially in the case of electrons), however, move with relativistic velocities. For an adequate description of particle motion in an accelerator, a few concepts of special relativity are needed. The total energy E of a particle in the

absence of fields is, in relation to its momentum $\boldsymbol{p}$, given by

$$E^2 = \boldsymbol{p}^2 c^2 + m^2 c^4, \tag{1.2}$$

where c is the vacuum speed of light and m is the mass of the particle. The total energy and momentum can also be formulated as

$$E = \gamma m c^2 \text{ and } \boldsymbol{p} = \boldsymbol{\beta}\gamma m c. \tag{1.3}$$

Here the relativistic $\boldsymbol{\beta}$ is related to the particle velocity as $\boldsymbol{\beta} = \boldsymbol{v}/c$ and the Lorentz factor is defined as

$$\gamma = \frac{1}{\sqrt{1-\beta^2}}. \tag{1.4}$$

We then introduce the scalar potential Φ and the vector potential $\boldsymbol{A}$, that are related to the electric field $\boldsymbol{E}$ and the magnetic flux density $\boldsymbol{B}$ by

$$\boldsymbol{E} = -\nabla\Phi - \frac{\partial \boldsymbol{A}}{\partial t} \text{ and } \boldsymbol{B} = \nabla \times \boldsymbol{A}. \tag{1.5}$$

In the presence of electromagnetic fields, Eqs. 1.3 are modified to

$$E = \gamma m c^2 + q\Phi \text{ and } \boldsymbol{p} = \boldsymbol{\beta}\gamma m c + q\boldsymbol{A}, \tag{1.6}$$

and the Hamiltonian for particle motion at relativistic velocities in an electromagnetic field becomes

$$H = c\sqrt{\left(\boldsymbol{p} - q\boldsymbol{A}\right)^2 + m^2 c^2} + q\Phi. \tag{1.7}$$

The above equation is in principle sufficient to describe single particle dynamics in an accelerator. Finding equations of motion (and understanding them) can, however, be simplified significantly by the following few modifications:

The Hamiltonian in Eq. 1.7 treats time as the independent variable. In practice, when considering a sequence of magnets in an accelerator beamline, it is much more convenient to use a variable that represents the distance along the particle trajectory, at which an accelerator element ends or begins, instead of calculating the time at which the particle reaches the element. This distance along the trajectory is denoted with s.

The equations of motion even for simple accelerator components are usually too complex to derive exact solutions for. Approximations in the form of power series of the dynamical variables are therefore required, even when using numerical algorithms. By truncating the power series, the equations of motion can be solved to a certain order. Truncating, for example, after the first order term will lead to linear approximation of particle dynamics, on which most of this chapter is based. For an effective power series, the variables describing

position and momentum of a particle should remain small throughout particle motion in the accelerator. This can be achieved by defining the dynamical variables in relation to those of a *reference particle*. The momentum of the reference particle, the *reference momentum*, is defined as $P_0 = \beta_0 \gamma_0 m c$ and a particle with a higher momentum has a positive *energy deviation* δ, defined as

$$\delta = \frac{E}{c P_0} - \frac{1}{\beta_0}. \tag{1.8}$$

For the deviation from the reference particle position along the trajectory, i.e. along s, we introduce the variable z as

$$z = \frac{s}{\beta_0} - c\,t. \tag{1.9}$$

As accelerator beamlines usually contain dipole magnets, the reference trajectory is occasionally bent. It is therefore practical to introduce a coordinate system (x, y, s), with the transverse coordinates (x, y) defining a plane that is at all times perpendicular to s, while the reference trajectory is bent with a curvature $h = 1/\rho$, where ρ is the radius of curvature.

Applying these modifications to Eq. 1.7, the Hamiltonian is expressed as

$$H = \frac{\delta}{\beta_0} - (1 + h\,x)\sqrt{\left(\delta + \frac{1}{\beta_0} - \frac{q\Phi}{c P_0}\right)^2 - \left(p_x - a_x\right)^2 - \left(p_y - a_y\right)^2 - \frac{1}{\beta_0^2 \gamma_0^2}} - (1 + h\,x)\, a_s. \tag{1.10}$$

Here, x is the horizontal coordinate, a_x is the component of the vector potential in x direction, multiplied by q/P_0, and s and a_s are the coordinate and vector potential, respectively, in the direction of the reference trajectory. The transverse momenta p_x and p_y are functions of the time derivatives of x and y and are normalized to the reference momentum:

$$p_x = \frac{\gamma m \dot{x} + q A_x}{P_0} \text{ and } p_y = \frac{\gamma m \dot{y} + q A_y}{P_0}. \tag{1.11}$$

1.1.1 The symplectic transfer map

A *transfer map* relates the dynamical variables of a particle between different points in an accelerator beamline. This is written as

$$\vec{x}(s_1) = \vec{M}\left(\vec{x}(s_0)\right), \tag{1.12}$$

where a 6-dimensional *phase space vector* $\vec{x}(s) = (x, p_x, y, p_y, z, \delta)$ contains the dynamical variables of the particle and the transfer map $\vec{M}$ describes the particle transport from s_0 to s_1 along the accelerator beamline. The transfer map is built from the solutions of the equations of motion, that depend on the electromagnetic field configuration along the beamline. Usually, these fields stem from standardized accelerator components. A few examples of such transfer maps

in their linear approximation are given in the next section. The transfer map of a sequence of accelerator components is easily obtained by matrix multiplication of the transfer maps of the individual components. In a circular accelerator, the *one-turn map* is defined accordingly.

An important property of the equations of motion derived with the Hamiltonian formalism, is that their solutions generate *symplectic* transfer maps. Such transfer maps are associated with conserved quantities, for example, the density of particles in phase space (also known as *Liouville's theorem*). Focusing a particle beam horizontally with a quadrupole magnet will decrease its size (coordinate x), but at the same time increase its divergence (or momentum p_x), so that the horizontal phase space volume the beam occupies, remains unchanged. For each degree of freedom of particle motion exists therefore an emittance that is conserved under particle beam transport, see also Section 1.3.1[1].

As will be discussed in Chapters 3 and 4, there are effects that influence the particle density in phase space, and therefore generate emittance. To study such effects numerically, the transfer maps used in simulation must be free of any non-symplectic elements that might lead to unphysical growth or damping of particle motion. This is of increasing importance, the longer particles are followed (or *tracked*) through an accelerator. As an example, the particle tracking studies and their results presented in Paper **I**, where the path of particles is follow for many hundreds of turns in the storage ring, are highly dependent on the symplecticity of particle transfer applied by the numerical code Tracy-3 [Bengtsson]. One crucial and non-trivial ingredient of such codes is therefore the representation of transfer maps that, while originating from truncated Hamiltonians and therefore representing particle motion to a certain order in the dynamical variables, are still symplectic [Forest and Ruth, 1990][Berg et al., 1994].

1.2 Linear transfer maps

In a few cases, a linear transfer map that is relatively simple and symplectic, can be derived. Of special interest is the representation of the skew quadrupole and its numerical treatment, since the coupling from this accelerator element plays an important role in Paper **I**.

1.2.1 Drift space

The absence of electromagnetic fields in a region of space is referred to as a *drift space*. An example of drift space are long straight sec-

[1] The assumption here is that the motions in each of the degrees of freedom are independent. In fully-coupled motion only the overall 6-dimensional emittance is preserved.

tions in storage ring light sources which are field-free as long as no insertion devise is installed. Solving the Hamiltonian (Eq. 1.10) to first oder, with both vector potential and scalar potential zero, the resulting equations of motion can be expressed in terms of the linear transfer map for a drift space as

$$R_{\text{drift}} = \begin{pmatrix} 1 & L & 0 & 0 & 0 & 0 \\ 0 & 1 & 0 & 0 & 0 & 0 \\ 0 & 0 & 1 & L & 0 & 0 \\ 0 & 0 & 0 & 1 & 0 & 0 \\ 0 & 0 & 0 & 0 & 1 & \frac{L}{\beta_0^2\gamma_0^2} \\ 0 & 0 & 0 & 0 & 0 & 1 \end{pmatrix}, \tag{1.13}$$

where L is the length of the drift space. A particle with a certain position in phase space is described by the six-dimensional phase space vector before the drift

$$\vec{x}_0 = \begin{pmatrix} x \\ p_x \\ y \\ p_y \\ z \\ \delta \end{pmatrix}, \tag{1.14}$$

and will be translated to a new position in phase space $\vec{x}_1$ after propagating along the drift. This is expressed as

$$\vec{x}_1 = R_{\text{drift}}\vec{x}_0. \tag{1.15}$$

1.2.2 Quadrupole and skew quadrupole

Quadrupole magnets generate strong focusing by applying a transverse kick to particles that grows linearly with the particle coordinate (i.e. deviation from the reference trajectory). The magnetic field in a quadrupole, scaled by q/P_0, is given by

$$\boldsymbol{b} = (k_1 y, k_1 x, 0), \tag{1.16}$$

and is illustrated in Figure 3. The transfer map for a distance L a particle travels through in a quadrupole field becomes

$$R_{\text{quad}} = \begin{pmatrix} \cos(\omega L) & \frac{\sin(\omega L)}{\omega} & 0 & 0 & 0 & 0 \\ -\omega\sin(\omega L) & \cos(\omega L) & 0 & 0 & 0 & 0 \\ 0 & 0 & \cosh(\omega L) & \frac{\sinh(\omega L)}{\omega} & 0 & 0 \\ 0 & 0 & \omega\sinh(\omega L) & \cosh(\omega L) & 0 & 0 \\ 0 & 0 & 0 & 0 & 1 & \frac{L}{\beta_0^2\gamma_0^2} \\ 0 & 0 & 0 & 0 & 0 & 1 \end{pmatrix}. \tag{1.17}$$

Here $\omega = \sqrt{k_1}$ and k_1 is the *normalized quadrupole gradient*

$$k_1 = \frac{q}{P_0}\frac{\partial B_y}{\partial x} = \frac{q}{P_0}\frac{\partial B_x}{\partial y}, \tag{1.18}$$

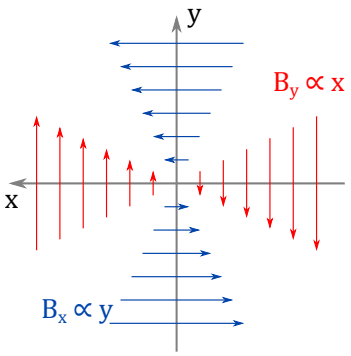

Figure 3. *Schematic of the transverse magnetic fields in an upright quadrupole magnet.*

i.e. normalized to the particle momentum. The transfer matrix, applied to an initial set of phase space coordinates, reads

$$\vec{x}_1 = R_{\text{quad}}\vec{x}_0. \tag{1.19}$$

A skew quadrupole magnet provides the normalized magnetic fields

$$\boldsymbol{b} = (-k_1^{(s)}x, k_1^{(s)}y, 0), \tag{1.20}$$

where $k_1^{(s)}$ is the normalized skew quadrupole gradient given by

$$k_1^{(s)} = \frac{q}{P_0}\frac{\partial B_y}{\partial y} = -\frac{q}{P_0}\frac{\partial B_x}{\partial x}. \tag{1.21}$$

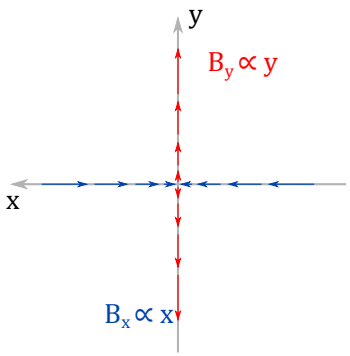

Figure 4. *Schematic of the transverse magnetic fields in a skew quadrupole magnet.*

This element has a generally different effect on particle motion than the *upright* quadrupole magnet introduced above: in a skew quadrupole field (see Figure 4), any horizontal deviation from the reference trajectory will result in a vertical deflection, and vice-versa. An accelerator with a skew quadrupole component will therefore show interdependent particle motion in the transverse planes. The skew quadrupole is therefore one example of an accelerator element that generates so-called *betatron coupling*, see Section 1.5.4. The representation of a skew quadrupole is obtained from the ordinary or upright quadrupole transfer map, rotated by 45°. Rotating in the (x, y)-plane by an angle θ around the reference trajectory is achieved by applying the rotation matrix

$$R_{\text{rot}}(\theta) = \begin{pmatrix} \cos\theta & 0 & \sin\theta & 0 & 0 & 0 \\ 0 & \cos\theta & 0 & \sin\theta & 0 & 0 \\ -\sin\theta & 0 & \cos\theta & 0 & 0 & 0 \\ 0 & -\sin\theta & 0 & \cos\theta & 0 & 0 \\ 0 & 0 & 0 & 0 & 1 & 0 \\ 0 & 0 & 0 & 0 & 0 & 1 \end{pmatrix}. \tag{1.22}$$

Then the transfer map of a pure skew quadrupole is

$$R_{\text{sq}} = R_{\text{rot}}\left(-\frac{\pi}{4}\right)R_{\text{quad}}R_{\text{rot}}\left(\frac{\pi}{4}\right). \tag{1.23}$$

It is equivalent to rotating the phase space of the beam, propagating the beam through an upright quadrupole and rotating the phase space back.

1.2.3 Radio frequency cavity

In a rf cavity resonator particle motion is influenced by oscillating electromagnetic fields. In accelerating rf cavities, electric fields along the particle trajectory influence the longitudinal phase space of the particles, affecting the longitudinal particle density (or *bunch shape*), and replenish the energy of particles that is lost, for example

to SR. The role of rf cavities in longitudinal particle motion is introduced in Chapter 2 and the details of the rf cavity-beam interaction in the MAX IV 3 GeV storage ring are presented in Paper **II**.

In a simplified case of a cylindrical rf cavity oscillating in the TM_{010} mode the electric field components can be written in polar coordinates as

$$E_r = 0, \tag{1.24}$$
$$E_\theta = 0, \tag{1.25}$$
$$E_s = E_0 J_0(kr)\,\sin(\omega t + \phi_0), \tag{1.26}$$

where E_0 is the field amplitude, J_0 is a zeroth-order Bessel function and $\omega = kc$. In a cylindrical cavity the relation between the cavity radius a and wave number k is given by

$$k = \frac{P_{01}}{a}, \tag{1.27}$$

where $P_{01} \approx 2.405$ is the first root of the Bessel function J_0. In order to satisfy Maxwell's equations, a magnetic field with the following components must also exist:

$$B_r = 0, \tag{1.28}$$
$$B_\theta = \frac{E_0}{c} J_1(kr)\,\cos(\omega t + \phi_0), \tag{1.29}$$
$$B_s = 0, \tag{1.30}$$

where J_1 is a first order Bessel function. For efficient acceleration, the time a particle takes to cross the cavity should not be longer than half the oscillation period of the fields, otherwise the particle would experience deceleration. This restricts the cavity length L depending on the particle velocity $\beta_0 c$ as follows:

$$\frac{L}{\beta_0 c} = \frac{\pi}{\omega} \tag{1.31}$$

From these field components a vector potential is found and a Hamiltonian is constructed. Solving the equations of motion for this case results in a linear transfer map, relating a phase space vector before cavity passage $\vec{x}_0$ to a vector after the passage $\vec{x}_1$, in the form

$$\vec{x}_1 = R_{\mathrm{rf}}\vec{x}_0 + \vec{m}_{\mathrm{rf}} \tag{1.32}$$

with

$$R_{\mathrm{rf}} = \begin{pmatrix} c_\perp & s_\perp & 0 & 0 & 0 & 0 \\ -\omega_\perp^2 s_\perp & c_\perp & 0 & 0 & 0 & 0 \\ 0 & 0 & c_\perp & s_\perp & 0 & 0 \\ 0 & 0 & -\omega_\perp^2 s_\perp & c_\perp & 0 & 0 \\ 0 & 0 & 0 & 0 & c_\parallel & \frac{1}{\beta_0^2\gamma_0^2} s_\parallel \\ 0 & 0 & 0 & 0 & -\beta_0^2\gamma_0^2\omega_\parallel^2 s_\parallel & c_\parallel \end{pmatrix} \tag{1.33}$$

and

$$\vec{m}_{\mathrm{rf}} = \begin{pmatrix} 0 \\ 0 \\ 0 \\ 0 \\ \left(1-\cos(\omega_{\parallel} L)\right)\frac{\tan\phi_0}{k} \\ \beta_0^2\gamma_0^2\omega_{\parallel}\sin(\omega_{\parallel} L)\frac{\tan\phi_0}{k} \end{pmatrix}, \tag{1.34}$$

where the transverse parameters are given by

$$c_{\perp} = \cos(\omega_{\perp} L), \tag{1.35}$$

$$s_{\perp} = \frac{\sin(\omega_{\perp} L)}{\omega_{\perp}}, \tag{1.36}$$

$$\omega_{\perp} = k\sqrt{\frac{\alpha\cos\phi_0}{2\pi}}, \tag{1.37}$$

while the longitudinal parameters are

$$c_{\parallel} = \cos(\omega_{\parallel} L), \tag{1.38}$$

$$s_{\parallel} = \frac{\sin(\omega_{\parallel} L)}{\omega_{\parallel}}, \tag{1.39}$$

$$\omega_{\parallel} = \frac{k}{\beta_0\gamma_0}\sqrt{\frac{\alpha\cos\phi_0}{\pi}}, \tag{1.40}$$

and finally

$$\alpha = \frac{qV_0}{P_0 c}. \tag{1.41}$$

Here P_0 is the reference momentum and V_0 is the *cavity voltage* amplitude, experienced by the particles, and is in our case calculated as

$$V_0 = E_0 T L, \tag{1.42}$$

with the *transit time factor* T, that takes the varying electric field during the passage of a particle through the rf cavity into account. It is defined as

$$T = \frac{2\pi\beta_0}{k^2 L^2}\sin\left(\frac{kL}{2\beta_0}\right). \tag{1.43}$$

The part of the transfer map R_{rf} in Eq. 1.33 shows, that not only a simple acceleration (or deceleration) in terms of a ΔE is provided by an rf cavity. Instead even the transverse planes are affected, as a consequence of the magnetic field (Eq. 1.29). In the longitudinal dimension $\vec{m}_{\mathrm{rf}}$, the part of the transfer map that is independent of particle coordinates in phase space, leads to a change in energy deviation $\Delta\delta$ that is given by

$$\Delta\delta \approx \frac{qV_0}{P_0 c}\frac{kL}{\pi}\sin\phi_0 \tag{1.44}$$

to compensate energy loss. The longitudinal components of R_{rf}, on the other hand, are an essential ingredient for bound longitudinal motion in a synchrotron, as discussed in Section 2.2.

1.3 Uncoupled particle dynamics

In this section particle motion is treated as independent in each of the three degrees of freedom. Although an ideal picture, many fundamental principles present in real accelerators can be approximated and understood in this simplified way. With a suitable parametrization, particle dynamics is described in terms of parameters that vary while particles pass along the beamline on one hand, and constants of motion on the other hand.

1.3.1 Courant-Snyder parameters

Assuming an accelerator beamline that is represented by a symplectic transfer map R, this transfer map satisfies the symplectic condition

$$R^T S R = S, \tag{1.45}$$

where S is the antisymmetric matrix defined as

$$S = \begin{pmatrix} 0 & 1 & 0 & 0 & 0 & 0 \\ -1 & 0 & 0 & 0 & 0 & 0 \\ 0 & 0 & 0 & 1 & 0 & 0 \\ 0 & 0 & -1 & 0 & 0 & 0 \\ 0 & 0 & 0 & 0 & 0 & 1 \\ 0 & 0 & 0 & 0 & -1 & 0 \end{pmatrix}. \tag{1.46}$$

In the absence of coupling, the motion in the horizontal plane is described by R_x, which is a 2×2 block diagonal sub-matrix of the transfer matrix R. R_x is also symplectic and it can be expressed as

$$R_x = I_2 \cos\mu_x + S_2 A_x \sin\mu_x, \tag{1.47}$$

with the matrices

$$I_2 = \begin{pmatrix} 1 & 0 \\ 0 & 1 \end{pmatrix} \text{ and } S_2 = \begin{pmatrix} 0 & 1 \\ -1 & 0 \end{pmatrix}, \tag{1.48}$$

the symmetric matrix A_x and the phase advance μ_x. When expressing A_x as

$$A_x = \begin{pmatrix} \gamma_x & \alpha_x \\ \alpha_x & \beta_x \end{pmatrix}, \tag{1.49}$$

we find the horizontal *Courant-Snyder parameters* α_x, β_x and γ_x [Courant and Snyder, 1958] or alternatively *Twiss parameters* [Twiss and Frank, 1949] that obey the relation

$$\beta_x \gamma_x - \alpha_x^2 = 1. \tag{1.50}$$

In a periodic accelerator structure such as a synchrotron the Courant-Snyder parameters have defined values that oscillate with the same periodicity as the magnetic lattice and that depend only

on the lattice. Especially the *beta functions*, the parameters β_x and β_y as a function of s, play an important roll in beam diagnostics, presented in Papers **III** and Paper **IV**, since they have direct influence on the beam size (Section 1.5.3). The importance of the beta functions to characterize an accelerator lattice is also emphasized by Section III A of Paper **I**, where they serve as a simple measure to quantify and minimize deviations of particle dynamic, caused by the application of the presented dispersion bump scheme.

1.3.2 Action-angle variables

While the Courant-Snyder parameters vary along the accelerator beam line, they define, together with the phase space coordinates, the *action variable* J_x (here given in the horizontal plane), that is invariant under particle motion, and is defined as

$$J_x = \frac{1}{2}\left(\gamma_x x^2 + 2\alpha_x x p_x + \beta_x p_x^2\right). \tag{1.51}$$

Equation 1.51 describes an ellipse in phase space with a shape determined by the Courant-Snyder parameters and an area equal to $2\pi J_x$, see Figure 5. While a particle propagates through an accelerator beamline, it will only occupy points in phase space (x, p_x) that lie on this ellipse. The position of the particle in phase space can therefore, together with J_x, be defined by the *angle variable* Φ_x which, in the horizontal plane, is

$$\tan\Phi_x = -\beta_x \frac{p_x}{x} - \alpha_x. \tag{1.52}$$

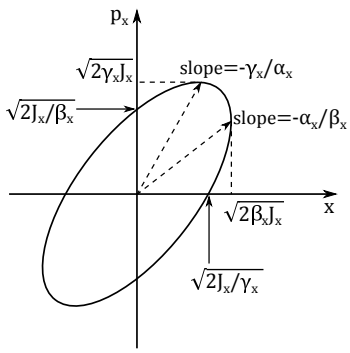

Figure 5. *Phase space ellipse in the horizontal degree of freedom with a shape defined by the Courant-Snyder parameters. The shape of the phase space ellipse varies along the accelerator beamline.*

The phase space coordinate x, expressed in action-angle variables, is

$$x = \sqrt{2\beta_x J_x}\cos\Phi_x \tag{1.53}$$

With the rate of change of the action variable along the beamline

$$\frac{d\Phi_x}{ds} = \frac{1}{\beta_x} \tag{1.54}$$

and the relation

$$\alpha_x = -\frac{1}{2}\frac{d\beta_x}{ds}, \tag{1.55}$$

the phase space coordinate p_x becomes

$$p_x = -\sqrt{\frac{2J_x}{\beta_x}}(\sin\Phi_x + \alpha_x\cos\Phi_x). \tag{1.56}$$

Equation 1.53 allows a simple interpretation of the beta function: a particle that is not on the reference trajectory will perform oscillations around the reference trajectory with an amplitude, that is determined by the constant action variable, and the value of the local

beta function $\beta_x(s)$. These oscillations in the transverse plane are called *betatron oscillations*.

With the rate of change of the action in Eq. 1.54 the *phase advance* in an accelerator lattice between two points, s and s_0, can be written as

$$\phi_x(s) = \int_{s_0}^{s} \frac{1}{\beta_x(\bar{s})} d\bar{s}. \tag{1.57}$$

In periodic circular accelerator lattices, the phase advance is equal in each cell and the phase advance for a full turn devided by 2π is called the *betatron tune*. In the MAX IV 3 GeV storage ring, the betatron tunes are $\nu_x = 42.2$ and $\nu_y = 16.28$. This means that each particle that is not on the reference trajectory performs 42.2 horizontal and 16.28 vertical betatron oscillations during each turn.

1.4 Particle distribution and projected emittance

The motion of any particle follows Eqs. 1.53 and 1.56 with its own initial phase space coordinates. These equations can therefore be used to express the distribution of many particles within an ensemble. Calculating the mean value of x^2 over all particles,

$$\langle x^2 \rangle = 2\beta_x \langle J_x \cos^2 \Phi_x \rangle = \beta_x \epsilon_x \tag{1.58}$$

we defined the horizontal emittance as

$$\langle J_x \rangle = \epsilon_x \tag{1.59}$$

under the assumption that all particles are uniformly distributed, and therefore

$$\langle x \rangle = 0. \tag{1.60}$$

Similarly, involving the distribution of the divergence p_x, we find

$$\langle x p_x \rangle = -\alpha_x \epsilon_x \text{ and } \langle p_x^2 \rangle = \gamma_x \epsilon_x \tag{1.61}$$

and express the horizontal emittance an ensemble of particles occupies in the horizontal phase space as

$$\epsilon_x = \sqrt{\langle x^2 \rangle \langle p_x^2 \rangle - \langle x p_x \rangle^2}. \tag{1.62}$$

Equation 1.62 is also referred to as the horizontal *projected emittance* [Franchi et al., 2011] to emphasize, that this definition of emittance is based on the laboratory frame of the accelerator. Its derivation as an emittance in terms of a conserved quantity depends on the absence of off-diagonal elements in the transfer map in Eq. 1.45. The emittance, projected to the laboratory frame, is therefore only conserved in the absence of betatron coupling. In a fully-coupled accelerator lattice there are still three conserved emittances, that are defined, however, in the eigenframe of the particle motion

(Section 1.5.4), which in general, does not coincide with the laboratory frame. In Paper **I**, where betatron coupling is deliberately introduced, distinguishing between projected emittance and eigenemittance becomes mandatory, see Figure 9 of Paper **I**. In the context of this paper, the projected emittance is relevant to describe the particle distribution in the IDs, devices that are aligned with respect to the laboratory frame.

1.5 Coupled motion

In strictly uncoupled particle motion, all three degrees of freedom of particle motion are independent of each other. Accelerator elements fulfilling this requirement are for example the drift space and the upright quadrupole, introduced in Section 1.2, since their transfer maps are indeed block diagonal. Different off-diagonal elements, appearing in the transfer matrix, for example in the transfer map of a skew quadrupole, are associated with different coupling effects of which some examples are given in this section.

1.5.1 Dispersion

A common type of coupling in a synchrotron is *dispersion*. It describes the dependence of the transverse trajectory of a particle on its energy deviation. Dispersion may be present in both transverse planes and is in general a function of s. The source of dispersion in a synchrotron are bending magnets. In a dipole the trajectory is bent with a curvature h that is given by

$$h = \frac{q}{P_0} B_0 = \frac{B_0}{B\rho}, \tag{1.63}$$

with the electric charge of the particle q, the reference momentum P_0 and the dipole field B_0. The term $B\rho$ is referred to as the *beam rigidity* and is in case of the MAX IV 3 GeV storage ring approximately 10 Tm. The transfer map of a dipole magnet without field gradient and with no focusing effect on the beam is given by

$$R = \begin{pmatrix} \cos(hL) & \frac{\sin(hL)}{h} & 0 & 0 & 0 & \frac{1-\cos(hL)}{h\beta_0} & \\ -h\sin(hL) & \cos(hL) & 0 & 0 & 0 & \frac{\sin(hL)}{\beta_0} & \\ 0 & 0 & 1 & L & 0 & 0 & \\ 0 & 0 & 0 & 1 & 0 & 0 & 0 \\ -\frac{\sin(hL)}{\beta_0} & -\frac{1-\cos(hL)}{h\beta_0} & 0 & 0 & 1 & \frac{L}{\beta_0^2\gamma_0^2} - \frac{hL-\sin(hL)}{h\beta_0^2} & \\ 0 & 0 & 0 & 0 & 0 & 1 & \end{pmatrix} \tag{1.64}$$

for a dipole magnet of length L, curvature h and bending radius $\rho = 1/h$. Note that this transfer map is valid for a dipole magnet that bends the beam in the horizontal plane. It is most common in storage rings to use horizontal bending magnets exclusively, although

vertical bends may occur for example in transfer lines between pre-accelerators and the storage ring. A purely horizontal bending magnet couples only the horizontal and longitudinal plane while the vertical plane is equivalent to a drift space (cf. 1.2.1). In the horizontal plane two additional terms, R_{16} and R_{26}, appear that make the horizontal coordinates x and p_x dependent on momentum deviation. Expressed as a power series:

$$x(\delta_p) = x|_{\delta_p=0} + \eta_x \delta_p + \eta_x^{(2)} \delta_p^2 + \ldots, \tag{1.65}$$

$$p_x(\delta_p) = p_x\big|_{\delta_p=0} + \eta_{px} \delta_p + \eta_{px}^{(2)} \delta_p^2 + \ldots, \tag{1.66}$$

where the momentum deviation of a particle with momentum P is defined as

$$\delta_p = \frac{P}{P_0} - 1. \tag{1.67}$$

Then η_x is the first-order or linear horizontal dispersion, $\eta_x^{(2)}$ is the second-order dispersion and so on. Equation 1.65 provides the theoretical basis for dispersion measurements with a diagnostic beamline, presented in Paper **III** and discussed in Section 5.3.3. The dispersion in a storage ring has the same periodicity as the magnetic lattice, as is shown in Figure 1 of Paper **I** for one achromat of the MAX IV 3 GeV ring.

1.5.2 Vertical dispersion from skew quadrupoles

Although vertical bends may be absent in a storage ring, the vertical dispersion is not necessarily zero. This section gives a brief introduction of the principle of dispersion coupling from (mainly) the horizontal into the vertical plane by skew quadrupoles. Being an undesired consequence of lattice imperfections (Section 1.7.2) or intentionally designed as for the scheme presented in Paper **I**, the mechanism can be understood as follows.

Assume a particle that is vertically deflected at a location s_0 in a storage ring. Consequently, this particle will perform betatron oscillations on a closed orbit which includes the deflection Δp_y at s_0. The particle's path is also referred to as a closed orbit in presence of a single steering error, and is described by the expression

$$y(s) = \frac{\Delta p_y \sqrt{\beta_y(s)\beta_y(s_0)}}{2\sin(\pi \nu_y)} \cos\big(\phi_{y,0}(s) - \pi \nu_y\big), \tag{1.68}$$

with the vertical betatron tune ν_y and the vertical phase advance $\phi_{y,0}(s)$ between s and s_0. Assuming that the vertical deflection is the result of a horizontal offset x at location s_0 in a skew quadrupole of normalized gradient k and effective length l, it is given by

$$\Delta p_y(s_0) = x(s_0)\, k\, l. \tag{1.69}$$

The relation between transverse coordinate and (linear) dispersion in the horizontal and vertical plane (Eq. 1.65) is

$$x(s) = \eta_x(s)\,\delta_p \;\text{ and }\; y(s) = \eta_y(s)\,\delta_p, \tag{1.70}$$

for a relative momentum deviation δ_p, respectively. Combining the above expressions, the vertical dispersion function, created by a single skew quadrupole that couples horizontal dispersion into the vertical plane, can be expressed as

$$\eta_y(s) = \frac{\eta_x(s_0)\,kl}{2\sin(\pi\nu_y)}\sqrt{\beta_y(s)\beta_y(s_0)}\,\cos\big(\phi_{y,0}(s) - \pi\nu_y\big). \tag{1.71}$$

Thus, Eq. 1.71 describes in a closed expression, how horizontal dispersion is coupled into the vertical plane by a single skew quadrupole.

Let us then introduce a second skew quadrupole of equal normalized gradient and equal length at a location s_1, where $\beta_y(s_0) = \beta_y(s_1)$ and $\eta_x(s_0) = \eta_x(s_1)$ [2]. In linear approximation the vertical dispersion function is expressed as the sum of two contributions, each given by Eq. 1.71:

$$\eta_y(s) = \frac{\eta_x(s_0)\,kl}{2\sin(\pi\nu_y)}\sqrt{\beta_y(s)\beta_y(s_0)}\,\big[\cos\big(\phi_{y,0}(s) - \pi\nu_y\big) + \cos\big(\phi_{y,1}(s) - \pi\nu_y\big)\big], \tag{1.72}$$

where $\phi_{y,1}(s)$ is the phase advance between s and s_1. The term in square brackets is a sum of two cosine functions that can be rewritten as

$$2\cos\left(\frac{\phi_{y,0}(s) + \phi_{y,1}(s)}{2} - \pi\nu_y\right)\cos\left(\frac{\phi_{y,0}(s) - \phi_{y,1}(s)}{2}\right). \tag{1.73}$$

Assuming further that the vertical phase advance between the two skew quadrupoles is equal to π, then, according to Eq. 1.57, $|\phi_{y,1}(s) - \phi_{y,0}(s)| = \pi$ for $s < s_0$ or $s_1 < s$. In that case, the second term in Eq. 1.73 vanishes, and therefore also the vertical dispersion described by Eq. 1.72. When evaluating the phase advance in between the skew quadrupoles, that means for $s_0 < s < s_1$, however, the phase advances are related by $\phi_{y,0}(s) + \phi_{y,1}(s) = \pi$ and Eq. 1.73 becomes

$$2\sin\big(\pi\nu_y\big)\,\sin\big(\phi_{y,0}(s)\big). \tag{1.74}$$

Thus, the described configuration of two skew quadrupoles generates an ideal closed vertical dispersion bump with finite vertical dispersion between the skew quadrupoles and zero vertical dispersion elsewhere in the ring. Although not in an ideal manner, since with a phase advance of $0.932\,\pi$ between the two skew quadrupoles (in each of the 20 cells around the storage ring), Case 1, presented in

[2] Due to the symmetry in most storage ring lattices such a location usually exists.

Paper **I**, generates dispersion bumps that are still sufficiently closed in the long straights. An example where the phase advance condition is strictly fulfilled, and a non-zero vertical dispersion is created by two equal skew quadrupoles across one straight section of the MAX IV 3 GeV storage ring, is shown in Figure 6.

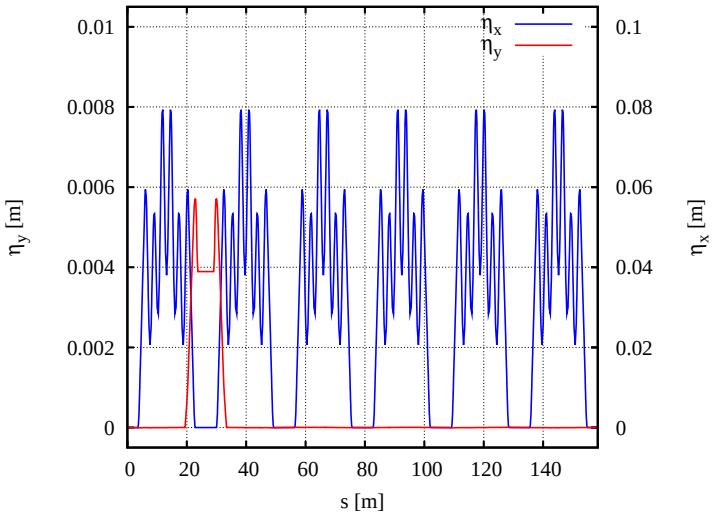

Figure 6. *Example of a closed vertical dispersion bump, opened and closed by two skew quadrupoles at lattice symmetry points, separated by a phase advance of π. Note the different scaling for the horizontal dispersion on the right axis of the plot.*

1.5.3 Beam size and beam divergence

Combining the *betatronic contribution* to the beam size from Eq. 1.58 with the (linear) *dispersive contribution* from Eq. 1.65, one obtains, under the assumption a of Gaussian particle distribution in phase space, the horizontal rms beam size as

$$\sigma_x = \sqrt{\beta_x \epsilon_x + \sigma_\delta^2 \eta_x^2}\,. \tag{1.75}$$

Similarly, for the vertical beam size we find

$$\sigma_y = \sqrt{\beta_y \epsilon_y + \sigma_\delta^2 \eta_y^2}\,. \tag{1.76}$$

With Eqs. 1.75 and 1.76 it is possible to deduce the emittances from the measured beam sizes, if the beta functions, the dispersions and the energy spread are known, see Chapter 5. The beam divergences are given by

$$\sigma_{p_x} = \sqrt{\gamma_x \epsilon_x + \sigma_\delta^2 \eta_{px}^2} \tag{1.77}$$

and

$$\sigma_{p_y} = \sqrt{\gamma_y \epsilon_y + \sigma_\delta^2 \eta_{py}^2}. \tag{1.78}$$

1.5.4 Fully coupled motion

For the most general case, allowing any coupling between all three degrees of freedom, a concept of *fully coupled motion* [Wolski, 2006][Wolski, 2014] is briefly introduced here. In the context of Paper **I** a general treatment of coupling is required considering betatron coupling caused by skew quadrupoles and is accounted for in the applied numerical simulation code Tracy-3. The aim of such a general approach is to express particle motion with reference to a new set of generalized Courant-Snyder parameters in an alternative coordinate system.

The definition of the second order moments of the particle distribution in one degree of freedom (the horizontal plane) is given by Eqs. 1.58 and 1.61. A general approach to k degrees of freedom is then

$$\Sigma_{ij} = \sum_k \beta_{ij}^k \, \varepsilon_k, \tag{1.79}$$

where in our case $k =$ I, II and III are three degrees of freedom, and $\Sigma_{ij} = \langle x_i x_j \rangle$ are the second order moments describing the beam distribution. The action in one dimension, in this case in the horizontal dimension as in Eq. 1.51, can be expressed as

$$2J_x = (x \; p_x) \, S^T \begin{pmatrix} \beta_x & -\alpha_x \\ -\alpha_x & \gamma_x \end{pmatrix} S \begin{pmatrix} x \\ p_x \end{pmatrix}, \tag{1.80}$$

where S is the antisymmetric matrix defined in Eq. 1.46. This would then, generalized to k dimensions, be given by

$$2J_k = \vec{x}^T S^T B^k S \, \vec{x} \tag{1.81}$$

with the 6-dimensional phase space vector $\vec{x}$ as defined in Eq. 1.14. The matrix B^k, containing the Courant-Snyder parameters, transforms like

$$B^k(s_1) = R(s_1, s_0) B^k(s_0) R(s_1, s_0)^T, \tag{1.82}$$

where $R = R(S_1, S_0)$ is a transfer map. For the symplectic matrix R with distinct eigenvalues, a *normalizing matrix* N can be found so that

$$N R N^{-1} = \bar{R}(\mu_k), \tag{1.83}$$

where $\bar{R}(\mu_k)$ is a rotation matrix with three angles $\mu_{\mathrm{I}}, \mu_{\mathrm{II}}$ and μ_{III} and is defined as

$$\bar{R}(\mu_k) = \begin{pmatrix} \cos\mu_{\mathrm{I}} & \sin\mu_{\mathrm{I}} & 0 & 0 & 0 & 0 \\ -\sin\mu_{\mathrm{I}} & \cos\mu_{\mathrm{I}} & 0 & 0 & 0 & 0 \\ 0 & 0 & \cos\mu_{\mathrm{II}} & \sin\mu_{\mathrm{II}} & 0 & 0 \\ 0 & 0 & -\sin\mu_{\mathrm{II}} & \cos\mu_{\mathrm{II}} & 0 & 0 \\ 0 & 0 & 0 & 0 & \sin\mu_{\mathrm{III}} & \cos\mu_{\mathrm{III}} \\ 0 & 0 & 0 & 0 & -\sin\mu_{\mathrm{III}} & \cos\mu_{\mathrm{III}} \end{pmatrix}. \tag{1.84}$$

The normalizing matrix N is itself symplectic and transforms a phase space vector in the laboratory frame $\vec{x}$ into the eigenframe, generating a new set of dynamical variables and a new phase space vector $\vec{\mathscr{X}}$, defined by

$$\vec{\mathscr{X}} = \begin{pmatrix} X_{\mathrm{I}} \\ P_{\mathrm{I}} \\ X_{\mathrm{II}} \\ P_{\mathrm{II}} \\ X_{\mathrm{III}} \\ P_{\mathrm{III}} \end{pmatrix} = N\vec{x}. \tag{1.85}$$

Expressed in normalized phase space coordinates, the action variables J_k and angle variables Φ_k are

$$J_k = \frac{1}{2}\left(X_k^2 + P_k^2\right) \text{ and } \tan\Phi_k = -\frac{P_k}{X_k}, \tag{1.86}$$

with

$$\vec{\mathscr{X}} = \begin{pmatrix} \sqrt{2J_{\mathrm{I}}}\cos\Phi_{\mathrm{I}} \\ -\sqrt{2J_{\mathrm{I}}}\sin\Phi_{\mathrm{I}} \\ \sqrt{2J_{\mathrm{II}}}\cos\Phi_{\mathrm{II}} \\ -\sqrt{2J_{\mathrm{II}}}\sin\Phi_{\mathrm{II}} \\ \sqrt{2J_{\mathrm{III}}}\cos\Phi_{\mathrm{III}} \\ -\sqrt{2J_{\mathrm{III}}}\sin\Phi_{\mathrm{III}} \end{pmatrix}. \tag{1.87}$$

The motion in these *normal modes* is independent in each plane k, since a phase space vector $\vec{\mathscr{X}}$ transforms with the block diagonal transfer map $\bar{R}(\mu_k)$ as a particle moves along the accelerator beamline as follows:

$$\vec{\mathscr{X}}(s_1) = \bar{R}(\mu_k)\vec{\mathscr{X}}(s_0). \tag{1.88}$$

Each degree of freedom is then associated with a constant *eigenemittance* or *normal mode emittance*, in our case $\mathscr{E}_{\mathrm{I}}, \mathscr{E}_{\mathrm{II}}$ and $\mathscr{E}_{\mathrm{III}}$, defined as (cf. Eq. 1.59)

$$\mathscr{E}_k = \langle J_k \rangle. \tag{1.89}$$

The eigenframe of the beam is relevant for mechanisms in the bunch itself, such as damping and excitation and the equilibrium emittance, discussed in Chapter 3. Only in the case of vanishing coupling will the projected emittance in the laboratory frame be identical to the eigenemittance, since in that case the off-diagonal elements in the laboratory frame transfer map become zero and the

laboratory frame action-angle variables and dynamical variables are eigenmodes as they are. This can occur locally in a storage ring, as shown in Figure 9 of Paper **I**, where coupling in the vertical plane is minimized in the long straights of the MAX IV 3 GeV ring. As a consequence, the projected vertical emittance approaches the value of the constant normal mode II emittance.

The amount of coupling in storage ring is in many cases low enough to allow for an approximate identification of the normal modes with the dimensions x, y and z in the laboratory frame. The second statistical moment of the laboratory frame vertical coordinate y, for example, is according to Eq. 1.79 given by

$$\langle y^2 \rangle = \beta_{33}^{\mathrm{I}} \mathscr{E}_{\mathrm{I}} + \beta_{33}^{\mathrm{II}} \mathscr{E}_{\mathrm{II}} + \beta_{33}^{\mathrm{III}}. \tag{1.90}$$

This is an exact expression for any kind of coupling among the three planes. In case of weak coupling, however, the eigenmode II can be associated with the laboratory y-plane. Then β_{33}^{I} describes the (betatron) coupling of the eigenmode I, associated with horizontal motion, into the y-plane while $\beta_{33}^{\mathrm{III}}$ represents the coupling to the longitudinal plane. If betatron coupling and coupling between the vertical and longitudinal plane are small ($\beta_{33}^{\mathrm{I}} \approx 0$ and $\beta_{33}^{\mathrm{III}} \approx 0$) we can conclude

$$\beta_{33}^{\mathrm{II}} \approx \beta_y. \tag{1.91}$$

1.6 Nonlinear dynamics

In the previous sections particle dynamics has been treated under the assumption of linear approximations to the equations of motion. There are, however, nonlinear effects present which especially in MBA lattices are not negligible. Influencing and correcting nonlinear particle dynamics requires magnetic multipoles of higher, orders such as sextupole magnets and octupole magnets.

1.6.1 Chromaticity and sextupole magnets

The linear transfer map for a quadrupole, derived in Section 1.2.2, assumes a focusing effect that is independent of the energy deviation δ of the particle. There is, however, a variation of focusing strength with particle energy called *chromaticity* that is defined in the horizontal plane as

$$\xi_x = P_0 \frac{d\nu_x}{dP_0} = -\frac{1}{4\pi} \oint \beta_x (h k_0 + k_1)\, ds \tag{1.92}$$

where ν_x is the horizontal tune and k_1 is the normalized quadrupole gradient as defined in Eq. 1.18. In the horizontal plane there is a contribution from dipole magnets depending on h, the curvature of the

reference trajectory, and on the normalized dipole field strength k_0, defined as

$$k_0 = \frac{q}{P_0} B_y. \tag{1.93}$$

In the vertical plane the chromaticity yields

$$\xi_y = P_0 \frac{d\nu_y}{dP_0} = \frac{1}{4\pi} \oint \beta_y k_1 ds, \tag{1.94}$$

with ν_y being the vertical tune.

Since a particle with positive energy deviation will experience less deflection by the magnetic fields of quadrupole magnets, it will be less focused than the reference particle, see Figure 7. The betatron tune is therefore reduced for particles with positive energy deviation. Thus, a storage ring with linear magnetic elements only, will have negative *natural chromaticities* in the horizontal and the vertical plane that scale linearly with the quadrupole gradients. High negative natural chromaticities are therefore typical in MBA lattices, where strong quadrupole gradients are employed. Large variations in betatron tunes with energy must be avoided, since particles with tunes close to integer and half-integer values are sensitive to steering errors from lattice imperfections. Controlling the chromaticity is therefore an essential ingredient also for the MAX IV 3 GeV storage ring [Leemann et al., 2009].

The sextupole magnet provides a field configuration that allows for chromaticity correction without major effects on the linear optics. Its field components, scaled to the particle momentum, are

$$b_x = k_2 x y, \tag{1.95}$$

$$b_y = \frac{1}{2} k_2 (x^2 - y^2), \tag{1.96}$$

$$b_z = 0, \tag{1.97}$$

and the *normalized sextupole strength* k_2 is

$$k_2 = \frac{q}{P_0} \frac{\partial^2 B_y}{\partial x^2}. \tag{1.98}$$

Including the effect of sextupole magnets into Eqs. 1.92 and 1.94, the chromaticities can be expressed by

$$\xi_x = -\frac{1}{4\pi} \oint \beta_x (h k_0 + k_1 - \eta_x k_2)\, ds \tag{1.99}$$

and

$$\xi_y = \frac{1}{4\pi} \oint \beta_y (k_1 - \eta_x k_2)\, ds, \tag{1.100}$$

where η_x is the horizontal dispersion. It is therefore possible to influence the chromaticities with sextupoles placed in dispersive sections

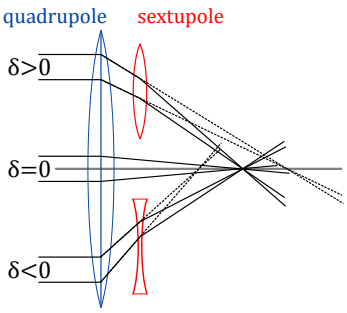

Figure 7. *Chromatic effect of a quadrupole magnet (dashed lines) and its correction by a sextupole magnet (solid lines). Drawing inspired by [Wiedemann, 2007].*

of the storage ring. The principle can be understood as follows: in areas of positive horizontal dispersion particles with positive energy deviation have a non-zero horizontal coordinate. A sextupole with positive strength $k_2 > 0$ will then supply focusing and therefore add a positive contribution to the horizontal chromaticity (see Figure 7).

A sextuple magnet will always affect the chromaticity in both planes, however, the effect depends on the beta functions. It is therefore possible to correct the chromaticities in both planes to desired values (usually slightly above zero) by a pair of sextupoles (or sextupole families). This concept is applied to the MAX IV 3 GeV storage ring to correct the linear chromaticities to $\xi_x = 1$ and $\xi_y = 1$.

The scheme presented in Paper **I** alters the linear optics as well as the nonlinear optics of the storage ring, and a correction by sextupole magnets is required to return to design parameters. This is discussed in Section III E of Paper **I** showing Figure 15 with the variation of the betatron tunes as a function of momentum deviation. The considerable deviation from linear behavior implies that higher orders of chromaticity are present and non-negligible.

Negative side effects of sextupole magnets are their influence on particle motion in phase space. While in linear dynamics particles follow an ellipse in phase space, defined by the Courant-Snyder parameters (Section 1.3.1), traces in phase space become deformed when nonlinear elements are employed. As a consequence not all coordinates in phase space can be associated with stable betatron motion. Instead, stable motion is only possible within a limited area in phase space, which leads to a finite *dynamic aperture* in the transverse coordinates. Study and correction of nonlinear dynamics is therefore essential to fulfill critical design parameters. The injection efficiency of a storage ring, for example, depends on the dynamic aperture at the injection point and it is therefore discussed in Section III E of Paper **I**.

1.7 Lattice imperfections

The theoretical treatment of particle dynamics has so far assumed an ideal storage ring, consisting of perfect accelerator components and magnets. A real storage ring, however, is built from magnets that deviate from design in terms of field strength and higher-order field contributions. Furthermore, the installation of a long sequence of accelerator components will inevitably introduce alignment errors of magnets.

1.7.1 Closed orbit distortions

In an ideal storage ring lattice a particle with initial phase space coordinates (0,0,0,0,0,0) will circulate on the reference trajectory, leading through the (field-free) center of quadrupole and sextupole magnets.

A steering error, for example from a field strength error in a dipole magnet or a misplaced quadrupole magnet, results in a closed orbit that deviates from the reference trajectory (cf. Eq. 1.68). The closed orbit fulfills thereby the requirement of having a periodicity equal to one turn in the storage ring. The purpose of *orbit correction*, as applied in the work presented in Paper **I**, is to correct the closed orbit towards the reference trajectory by employing dedicated horizontal and vertical corrector magnets.

1.7.2 Coupling

The alignment error of a quadrupole magnet will in general also include a rotation of the magnet around the particle trajectory. As discussed in Section 1.2.2, such a rotation is a representation of a skew quadrupole component that couples the transverse planes and generates vertical dispersion through a mechanism discussed in Section 1.5.2. Coupling is the dominant contribution to the vertical emittance in a flat machine (i.e. without vertical bends), and excites vertical emittance both by vertical dispersion and betatron coupling. In contrast to the scheme of well-controlled successive closed vertical dispersion bumps presented in Paper **I**, however, skew quadrupole components from lattice imperfections cause irregular vertical dispersion and betatron coupling, that are not confined to the arcs and therefore affect ID source properties. An example is given in Figures 6 and 7 of Paper **I** where the vertical dispersion, originating from lattice imperfections, is compared to that resulting from closed dispersion bumps. It is therefore beneficial in terms of ID source properties to minimize any undesired coupling and regain Touschek lifetime up to a desired level by applying a systematic scheme for vertical emittance adjustment.

1.7.3 Nonlinear lattice errors

Field strength errors in quadrupoles or undesired quadrupole components affect beam focusing locally, leading to a variation in the amplitude of betatron oscillations, the so-called *beta beating*. The beam optics in the MAX IV 3 GeV storage ring is based on a careful balance of sextupole and octupole magnet strengths. This balance can be disturbed by beta beating and/or higher-order field errors, resulting in, for example, a reduced dynamic aperture. In Section III F of Paper **I** particle dynamics is therefore also studied under the influence of random lattice errors that resemble expected deviations of a real accelerator lattice from its ideal counterpart.

CHAPTER 2

LONGITUDINAL BEAM DYNAMICS

Longitudinal beam dynamics describes particle motion in the (z,δ)-plane, z being collinear with the particle trajectory. While in both transverse planes it is mostly the strong focusing from quadrupole magnets that determines the linear dynamics by betatron oscillations, the mechanism of longitudinal motion is different and is therefore treated in a separate chapter.

2.1 Momentum compaction and phase slip

Due to dispersion the path length in a magnetic dipole field depends on the particle momentum. In presence of dispersion in the horizontal plane, the path length dC along the reference trajectory ds is given by

$$dC = (\rho + x)\, d\theta = (\rho + x)\frac{ds}{\rho}, \tag{2.1}$$

where ρ is the bending radius of the reference trajectory. Along a beamline of length C_0, the relative change in path length with respect to momentum deviation for particles with zero momentum deviation is called the (first order) *momentum compaction factor*, and is defined as

$$\alpha_c = \frac{1}{C_0}\left.\frac{dC}{d\delta_p}\right|_{\delta_p=0} = \frac{1}{C_0}\int_0^{C_0}\frac{\eta_x}{\rho}\,ds, \tag{2.2}$$

where η_x is the horizontal dispersion. In a storage ring the *first synchrotron radiation integral* is defined as

$$I_1 = \oint \frac{\eta_x}{\rho}\,ds \tag{2.3}$$

and is integrated around the circumference of the storage ring. Contributions to the integral originate from sections where the beam

is bent ($\rho < \infty$) while the dispersion is non-zero. The momentum compaction factor in a storage ring then becomes

$$\alpha_c = \frac{I_1}{C_0}. \tag{2.4}$$

Higher-order momentum compaction factors are defined by

$$\frac{C}{C_0} = 1 + \alpha_c \delta_p + \alpha_c^{(2)} \delta_p^2 + \alpha_c^{(3)} \delta_p^3 + \dots . \tag{2.5}$$

As a general consequence of different path lengths at different momentum deviations, the time for one revolution in the storage ring will also depend on the momentum deviation. This can be expressed in terms of the *phase slip factor*, defined as

$$\eta_p = \frac{1}{T_0} \frac{dT}{d\delta_p}\bigg|_{\delta_p=0}, \tag{2.6}$$

where T is the time of flight for a particle along the beamline and T_0 is the time of flight of the reference particle. For a particle with zero momentum deviation the phase slip factor becomes

$$\eta_p = \alpha_c - \frac{1}{\gamma_0^2}. \tag{2.7}$$

The momentum compaction factor in a storage ring is typically positive as a consequence of longer paths through the bending magnets at increased momentum. In the MAX IV 3 GeV storage ring we find $\alpha_c \approx 3.07 \cdot 10^{-4}$ [MAX IV Facility, 2010] and $\gamma \approx 6000$. This results in a positive phase slip factor (typical for electron synchrotrons) which means that a particle with a positive energy deviation has a longer revolution period than the reference revolution period T_0.

2.2 Synchrotron motion

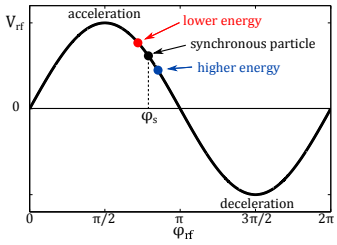

Figure 8. *Phase relation for particle acceleration with a sinusoidal rf voltage (single rf system) in an electron synchrotron.*

Longitudinal motion of particles in a synchrotron, the *synchrotron motion*, is an interplay of phase slip and the interaction of particles with the fields in rf cavities (Section 1.2.3). The motion in a storage ring with a single rf system is discussed in this section, while the effect of harmonic cavities on particle motion is briefly introduced in Section 2.3.

A particle with positive momentum deviation ($\delta_p > 0$) in a storage ring with positive phase slip factor ($\eta_p > 0$) will, after one turn in the synchrotron, arrive with a delay with respect to the reference particle. The rf cavity phase for acceleration is therefore chosen to provide a higher cavity voltage for particles arriving later than the reference particle and a lower voltage for particles arriving earlier (accelerating on the 'falling slope', see Figure 8). If the cavity voltage is supplied with such a phase dependence, an oscillation of the off-energy

particles around the reference particle is possible. This concept is also called *phase focusing* and ensures that bound motion exists for particles with non-zero momentum deviation δ.

The equation of motion in the longitudinal plane is

$$\frac{d^2z}{ds^2} = -\frac{q\,V_{\mathrm{rf}}}{c\,P_0\,C_0}\,\eta_p \sin\left(\phi_{\mathrm{rf}} - \frac{\omega_{\mathrm{rf}}\,z}{c}\right) + \eta_p\,\frac{U_0}{c\,P_0\,C_0}, \tag{2.8}$$

and the first term on the right hand side describes the effect of a change in energy deviation from a rf cavity (Eq. 1.44), providing an accelerating voltage with amplitude V_{rf}, frequency ω_{rf} and phase ϕ_{rf}. The second term accounts for the effect of an energy loss U_0 of a particle (mainly due to synchrotron radiation, see Section 3.1). If the rf phase is set so that the cavity provides an energy change that compensates the energy loss in one turn, then $\phi_{\mathrm{rf}} = \phi_s$ and we call ϕ_s the *synchronous phase*, which is given by

$$\sin\phi_s = \frac{U_0}{q\,V_{\mathrm{rf}}}. \tag{2.9}$$

The reference particle has $\delta = 0$ by definition and does not oscillate, but is accelerated at the synchronous phase. Off-energy particles, however, oscillate about the synchronous phase, which is described by

$$\frac{d^2z}{ds^2} = -k_z^2 z \;\text{ with }\; k_z^2 = -\frac{q\,V_{\mathrm{rf}}}{c\,P_0}\,\frac{\omega_{\mathrm{rf}}}{c\,C_0}\,\eta_p\cos\phi_s \tag{2.10}$$

and stable motion is found for particles fulfilling

$$q\,V_{\mathrm{rf}}\,\eta_p\cos\phi_s < 0\,. \tag{2.11}$$

For positive η_p, and assuming that the accelerating voltage is defined in a way that $q\,V_{\mathrm{rf}} > 0$, we find the range of stable motion for the reference (synchronous) particle in a single-rf system as

$$\frac{\pi}{2} < \phi_s < \pi\,. \tag{2.12}$$

The number of synchrotron oscillations per turn in the storage ring is called the *synchrotron tune*, and is given by the expression

$$\nu_z = \frac{k_z\,C_0}{2\pi} = \frac{1}{2\pi}\sqrt{-\frac{q\,V_{\mathrm{rf}}}{c\,P_0}\,\frac{\omega_{\mathrm{rf}}C_0}{c}\,\eta_p\cos\phi_s}\,. \tag{2.13}$$

Compared to the betatron oscillation, and even compared to the revolution period, the synchrotron motion is slow with a typical tune of the order $1\cdot10^{-3}$. Figure 6 of Paper **II**, as an example, shows the range of synchrotron tunes in the MAX IV 3 GeV ring.

The amplitude of synchrotron oscillations particles can perform without being lost is limited, since in practice the amplitude of the accelerating voltage V_{rf} is finite. The maximum value of momentum

deviation a particle can have without being lost is called the *rf acceptance* of the storage ring and is given by

$$\delta_{\mathrm{rf}} = \frac{2\nu_z}{h\,|\eta_p|}\sqrt{1+\left(\phi_s-\frac{\pi}{2}\right)\tan\phi_s}\,, \tag{2.14}$$

where h is the *harmonic number*, defined as

$$h = \frac{\omega_{\mathrm{rf}}}{\omega_0}, \tag{2.15}$$

and ω_0 is the revolution frequency. The harmonic number is equal to the number of *rf buckets* in the storage ring in which bunches of particles can be accelerated. For the MAX IV 3 GeV ring with $f_{\mathrm{rf}} = \omega_{\mathrm{rf}}/2\pi \approx 100$ MHz and $C_0 \approx 528$ m follows, that $h = 176$ rf buckets are available.

Since in a single rf system the rf voltage provides a restoring force on particles that is approximately linear around the synchronous phase, the Gaussian energy distribution of width σ_δ of a bunch of particles leads to a longitudinal charge distribution that is also Gaussian. The standard deviation of this longitudinal distribution is the rms bunch length and is given by

$$\sigma_z = \frac{\alpha_c\, c}{2\pi f_s}\sigma_\delta, \tag{2.16}$$

where α_c is the momentum compaction and $f_s = \nu_z/T_0$ is the synchrotron frequency.

2.3 Harmonic rf cavities

To generate a variability in longitudinal bunch shape, and mainly to provide bunch lengthening, a *harmonic rf system* is integrated into both MAX IV storage rings, which is operated at the third harmonic, i.e. at a frequency $f_{\mathrm{harmonic}} = 3f_{\mathrm{rf}}$. A reduced charge density in the bunches relaxes the heat load from beam-induced fields on vacuum components and reduces Touschek scattering (Section 4.1) and intrabeam scattering (Section 4.2) [Tavares et al., 2014].

Of equal importance as the bunch lengthening is the damping effect on the electron beam provided by the harmonic cavities in the MAX IV concept. As shown in Figure 6 of Paper **II**, harmonic cavities increase the spread of the incoherent synchrotron tune. Electrons oscillate therefore within a broader band of synchrotron frequencies, which suppresses coherent longitudinal particle motion which otherwise could limit the maximum stored current [Nielsen and Sessler, 1959]. The damping effect associated with this mechanism is referred to as *Landau damping*, a term originating from a similar effect in plasmas [Landau, 1946]. Both contributions of harmonic cavities, lengthening and damping, are essential in the MAX IV storage rings to reach design parameters [MAX IV Facility, 2010].

The accelerating voltage seen by the electron beam is given by the sum of the voltages of all cavities in the synchrotron. This assumption can be made since the motion in the longitudinal plane is slow compared to the revolution frequency. Although more than one cavity of each type is installed in the MAX IV 3 GeV storage ring (six main cavities, three harmonic cavities) to reach sufficiently high voltages, the individual voltages of each cavity type may be summed and considered as a single voltage V_T experienced by the beam, that is

$$V_T(\varphi) = V_{\mathrm{rf}} \sin\left(\varphi + \varphi_s\right) + k\, V_{\mathrm{rf}} \sin\left(n\varphi + n\phi_h\right). \tag{2.17}$$

Here the parameters k and ϕ_h define amplitude and phase in the harmonic cavity that is operated at the n-th harmonic of the main rf. An example with $n = 3$ is given in Figure 9.

The harmonic rf cavities in the MAX IV storage rings are passive cavities. Unlike the main rf cavities they are not powered by an external transmitter but by the stored beam itself. In a passive cavity, energy is transfered from the particle beam to the cavity, a process in which the beam is decelerated. The power loss to the harmonic cavities U_{h}, in addition to the power loss to radiation U_0, is the total power loss that is given by

$$U_T = U_0 + U_{\mathrm{h}}. \tag{2.18}$$

The additional power loss and the altered total voltage seen by the electron beam affects the synchronous phase and the longitudinal particle distribution in the bunch. Bunch lengthening is achieved by reducing the slope of the total rf voltage and the *flat potential* condition, as a special case, is reached if the first two derivatives of the rf voltage vanish around the synchronous phase [Hofmann and Myers, 1980] [Byrd and Georgsson, 2001].

A general derivation of the particle distribution in the bunch is shown in Section II of Paper **II**. A complication in the theoretical treatment of an rf system involving passive harmonic cavities is given by the fact that the voltage in such a cavity depends not only on cavity properties (shunt impedance and tuning) but also on properties of the electron beam. Mathematically, the excitation of fields in the cavity by the electron beam is expressed in a *form factor* as a function of the charge distribution in the bunch and is a measure of the bunch spectrum at the harmonic frequency $n\, f_{\mathrm{rf}}$. Thus, a dependency of the harmonic cavity voltage on the bunch shape is established while the bunch shape itself is given by the total rf voltage. This interdependence is not solved analytically but requires an iterative approach, leading to a result that fulfills *scalar self-consistency* (Section II A of Paper **II**).

Since the form factor defined in Eq. 17 of Paper **II** is a scalar, it does not account for a dephasing between the harmonic cavity and the charge distribution. This dephasing does, however, affect the excitation of fields in the passive harmonic cavity. The scalar

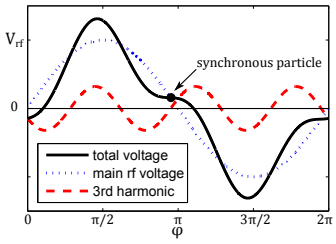

Figure 9. *Radio frequency voltage from main cavity and harmonic cavity. The reduced slope of the total voltage around the synchronous phase lengthens the particle distribution.*

self-consistency is therefore completed by a *form factor phase* in Section II B of Paper **II**, leading to *full self-consistency* and allowing the theoretical treatment of asymmetric bunch shapes. In the regime of harmonic cavity operation (high shunt impedance, large detuning) applied in the MAX IV 3 GeV ring, the fully self-consistent approach is mandatory for a correct description of longitudinal dynamics.

CHAPTER 3

EMITTANCE IN ELECTRON STORAGE RINGS

While emittances have been introduced and defined already in Sections 1.4 and 1.5.4, these definitions do not reveal the sources of emittance, i.e. the mechanisms that let particles occupy a certain phase space volume. The brief discussion in this chapter is focused on electron storage rings where the emission of SR by the stored electrons is the key ingredient to excitation as well as damping of particle motion.

Charged particles traveling at relativistic velocities that experience acceleration will emit SR. The total radiated power is described by Lienard's Formula [Jackson, 1999]

$$P_\gamma = \frac{q^2}{6\pi\varepsilon_0 c}\gamma_0^6\left(\dot{\boldsymbol{\beta}}^2 - (\boldsymbol{\beta}\times\dot{\boldsymbol{\beta}})^2\right), \tag{3.1}$$

where $\dot{\boldsymbol{\beta}} = \dot{\boldsymbol{v}}/c$ is the time derivative of the particle velocity divided by the speed of light, γ_0 is the Lorentz factor and ε_0 is the vacuum permittivity. Ultra-relativistic particles experience high rates of acceleration in deflecting magnetic fields, rather than in rf cavities, since magnetic fields, changing the direction of particle motion lead to substantially larger $\dot{\boldsymbol{\beta}}$ than the electric fields in rf cavities.

Synchrotron radiation in storage rings can be treated as incoherent since each electron in the bunch emits spontaneously. The radiation intensity therefore scales linearly with the number of electrons in the bunch. This is a good approximation as long as the bunch dimension is larger than the radiation wavelength, and describes both radiation from bending magnets and from IDs in a storage ring light source. The SR itself has interesting characteristics and is of great value for electron beam diagnostics, as discussed in Chapter 5.

3.1 Damping by emission of synchrotron radiation

The damping effect of SR can be explained even if the emission of SR is treated as a classical phenomenon, that means neglecting the

fact that it is actually emitted in discrete quanta of electromagnetic radiation, the photons. Furthermore it can be neglected that the radiation is emitted into a finite opening angle scaling like $1/\gamma$ around the velocity vector v of the particle ($1/\gamma \approx 0.17$ mrad in case of MAX IV 3 GeV storage ring). In this simplified picture, SR is emitted strictly in the direction of the particle velocity. A particle undergoing betatron oscillations can, unlike a particle following the reference trajectory, have a velocity (or momentum) component in the transverse plane. The momentum change from the emission of SR in the direction of particle velocity happens therefore in the transverse and the longitudinal plane with equal proportions. Considering that the longitudinal momentum is continuously recovered to nominal by rf cavity fields, which act only in the longitudinal direction, we can express the vertical momentum of a particle after emission as

$$p_{y1} \approx p_y \left(1 - \frac{dP}{P_0}\right), \tag{3.2}$$

where p_y is the vertical momentum before emission (scaled by the reference momentum P_0) and dP is the total momentum change. Using the definition for the action (cf. Eq. 1.51, but this time in the vertical plane), we find a change in vertical action by

$$dJ_y = -\left(\alpha_y y p_y + \beta_y p_y^2\right) \frac{dP}{P_0}, \tag{3.3}$$

which according to Eqs. 1.61 and Eq. 1.50 can be related to a change in vertical projected emittance given by

$$d\epsilon_y = \langle dJ_y \rangle = -\epsilon_y \frac{dP}{P_0}. \tag{3.4}$$

Related to a particle in a storage ring with a revolution period T_0, the change of vertical emittance in time can be written as

$$\frac{d\epsilon_y}{dt} \approx -\frac{U_0}{E_0 T_0} \epsilon_y, \tag{3.5}$$

where U_0 is the energy loss to SR per turn and $E_0 = P_0 c/\beta_0$ is the reference energy. The development of the vertical emittance over time is therefore an exponential damping with damping time τ_y:

$$\epsilon_y(t) = \epsilon_y(0) e^{-2t/\tau_y} \text{ with } \tau_y = 2\frac{E_0}{U_0} T_0. \tag{3.6}$$

An expression for the energy loss to SR per turn U_0 can be derived from Lienard's formula (Eq. 3.1), providing the power radiated by a relativistic particle on a circular trajectory with bending radius ρ:

$$P_\gamma = \frac{q^2 c}{6\pi\epsilon_0} \frac{\beta_0^4 \gamma_0^4}{\rho^2}. \tag{3.7}$$

This can be rewritten in the form

$$P_\gamma = \frac{C_\gamma c}{2\pi}\frac{\beta_0^4 E_0^4}{\rho^2} \text{ with } C_\gamma = \frac{q^2}{3\epsilon_0 (mc^2)^4}. \tag{3.8}$$

Integrating the radiation power over one revolution in the ring yields the energy loss to SR for one particle in one turn as

$$U_0 = \oint P_\gamma \, dt = \oint P_\gamma \frac{ds}{\beta_0 c} = \frac{C_\gamma}{2\pi}\beta_0^3 E_0^4 \oint \frac{1}{\rho^2} ds \tag{3.9}$$

or

$$U_0 = \frac{C_\gamma}{2\pi}\beta_0^3 E_0^4 I_2, \tag{3.10}$$

where the *second radiation intregral* is defined as

$$I_2 = \oint \frac{1}{\rho^2} ds. \tag{3.11}$$

Evaluating the second radiation integral is in principle straight forward. In a typical storage ring, however, the dipole field often varies along the bending magnets (magnet fringe fields or soft-end dipoles in case of the MAX IV 3 GeV storage ring matching magnets, see Figure 2 of Paper **IV**), which complicates integration. For the bare lattice (no insertion devices, only bending magnets contribute to I_2) of the MAX IV storage ring, the reference energy is $E_0 = 3$ GeV and the energy loss per turn per electron is $U_0 = 363.8$ keV, or 0.12‰ of the reference energy. This leads to a damping time $\tau_y \approx 29$ ms. Insertion devices increase energy loss and therefore provide additional radiation damping.

3.2 Damping and dispersion

In the approach shown in Section 3.1, dispersion is not taken into account. While in the vertical plane the dispersion might be negligible in many lattices, this is not the case in the horizontal plane due to dispersion from bending magnets. The horizontal action in presence of horizontal dispersion can be expressed as

$$J_x = \frac{1}{2}\left(\gamma_x \bar{x}^2 + 2\alpha_x \bar{x}\bar{p}_x + \beta_x \bar{p}_x^2\right) \tag{3.12}$$

where $\bar{x}$ and $\bar{p}_x$ are defined with respect to the off-momentum closed orbit:

$$\bar{x} = x - \eta_x \delta_p, \tag{3.13}$$

$$\bar{p}_x = p_x - \eta_{px} \delta_p. \tag{3.14}$$

After the emission of SR the horizontal coordinate and momentum are

$$\bar{x}_1 \approx \bar{x} + \eta_x \frac{dP}{P_0} \tag{3.15}$$

$$\bar{p}_{x1} \approx \bar{p}_x \left(1 - \frac{dP}{P_0}\right) + \eta_{px} \frac{dP}{P_0} \tag{3.16}$$

and the change of the action dJ_x, defined by

$$J_{x1} = J_x + dJ_x, \tag{3.17}$$

can be sorted by its order in momentum change from SR emission relative to the reference momentum:

$$dJ_x = -\omega_1 \frac{dP}{P_0} + \omega_2 \left(\frac{dP}{P_0}\right)^2. \tag{3.18}$$

The rate of change of the horizontal action over time is then given by

$$\frac{dJ_x}{dt} = -\omega_1 \frac{1}{P_0} \frac{dP}{dt} + \omega_2 \frac{dP}{P_0^2} \frac{dP}{dt}. \tag{3.19}$$

In the a classical model SR is emitted continuously hence that the power emitted during infinitely short time intervals approaches zero. The second term on the right hand side of Eq. 3.19 is therefore zero in the classical model and a pure damping effect is found, since the change of horizontal action over time is

$$\frac{dJ_x}{dt} = -\omega_1 \frac{1}{P_0} \frac{dP}{dt} \approx -\omega_1 \frac{P_\gamma}{E_0} \tag{3.20}$$

and the time average by integrating over a full turn is given by

$$\left\langle \frac{dJ_x}{dt} \right\rangle_t = -\frac{1}{T_0 E_0} \oint \omega_1 P_\gamma \left(1 + \frac{x}{\rho}\right) \frac{ds}{\beta_0 c}. \tag{3.21}$$

To evaluate this integral the bending radius ρ caused by magnetic fields must be known. Neglecting horizontal magnetic fields (from quadrupoles or skew quadrupoles), but retaining the gradient of the vertical field (for horizontal deflection of the particle) to first order, i.e.

$$B = B_0 + x \frac{\partial B_y}{\partial x}, \tag{3.22}$$

the integral becomes

$$\oint \left\langle \omega_1 P_\gamma \left(1 + \frac{x}{\rho}\right) \right\rangle \frac{ds}{\beta_0 c} \approx U_0 \left(1 - \frac{I_4}{I_2}\right) \epsilon_x, \tag{3.23}$$

where U_0 is the energy loss per turn (see Eq. 3.10) and I_4 is the *fourth synchrotron radiation integral*, defined as

$$I_4 = \oint \frac{\eta_x}{\rho} \left(\frac{1}{\rho^2} + 2k_1\right) ds. \tag{3.24}$$

Here k_1 is the normalized quadrupole gradient in the dipole field. Now the *horizontal damping time* becomes

$$\tau_x = \frac{2}{j_x}\frac{E_0}{U_0}T_0, \tag{3.25}$$

and the *horizontal damping partition number* is defined as

$$j_x = 1 - \frac{I_4}{I_2}. \tag{3.26}$$

In the absence of dispersion we find $j_x = 1$, which agrees with the result from Section 3.1. Quadrupole gradients in dipoles have, according to Eq. 3.24, a contribution to I_4. In many storage ring light sources the dipole magnets are realized as *combined function magnets*, providing a negative quadrupole gradient for vertical focusing in addition to the dipole field for bending. This leads to negative values for I_4 and increases the horizontal damping partition number, thereby reducing the horizontal emittance. This concept is also employed in the MAX IV 3 GeV storage ring, where $j_x \approx 1.8$.

A lattice where the vertical dispersion is non-zero will, according to Eq. 3.24 in its vertical representation, have a damping partition number $j_y \neq 1$. The vertical dispersion generated in the examples presented in Paper **I** leads, however, only to a minor decrease of j_y on the order 10^{-3}.

In the longitudinal degree of freedom a damping effect of synchrotron oscillations similar to the damping in the horizontal plane is found and can be described by

$$\tau_z = \frac{2}{j_z}\frac{E_0}{U_0}T_0 \tag{3.27}$$

with the *longitudinal damping partition number*

$$j_z = 2 + \frac{I_4}{I_2}. \tag{3.28}$$

The amount of damping by SR in a storage ring is constant, but can be distributed differently between the three planes. This general theorem is known as the *Robinson damping theorem* [Robinson, 1958] and is expressed by the statement that the sum of the damping partition numbers is constant:

$$j_x + j_y + j_z = 4. \tag{3.29}$$

3.3 Quantum excitation

Synchrotron radiation is emitted in photons, therefore the 'recoil' on the emitting particle (momentum conservation) occurs in discrete quanta dP. This has an exciting effect on particle motion that competes with the previously discussed damping effect. The *natural emittance* is the result of an equilibrium of excitation and damping.

3.3.1 Natural emittance

In Section 3.2 we neglected the second term on the right hand side of Eq. 3.19. Taking quantum effects into account this term does not vanish, since the momentum change in infinitesimally short times is non-zero due to the emission of discrete quanta of SR. The evaluation of this term requires knowledge of the number of photons emitted per time and per energy range, obtained from the intensity spectrum of the radiation [Jackson, 1999]. A detailed derivation is found in [Sands, 1970] and [Wolski, 2014]. The resulting change of the horizontal emittance in time can be described by

$$\frac{d\epsilon_x}{dt} = -\frac{2}{\tau_x}\epsilon_x + \frac{2}{j_x \tau_x} C_q \gamma_0^2 \frac{I_5}{I_2}. \tag{3.30}$$

The first term, depending on the horizontal emittance itself and on the horizontal damping rate τ_x, describes damping in the classical model. The additional term describes the quantum excitation due to emission of SR, where

$$C_q = \frac{55}{32\sqrt{3}} \frac{\hbar}{mc} \tag{3.31}$$

is a constant and

$$I_5 = \oint \frac{\mathcal{H}_x}{|\rho^3|} ds \tag{3.32}$$

is the *fifth synchrotron radiation integral* with the *chromatic invariant* or *dispersion invariant* in the horizontal plane, defined as

$$\mathcal{H}_x = \gamma_x \eta_x^2 + 2\alpha_x \eta_x \eta_{px} + \beta_x \eta_{px}^2. \tag{3.33}$$

An equilibrium between damping and excitation is found for $d\epsilon_x/dt = 0$, resulting in an *equilibrium emittance* or *natural emittance* in the horizontal plane given by

$$\epsilon_{x,0} = C_q \gamma_0^2 \frac{I_5}{j_x I_2}. \tag{3.34}$$

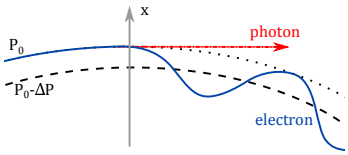

Figure 10. *Emittance generation by quantum excitation due to SR emission in presence of dispersion.*

The quantum excitation of the emittance can be understood as follows (see Figure 10): assume we follow a particle with momentum P_0 through a bending magnet, where the horizontal dispersion is non-zero. Within the bending magnet the particle emits a SR photon and thus suffers a momentum loss ΔP. It is then, however, not on the closed orbit that is associated with its new momentum $P_0 - \Delta P$. Consequently, the particle performs betatron oscillations around this closed orbit. Since the emission of SR is an incoherent process, particles within a bunch emit in different locations in the bending magnets and the betatron oscillations is incoherent as well. The particle distribution will therefore grow in phase space and lead to an increasing emittance, if not compensated by damping.

In case of non-zero vertical dispersion, a natural vertical emittance can be formulated accordingly. An expression for the natural vertical emittance as a projected emittance is, however, not applicable in the scheme presented in Paper **I** due to betatron coupling, which affects the vertical emittance independently of vertical dispersion. In presence of betatron coupling, a horizontal offset from the reference trajectory, originating from horizontal dispersion, results in both horizontal and vertical betatron oscillations, therefore exciting both planes to a certain extent. In a fully coupled lattice the natural emittance is therefore defined by the normal modes of the beam [Wolski et al., 2011]. This is shown in Section II B of Paper **I** for the normal mode II emittance, that is associated with, but not equal to, the vertical projected emittance. It is important to note here that it is still quantum excitation from SR emission by horizontal deflection of the electron beam that generates emittance.

3.3.2 Quantum limit emittance

Let us assume an ideal storage ring with no betatron coupling and vertical dispersion. Without excitation the radiation damping, described for the vertical plane in Section 3.1, would reduce the vertical emittance to very small values in short time, without ever reaching a lower limit. There is, however, an exciting effect on the beam, originating from the fact that SR is emitted in discrete photons into a finite opening angle, that has so far been neglected. Synchrotron radiation is therefore not emitted strictly in the direction of particle motion and a particle without any vertical momentum component will eventually emit a photon that has a non-zero vertical momentum component. For reasons of momentum conservation the particle will then have a non-zero vertical momentum. In an ensemble of electrons this effect is uncorrelated and leads to emittance growth. An equilibrium is reached at

$$\epsilon_{y,\min} = \frac{13}{55}\frac{C_q}{I_2}\oint \frac{\beta_y}{|\rho^3|}ds. \tag{3.35}$$

This minimum vertical emittance is of little relevance in most storage ring light sources, since the emittance growth from lattice imperfections dominate the vertical emittance in many storage rings. The numerical value for $\epsilon_{y,\min}$ is for the MAX IV 3 GeV ring approximately 0.05 pm rad [Streun], which is still one order of magnitude less than what might be achieved by correction of lattice imperfections.

CHAPTER 4

TOUSCHEK LIFETIME AND INTRABEAM SCATTERING

Electrons in a bunch perform (transverse) betatron oscillations and (longitudinal) synchrotron oscillations independently of each other. Depending on the particle density, there is a finite probability of collision. In such a case elastic scattering leads to a redistribution of momenta. In the so-called *Touschek event* [Bernardini et al., 1963] momentum is transfered from the fast betatron oscillations into the longitudinal dimension, such that the momentum acceptance is exceeded. Consequently, both particles are lost from the bunch. Even in cases of a momentum transfer where no loss of electrons occurs, the redistribution of momentum is usually associated with an emittance growth. This effect is called *intrabeam scattering*. Since both effects grow with electron density in the bunch, they are relevant in fourth generation synchrotron light sources and their ultralow-emittance lattices.

4.1 Touschek lifetime

The loss rate from Touschek events, the inverse of the Touschek lifetime, is given by [Streun, 1997]

$$\frac{1}{\tau} = \frac{r_e^2 c\, q}{8\pi e \gamma_0^3 \sigma_z C_0} \cdot \oint \frac{F\left(\left(\frac{\delta_{\mathrm{acc}}(s)}{\gamma_0 \sigma_{x'}(s)}\right)^2\right)}{\sigma_x(s)\sigma_y(s)\sigma_{x'}(s)\delta_{\mathrm{acc}}^2(s)} ds, \tag{4.1}$$

where r_e denotes the classical electron radius, c the vacuum velocity of light, e the elementary charge, C_0 the circumference of the storage ring, q the bunch charge and γ_0 the Lorentz factor of the beam. The horizontal and vertical rms beam sizes are σ_x and σ_y, respectively, while σ_z denotes the rms bunch length and $\delta_{\mathrm{acc}}(s)$ the local momentum acceptance.

The horizontal rms divergence in the center of the bunch ($x \approx 0$), where the particle density is highest and Touschek scattering events are most likely to occur, is given by

$$\sigma_{x'}(s) = \frac{\epsilon_x}{\sigma_x(s)} \sqrt{1 + \frac{\mathscr{H}_x(s)\,\sigma_\delta^2}{\epsilon_x}}\,, \tag{4.2}$$

where $\mathscr{H}_x(s)$ is the chromatic invariant (Eq. 3.33). Finally, the function $F(x)$ is defined as

$$F(x) = \int_0^1 \left(\frac{1}{u} - \frac{1}{2}\ln\left(\frac{1}{u}\right) - 1\right) \exp\left(-\frac{x}{u}\right)\, du. \tag{4.3}$$

4.1.1 Local momentum acceptance

The local momentum acceptance $\delta_{\text{acc}}(s)$ at any location of the storage ring can be defined either by the rf system or by the lattice acceptance, that means

$$\delta_{\text{acc}}(s) = \text{minimum}\left\{\delta_{\text{rf}}\,,\ \delta_{\text{acc,lattice}}(s)\right\}. \tag{4.4}$$

While the rf acceptance is constant, the lattice momentum acceptance needs to be evaluated along the storage ring. In a lattice with significant nonlinear dynamics (as in the MAX IV 3 GeV storage ring) this is done by particle tracking. The local lattice momentum acceptance is then found as the maximum momentum deviation a particle can acquire, while still surviving a certain number of turns without being lost. Computer codes for particle tracking in the 6-dimensional phase space are therefore based on symplectic, nonlinear transfer maps and efficient ways to determine particle loss, for example by exponential growth in the dynamical variables. Local momentum acceptances from particle tracking with the code Tracy-3 are shown in Figure 12 of Paper **I**. The rf acceptance is set to $\delta_{\text{rf}} = 7\%$, limiting only in the long straight sections, since the lattice momentum acceptance is significantly lower in the arcs. The Touschek lifetimes given in that paper have been determined based on the these local momentum acceptances.

4.1.2 Charge density and transverse momentum

The Touschek lifetime depends on the charge density in the bunch which can be expressed as

$$\rho_q(s) = \frac{q}{\sigma_x(s)\,\sigma_y(s)\,\sigma_z}. \tag{4.5}$$

The design goal of fourth generation synchrotron light sources, the reduction of the transverse emittances, is therefore competing with

a sufficient Touschek lifetime. On the other hand, a lower emittance is associated with less transverse momentum that can be transfered in a scattering event. For a sufficiently small horizontal emittance and a sufficiently large momentum acceptance, a regime where fourth generation storage ring light sources such as the MAX IV 3 GeV storage ring operate, the latter effect dominates and a horizontal emittance decrease is associated with an increase in Touschek lifetime [Leemann, 2014].

In the MAX IV 3 GeV storage ring the concept of long bunches is applied to relax the charge density, an approach based on a comparatively low main rf of 100 MHz and on the double rf system, described in detail in Paper **II**, to achieve sufficient Touschek lifetime.

The design value for the vertical emittance of 8 pm rad is motivated by a diffraction limited operation at 1 Å [MAX IV Facility, 2010]. Brightness and transverse coherence of SR from IDs can, nevertheless, be gained by further reducing the vertical emittance [Leemann and Eriksson, 2013]. The increased charge density from a lower vertical emittance, however, reduces Touschek lifetime. In the context of this trade-off between Touschek lifetime and SR brightness, the work presented in Paper **I** describes a scheme for vertical emittance adjustment and Touschek lifetime recovery.

4.2 Intrabeam scattering

While Touschek scattering events are associated with particle loss, there is a much more frequent of type scattering, based on the same fundamental principle but at small angles, which do not lead to particle loss. The momentum transfer in the bunch, however, blows up the beam emittance in 6-dimensional phase space, i.e. increasing the bunch length and energy spread as well as the transverse emittances. This effect is called *intrabeam scattering* (IBS) [Piwinski, 1974].

Similar to the quantum excitation from SR emission the effect of intrabeam scattering on the beam emittance can be expressed as IBS growth times

$$\frac{1}{T_i} = \frac{1}{2\epsilon_i}\frac{d\epsilon_i}{dt} \tag{4.6}$$

where $i = x$, y or z. Compared to growth times from SR emission, the IBS growth times are more complicated to determine since they depend on the beam emittance, and therefore an equilibrium must be found which usually requires iteration. IBS studies in the context of ultralow-emittance storage rings and the MAX IV 3 GeV storage ring, where IBS blowup of primarily the transverse emittances is mitigated by harmonic cavities, are presented in [Leemann, 2014].

CHAPTER 5

BEAM DIAGNOSTICS WITH SYNCHROTRON RADIATION

Synchrotron radiation that is inevitably produced in bending magnets around the storage ring is of great value for electron beam diagnostics. The entirely parasitic operation mode of SR-based diagnostic beamlines allows a high availability and enables continuous monitoring, as well as high-precision measurements. In this chapter the emission process of SR is briefly introduced and a few concepts are discussed that complement the work presented in Papers **III** and **IV**.

5.1 Theoretical background

Synchrotron radiation is emitted by electrons when they are transversely deflected (e.g. in a dipole magnets) at relativistic velocities. The observable angular distribution of the emitted electromagnetic fields is strongly affected by the Lorentz transformation from the relativistic rest frame of the electron to the laboratory frame [Jackson, 1999]. Synchrotron radiation is therefore emitted into a narrow cone in the direction of the electron motion with an opening angle that is usually estimated by $\theta_c \approx 1/\gamma$ around the critical frequency, given by [Schwinger, 1949]

$$\omega_c = \frac{3}{2}\gamma_0^3\left(\frac{c}{\rho}\right), \tag{5.1}$$

with the Lorentz factor γ_0, the vacuum speed of light c and the radius of curvature of the electron trajectory ρ. Half of the total SR power emitted in a dipole magnet is radiated below the critical photon energy $E_c = \hbar\omega_c$. Assuming a 3 GeV electron beam in a 0.53 T magnetic dipole field, we find a critical wavelength of $\lambda_c = 2\pi c/\omega_c \approx 0.37$ nm.

The narrow opening angle and the curved trajectory in the magnetic field let SR, emitted from a single electron, appear as a flash

with short duration in time than can be approximated by

$$\delta t \approx \frac{4\rho}{3c\gamma_0^3}. \tag{5.2}$$

The short pulse duration translates to a broad spectrum, for which an example is given in Figure 11. Since the pulse duration $\delta t \approx 4 \cdot 10^{-19}$ s is orders of magnitude shorter than the rms length of the electron distribution (several 10 ps in the MAX IV storage rings), the measurement of the bunch shape is not impaired by incoherently emitted SR from electrons within the bunch.

The radiation opening angle is, however, wavelength-dependent. In the low frequency range ($\omega \ll \omega_c$) a considerably wider opening angle θ_r is observed than for the critical wavelength:

$$\theta_r \approx \left(\frac{3c}{\omega\rho}\right)^{1/3} = \frac{1}{\gamma_0}\left(\frac{2\omega_c}{\omega}\right)^{1/3}. \tag{5.3}$$

In the UV-visible-IR spectral range the opening angle is therefore $\theta_r \approx 2$ to 3 mrad. The increased opening angle is essential for the operation of diagnostic beamlines in this spectral range, since the diffraction patterns in SR images, originating from few-mrad opening angles, are taken advantage of in order to resolve small electron beam sizes.

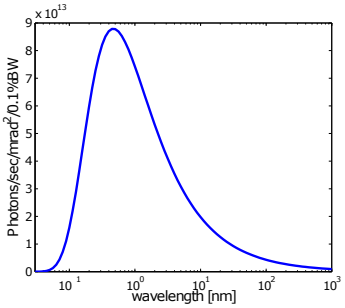

Figure 11. *Spectral flux of unpolarized SR from a 0.53 T bending magnet. The beam energy is 3 GeV and the current is 500 mA.*

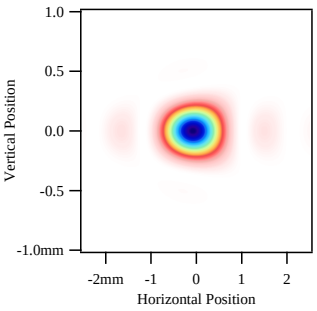

Figure 12. *Image of σ-polarized SR with Fraunhofer diffraction characteristics. $\alpha_H = 2$ mrad and $\lambda = 930$ nm. FBSF calculated in SRW.*

5.2 Synchrotron radiation imaging

With a suitable focusing element, for example a spherical lens, SR can be imaged onto an observation plane (for example a CCD sensor). This image is dominated by diffraction and polarization effects that are inherent to SR and need to be understood in order to make SR imaging a suitable electron beam diagnostic.

Let us assume the case of SR from a single electron in a dipole magnet that bends the trajectory in the horizontal plane. The vertical angular distribution of the emitted electric field will then be limited within the angle $2\theta_r$. The radiated electromagnetic field in the horizontal plane can be assumed to be uniform, a consequence of the 'search light effect' when the narrow opening angle is swept horizontally along the curved trajectory. In the horizontal plane an aperture is therefore assumed, that limits the horizontal acceptance angle α_H while the vertical acceptance angle α_V is chosen large enough to cover the entire radiated field. For sufficiently small horizontal opening angles an intensity distribution shown in Figure 12 is found. As a typical sign of Fraunhofer diffraction, the intensity distribution is proportional to $\mathrm{sinc}^2(x)$ in the horizontal plane [Hofmann and Méot, 1982] [Andersson et al., 2008].

The polarization of the electric field vector in Figure 12 is oriented horizontally and parallel to the bending plane. This is referred

to as *σ-polarized* SR. Radiation with a vertical electric field, the *π-polarized* SR, is emitted into an opening angle that is roughly equal to the one given in Eq. 5.3 and with approximately a fifth of the intensity of the horizontally polarized SR. The main characteristic of π-polarized SR is the phase shift of π between the upper and lower radiation lobe, while no vertically polarized SR is emitted in the bending plane. Imaged π-polarized SR is shown in Figure 13 with zero intensity across the bending plane (where the vertical position equals zero).

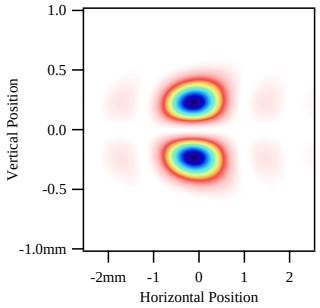

Figure 13. *Image of π-polarized SR with Fraunhofer diffraction characteristics. $\alpha_H = 2$ mrad and $\lambda = 930$ nm. FBSF calculated in SRW.*

5.2.1 Depth-of-field and filament beam

Restricting the horizontal opening angle minimizes the *depth-of-field effect*, a consequence of the longitudinal extension of the electron beam as the imaged object. The lens equation for imaging with a lens of focal length f is

$$\frac{1}{f} = \frac{1}{S_1} + \frac{1}{S_2} \tag{5.4}$$

with the distances S_1 from the lens to the object (electron beam) and S_2 from the lens to the image plane. Assuming a fixed lens and observation plane, the above relation can only be met for one location along the electron trajectory. Although a well-known effect in geometrical optics, the depth-of-field effect as shown in Figure 14 describes imaging of a longitudinally extended source with SR only in a simplified picture. The SR from a single electron radiated at differ-

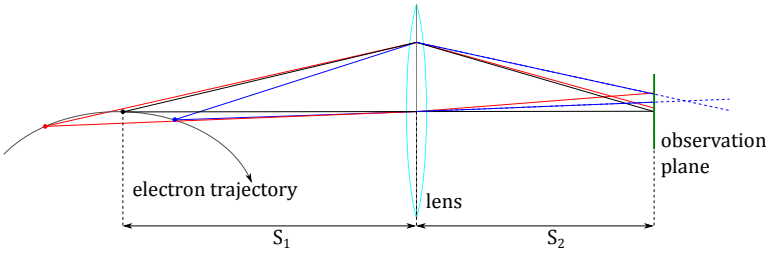

Figure 14. *Schematic of the depth-of-field effect when imaging SR from a dipole magnet.*

ent locations along its trajectory can not be described as radiation from a point source. Instead, the so-called *filament beam* as a longitudinally extended SR source is introduced. The single electron SR intensity distribution in the observation plane is then determined by the superposition of the electric fields, emitted from coherent point sources with magnitude and phase that are related to the emission point along the arc trajectory.

A characteristic of the image of a longitudinally extended source is the horizontally asymmetric diffraction pattern in the observation

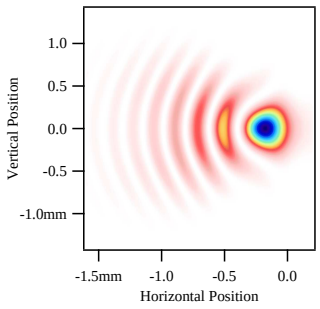

Figure 15. *Image of σ-polarized SR with depth-of-field characteristics. $\alpha_H = 18$ mrad and $\lambda = 930$ nm. FBSF calculated in SRW.*

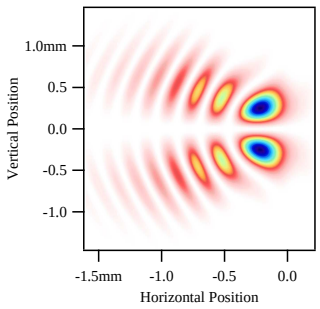

Figure 16. *Image of π-polarized SR with depth-of-field characteristics. $\alpha_H = 18$ mrad and $\lambda = 930$ nm. FBSF calculated in SRW.*

plane that is more pronounced the longer the source, contributing to the image, is. Figures 15 and 16 are calculated with identical parameters as Figures 12 and 13, except for the horizontal acceptance angle α_H that is increased from 2 mrad to 18 mrad. Imaging with radiation from wider horizontal angles is equivalent to an effective increase in the length of the curved filament beam as a radiation source. The horizontal asymmetry found in Figures 12 and 13 is therefore due to a superposition of fields in the observation plane that are radiated along the curved trajectory, and the intensity deviates clearly from $I \propto \mathrm{sinc}^2(x)$ behavior.

A model for the computation of SR has been outlined by [Chubar, 1995] where the radiation from arbitrary magnetic field distributions is calculated in the near-field regime. This has been implemented in the code Synchrotron Radiation Workshop (SRW) [Chubar]. Since the amplitude and phase relations of the emitted radiation are preserved according to wave optics and classical electrodynamics, the depth-of-field effect is fully accounted for in the image formation. Radiation propagation in free space, through apertures and the perfect thin lens, is implemented in the code and allows the precise calculation of the intensity distribution of focused bending magnet radiation.

Similar to the point spread function, being the response of an optical imaging system to a point source, the image of the filament beam (no transverse size) as the *filament beam spread function* (FBSF) can be calculated in SRW for a given electron beam in a magnetic field and imaged by an optical beamline. The images of SR until Figure 16 are FBSFs, calculated with the properties of the electron beam, the magnetic field and the elements for SR propagation that resemble those of the MAX IV 3 GeV storage ring diagnostic beamline in a simplified way and with an optical magnification of approximately −2.4. A main aspect of Papers **III** and **IV** is modeling a beamline in SRW, that resembles the physical diagnostic beamline, in order to arrive at a precise prediction of the FBSF, which is not accessible in the experiment.

5.2.2 Finite beam size

So far the SR from an electron beam with no transverse dimensions has been considered. Since the transversely extended electron beam is the result of (uncorrelated) SR emission by individual electrons (each described by the FBSF), a convolution of the electron distribution with the FBSF describes the image of the 'thick beam'. In principle an arbitrary electron distribution can be convoluted with the FBSF. The assumption of a Gaussian distribution of particles in transverse dimensions is, however, often adequate in electron storage rings.

An example is given for electron beam dimensions of $\sigma_x = 25$ µm and $\sigma_y = 11.5$ µm in Figure 17, where the FBSF is identical to

the one shown in Figure 15. The example is to be considered in the diffraction dominated regime, where the dimensions of the FBSF are of the same order as, or even larger than those of the electron beam. Therefore, the image of the extended beam resembles rather a smeared out FBSF than a Gaussian intensity distribution. If the source dimensions dominate over the diffraction, however, an image that resembles the shape of the source is expected, as in usual imaging of macroscopic objects.

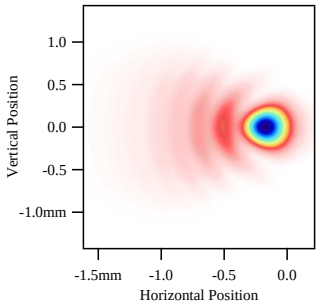

Figure 17. *Image of a transversely extended electron beam, calculated in SRW.*

5.3 Measurement principles

Measurements of the longitudinal bunch shape, being directly accessible as the time-dependent intensity of the SR pulse, are based on fast readout electronics (Section 5.3.5). The design criteria of the diagnostic beamline optics are, however, determined by imaging properties relevant for measurements of the transverse beam size. Besides the surface quality of optical components and mechanical stability, the imaging properties are determined by the FBSF of the diagnostic beamline. The FBSF depends on various parameters of which some are predetermined, such as the dipole field magnitude and distribution, or might, like the beam energy, depend on the current operation mode of the machine. Another set of parameters is given by the diagnostic beamline design, namely the focal length of the focusing element, the horizontal and vertical acceptance angles, polarization, wavelength (also bandwidth) and possibly diffraction obstacle properties. The fundamental target in the design of the diagnostic beamline is then to create a FBSF that, when convoluted with the electron beam distribution, generates an image that is as sensitive to the electron beam size as possible.

The difference between the horizontal and vertical plane in SR intensity distribution, but also in electron beam size, might require different or even opposed beamline parameters to optimize sensitivity in both planes. This must not necessarily lead to a compromise, since multiple operation modes of a diagnostic beamline, ideally simultaneously, are in principle possible.

For typical beam sizes in an ultralow-emittance storage ring of a few tens of micrometers and below, a SR image of the beam, taken in the UV-visible-IR spectral range, is dominated by diffraction effects. The consequence is a non-Gaussian image and possibly a characteristic diffraction fringe pattern. The contrast of this fringe pattern (or visibility) is easily accessible in experiment and can be related to the beam size by comparison with a calculated model.

5.3.1 Horizontal beam size

The horizontal beam size measurements presented in this work follow two different approaches. The measurements presented in

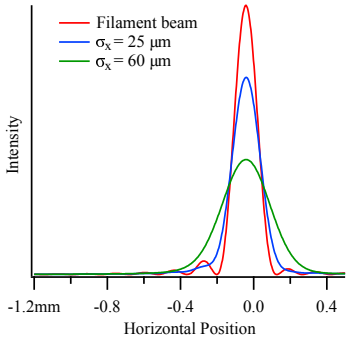

Figure 18 a). *SRW calculation for $\alpha_H = 2$ mrad, $\lambda = 325$ nm. Beam size determination at $\sigma_x \approx 60$ µm by the width of the imaged beam.*

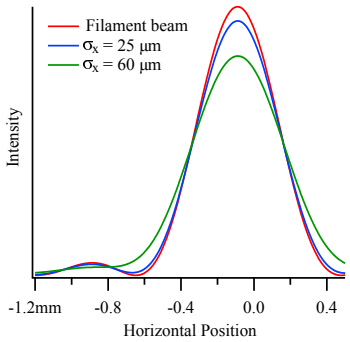

Figure 18 b). *SRW calculation for $\alpha_H = 2$ mrad, $\lambda = 930$ nm.*

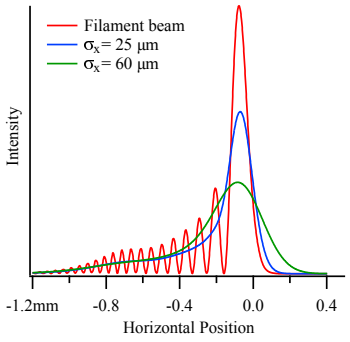

Figure 18 c). *SRW calculation for $\alpha_H = 18$ mrad, $\lambda = 325$ nm.*

Paper **III** have been performed at the SLS, a third generation synchrotron light source with a horizontal emittance of approximately 6 nm rad and a horizontal electron beam size at the source point of the diagnostic beamline of $\sigma_x \approx 60$ µm, where a method based on the width of the measured image is still applicable for beam size measurements. In the MAX IV 3 GeV storage ring with a horizontal emittance of approximately 0.3…0.2 nm rad, depending on the number and properties of IDs, horizontal beam sizes lower than 20 µm are to be expected in the SR source point of the diagnostic beamlines. A method based on the contrast of a horizontal fringe pattern has therefore been introduced and is presented in Paper **IV**.

An example, based on SRW calculations for a simplified model of a MAX IV diagnostic beamline at the 3 GeV storage ring, is given below to demonstrate in four examples a) to d), with horizontal intensity profiles given in Figures 18 a) to 18 d), how sensitivity to the horizontal beam size is achieved in different ranges of horizontal beam size.

a) At a horizontal opening angle of 2 mrad and a wavelength of 325 nm the FBSF shows the typical Fraunhofer diffraction pattern. A horizontal beam size of 60 µm is significantly wide compared to the FBSF and the width of the measured image has a sufficient sensitivity to the beam size. This is the measurement principle used in [Andersson et al., 2008] and in Paper **III**. The dominance of the FBSF, however, reduces the effect of the beam size on the width of the measured image the smaller the beam size is, and the method becomes insensitive to the beam size.

b) For the same horizontal opening angle and a wavelength of 930 nm the dependence of the width of the FBSF on the wavelength becomes apparent, a result of the wavelength-dependent angle the SR is radiated into. Compared to example a) the beam size sensitivity is largely lost already for wider electron beams. Naturally, imaging with shorter wavelength will have the opposite effect, with a potential to resolve smaller electron beams. The reduction of the measurement wavelength is, however, technically limited in a optical diagnostic beamline by transmission and reflection coefficients of the materials and by the sensor efficiency.

c) Increasing the horizontal opening angle of the beamline by a factor 9 compared to example a) leads to a significant depth-of-field contribution to the FBSF with a strong asymmetry and an extended fringe pattern. At an imaging wavelength of 325 nm the period of this fringe pattern is small compared to that of the horizontal beam sizes, and is, from convolution with the beam size, smeared out entirely.

d) Finally, combining the wide horizontal opening angle with an IR imaging wavelength, the fringe period becomes comparable to a beam size of 25 µm and the horizontal intensity profile of the image shows several local minima. A measurement method that relates the fringe pattern contrast to horizontal beam size is applicable.

5.3.2 Vertical beam size

At the SLS a vertical emittance of approximately 1 pm rad has been reached by minimization of vertical dispersion and betatron coupling [Aiba et al., 2012]. Ultra-low vertical emittance diagnostics with visible-UV SR has been demonstrated at the SLS using π-polarized SR [Andersson et al., 2008]. In the *π-polarization method*, the dependence of the contrast between the maxima and the central minimum to the vertical beam size is used for determination of the beam size, and allows resolutions of a few micrometers (see Figure 19). For this method short wavelengths in the near-UV range are applied to increase the sensitivity of the fringe contrast to the vertical beam size.

A modification of the π-polarization method is the *obstacle diffractometer* presented in Paper **III**. Here a diffraction obstacle is introduced to modify the FBSF of the diagnostic beamline in a way that is similar to the principle of the classical double-slit interferometer (Appendix A of Paper **III**). With the obstacle diffractometer methods the sensitivity to the vertical beam size can, under certain conditions, be enhanced. Furthermore, the σ-polarized SR becomes available for vertical beam size measurements. Another aspect of the obstacle diffractometer is that the diffraction obstacle is a part of the diagnostic beamline, that may be removed or modified solely to the requirements of the beam size measurement. Thus, the FBSF can be varied systematically in the experiment and the observed images are compared to those, calculated numerically, with similarly varied models of the beamline. The aim of the obstacle diffractometer is therefore mainly to provide complementary methods to measure the vertical beam size. The optional obstacle diffractometer is also applied in the MAX IV diagnostic beamlines and first results are presented in Paper **IV**.

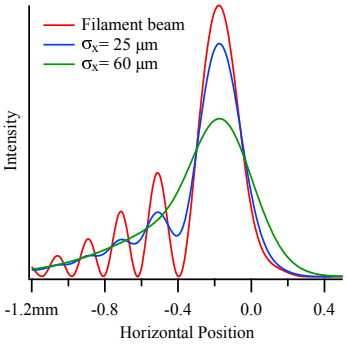

Figure 18 d). *$\alpha_H = 18$ mrad, $\lambda = 930$ nm. Beam size determination at $\sigma_x \approx 25$ μm by fringe contrast.*

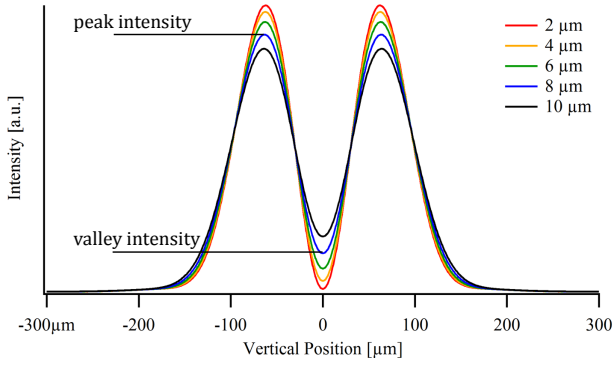

Figure 19. *Example of vertical intensity profiles of π-polarized SR at 325 nm for different vertical beam sizes.*

5.3.3 Dispersion

As described in Section 1.5.1, dispersion is the contribution of momentum deviation to the transverse coordinates and momenta of a particle. If the beam momentum is changed collectively dispersion can be observed as a transverse displacement of the beam. The dispersion in the SR source point is therefore be measured by the diagnostic beamline as a transverse displacement of the source.

In the linear approximation the relative momentum change $\Delta P/P_0$ is related to the relative change in main rf as follows:

$$\frac{\Delta f_{\mathrm{rf}}}{f_{\mathrm{rf}}} = -\alpha_c \frac{\Delta P}{P_0}. \tag{5.5}$$

Here α_c is the linear momentum compaction (Section 2.1). The beam displacement in the vertical plane Δy, caused by a relative momentum change, yields the vertical dispersion:

$$\eta_y = \frac{\Delta y}{\Delta P/P_0}. \tag{5.6}$$

As an example, data recorded during a vertical dispersion measurement in the MAX IV 3 GeV storage ring is shown in Figure 20. The ±50 Hz variation of the main rf in 11 steps caused a relative momentum change of approximately 0.33% and changed the vertical beam position by approximately 14 μm. The position of the beam centroid is hereby derived from same fits to the measured image that are applied for the evaluation of the fringe contrast (Section 5.3.4). Linear fits to the measured beam positions result in a linear vertical dispersion of $\eta_y \approx 4.3$ mm[1] in this example. The pattern of frequency change is chosen to detect and compensate for possible drifts of the detected beam position, that are not related to the rf change.

5.3.4 Image evaluation

The process of beam size determination from a recorded image is briefly described in this section for a vertical beam size measurement with the π-polarization method. With modifications and adaptations, however, this procedure is also applicable for processing obstacle diffractometer images (Paper **III**), and for the determination of the horizontal beam size by evaluation of diffraction patterns (Paper **IV**).

We assume that an image of the electron beam is recorded and a background image[2] is subtracted from the raw image as a first step. The vertical intensity profile, shown in Figure 21, is derived from the

[1] This amount of vertical dispersion is expected since lattice imperfections were largely uncorrected at the time of this measurement.

[2] For example an image taken at exactly the same parameters but without stored beam

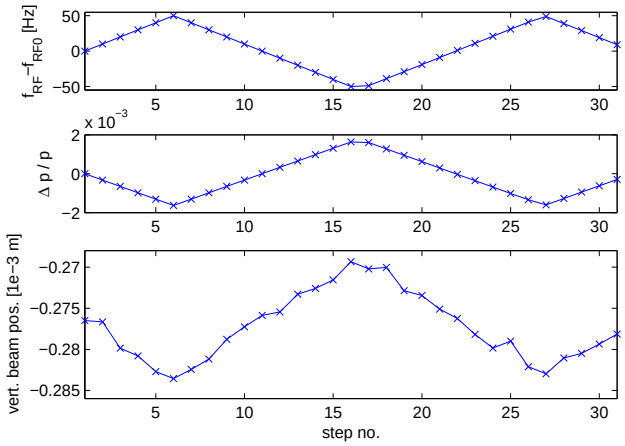

Figure 20. *Example of a vertical dispersion measurement with a diagnostic beamline at the MAX IV 3 GeV ring. The variation of the rf changes the electron beam momentum. The vertical beam displacement is then related to vertical dispersion.*

background-subtracted image by a line-by-line averaging over a narrow column around the intensity maximum to reduce pixel noise. The width of this column needs to be chosen with care, especially for asymmetric diffraction patterns, since only pixel noise but no diffraction effects should be averaged out.

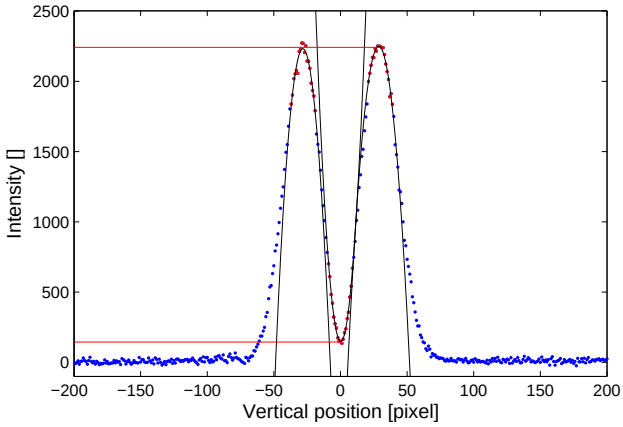

Figure 21. *Vertical profile with fitted parabolas. The intensity ratio between minimum and maxima (valley-to-peak ratio) is 6.4%.*

As a next step the minima and maxima of the diffraction pattern

are identified and fitted. The example in Figure 21 shows parabolas, being a convenient choice of fit function, fitted to both maxima and the central minimum. The number of data points (red in the figure) considered for each fit is chosen depending on the width of the diffraction pattern compared to the pixel size. For each of the three extrema the vertical position and the intensity are derived from the fit parameters and a random error on position and intensity is obtained by error propagation with an estimate of the covariance matrix of the fit parameters. The directly observable position in the image plane is then translated into the position of the source, while further steps are required to obtain the beam size. As an experimentally accessible measure of the fringe contrast, the *valley-to-peak ratio* is defined as the intensity ratio $r_{\mathrm{v/p}} = \langle I_{\mathrm{min}} \rangle / \langle I_{\mathrm{max}} \rangle$, where an average is taken over two maxima. The result is the measured valley-to-peak ratio and its random error.

Translating the measured valley-to-peak ratio into a beam size requires SR images, calculated with a modeled diagnostic beamline, that resembles its physical counterpart. Calculating SR images for a range of beam sizes and obtaining valley-to-peak ratio as a function of beam size, a *lookup table* is created. For the evaluation of measurement data it is useful to apply a fit to the lookup table. A convenient choice of fitting is:

$$r_{\mathrm{v/p}}(\sigma_y) = c_1 + c_2 \exp\left[-\left(\frac{\sigma_y - c_3}{c_4}\right)^2\right], \tag{5.7}$$

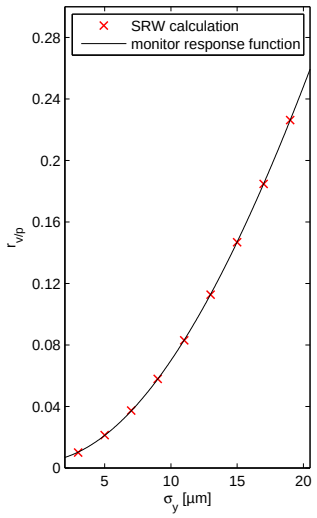

Figure 22. *Example of a monitor response function for vertical beam size measurement, obtained by a fit to SRW-calculated data.*

referred to as the *monitor response function*, which connects the measurable valley-to-peak ratio to the (vertical) beam size. Thus, this approach allows the characterization of a given diagnostic beamline for various setups by four parameters $c_1 \ldots c_4$. The function in Eq. 5.7 proved to be a suitable fit to the lookup table, providing better results than a polynomial fit. Figure 22 shows an example of a monitor response function for vertical beam size measurements with the π-polarization method, and in Figure 2 and 4 of Paper **III** the monitor response functions are shown for several methods, applicable for vertical beam size measurements, at the SLS diagnostic beamline.

By inversion of Eq. 5.7, a closed expression for the beam size as a function of the valley-to-peak ratio is obtained, that completes the image evaluation process described above:

$$\sigma_y(r_{\mathrm{v/p}}) = c_3 + c_4 \sqrt{\ln\left(\frac{c_2}{r_{\mathrm{v/p}} - c_1}\right)} \tag{5.8}$$

Based on this expression, the random error on the valley-to-peak ratio is propagated to a random error on the vertical beam size. The beam size and its standard deviation can therefore be stated for a single measurement, as shown for a vertical beam size measurement series in Figure 7 of Paper **III**.

5.3.5 Longitudinal bunch shape

The rms bunch length in the MAX IV 3 GeV storage ring with a natural energy spread of $\sigma_\delta \approx 0.77 \cdot 10^{-3}$ and a peak rf voltage of $V_{\mathrm{rf}} = 1.8$ MV is approximately 29 ps. This natural bunch length can be observed on a stable beam at low current, where the excitation of fields in the harmonic cavities is low. At design current, a bunch lengthening by up to a factor 5 is achievable. Synchrotron radiation based bunch shape measurements require therefore time-resolved intensity measurements at signals of a few 10 ps width. Two approaches, the single-shot and the sampling technique, are available.

Single-shot measurements with a 12 GHz photo diode have been performed but are limited by the bandwidth of the 4 GHz oscilloscope used to analyze the photo diode signal. Although not sufficient for resolving the bunch profile, the single-shot technique allows the evaluation of longitudinal bunch stability in terms of coherent synchrotron motion. For this purpose the oscilloscope is triggered with the revolution clock of the storage ring, which is synchronized to the rf system. Only in case of a longitudinally stationary electron bunch, that is a rigid bunch with no detectable motion of the bunch centroid, the sampling technique is applicable.

A sampling oscilloscope, the Hamamatsu OOS-001, is triggered with the revolution period and samples the intensity profile of the SR from one specific electron bunch over several thousand turns. In the detector part of the device, the incident SR is focused and converted into photo-electrons by a photo-cathode. The emitted electrons are deflected by a time-dependent electric field, generated between two plates. The fast sweep of the electrons by the field, combined with a narrow slit, allows a time resolution as low as 4 ps, depending on the operation mode of the sampling oscilloscope. Electrons passing the slit are converted to light by a phosphor screen. The light is then transformed to an electric signal by a photomultiplier tube. With sufficiently long signal accumulation and averaging, the noise level can be suppressed and bunch profile measurements at single-bunch currents below 0.1 mA are possible.

Bunch shapes measured with the sampling oscilloscope at MAX III, a third generation storage ring light source, are shown in Figure 9 of Paper **II**. The figure compares the bunch shapes, computed with the theoretical model presented in the paper, with measurements for three cases of bunch lengthening by harmonic cavities. A bunch shape, measured with the same instrument at the MAX IV 3 GeV storage ring at low current, is shown in Figure 8 of Paper **IV**. The deviation from the natural bunch length quoted above is mainly due to a lower rf voltage.

5.3.6 Emittance and energy spread

A diagnostic beamline based on SR imaging measures the transverse beam size, from which an emittance, here in the vertical plane, is derived as follows:

$$\mathbb{E}_y(s) = \frac{\sigma_y^2(s) - \eta_y^2(s)\sigma_\delta^2}{\beta_y(s)} \tag{5.9}$$

This so-called *apparent emittance* [Franchi et al., 2011] from beam profile measurements is equal to the projected emittance, given in Section 1.4, only in the absence of coupling. In such a situation the apparent emittance is also equal to the normal mode emittance, introduced in Section 1.5.4, and these distinctions become obsolete, since $\epsilon = \mathscr{E} = \mathbb{E}$. Betatron coupling and spurious vertical dispersion from lattice imperfections should therefore be minimize as far as possible, in order to access the normal mode emittance $\mathscr{E}_{\mathrm{II}}$ as the invariant of vertical particle motion in a measurement with a diagnostic beamline, since then $\mathbb{E}_y \rightarrow \mathscr{E}_{\mathrm{II}}$. Due to the small emittance ratio $\mathscr{E}_{\mathrm{II}}/\mathscr{E}_{\mathrm{I}}$, the horizontal emittance is less affected by betatron coupling and $\mathbb{E}_x \approx \mathscr{E}_{\mathrm{I}}$ is usually a good approximation.

While the beam sizes and the dispersions are measured with the diagnostic beamline itself, the local values of the beta functions are obtained by other means. Well-known procedures are the measurement of the betatron tune shifts by variation of the gradient in quadrupole magnets, and the measurement and fit of the orbit response matrix, following for example the LOCO approach [Safranek, 1997]. The beta functions from either of these methods need to be interpolated from the quadrupole magnet or the beam position monitor, to the SR source point of the diagnostic beamline.

The beam energy spreads for the emittances presented in Papers **III** and **IV** have been calculated from a computer model of the storage ring, since no reliable diagnostics had so far been available without major effort. With two diagnostic beamlines in locations of different optics functions, however, the emittance can be obtained without the need for a model based energy spread. From Eq. 5.9 formulated for the horizontal plane follows for the horizontal apparent emittance

$$\mathbb{E}_x = \frac{\sigma_{x,2}^2 - \left(\frac{\eta_{x,2}}{\eta_{x,1}}\right)^2 \sigma_{x,1}^2}{\beta_{x,2} - \left(\frac{\eta_{x,2}}{\eta_{x,1}}\right)^2 \beta_{x,1}}, \tag{5.10}$$

where the local values of the beta function $\beta_{x,1}$ and $\beta_{x,2}$ at source point 1 and 2, respectively, are obtained in the traditional way. Similarly, the beam energy spread is given by

$$\sigma_\delta = \left[\frac{\sigma_{x,2}^2 - \left(\frac{\beta_{x,2}}{\beta_{x,1}}\right) \sigma_{x,1}^2}{\eta_{x,2}^2 - \left(\frac{\beta_{x,2}}{\beta_{x,1}}\right) \eta_{x,1}^2} \right]^{1/2} . \tag{5.11}$$

In the MAX IV 3 GeV storage ring a diagnostic beamline with the source point in the first matching cell dipole of achromat 20 and local values of the optics functions $\eta_{x,2} \approx 1$ mm and $\beta_{x,2} \approx 1.7$ has been installed (Paper **IV**). The installation of another diagnostic beamline with source point in the fifth unit cell dipole of achromat 2, where $\eta_{x,1} \approx 25$ mm and $\beta_{x,1} \approx 1.3$ m is being prepared. For small dispersion ratios $\eta_{x,2}/\eta_{x,1}$, Eqs. 5.10 and 5.11 can be approximated as follows:

$$\mathbb{E}_x = \frac{\sigma_{x,2}^2}{\beta_{x,2}}, \tag{5.12}$$

$$\sigma_\delta = \frac{\sqrt{\sigma_{x,1}^2 - \mathbb{E}_x \beta_{x,1}}}{\eta_{x,1}}. \tag{5.13}$$

Covering the entire 6-dimensional phase space by beam diagnostics is of special interest in an ultralow-emittance storage ring in the context of intrabeam scattering.

CHAPTER 6

SUMMARY AND OUTLOOK

A method allowing horizontal emittance diagnostics in electron storage rings by near-visible SR imaging has been introduced. The fringe pattern from imaged SR in the near-IR spectral range is sufficiently sensitive to the horizontal beam size of $\sigma_x \approx 24\,\mu\text{m}$ at a diagnostic beamline in the MAX IV 3 GeV storage ring. Preliminary results from measurements applying this method are presented in Paper **IV**, indicating, however, experimental imperfections. Subject to further commissioning of the diagnostic beamline is therefore mainly the improvement of SR optics alignment. Furthermore, the numerical model applied so far is insufficient in the given case of varying transverse beam sizes along the longitudinally extended radiation source. Further development of the numerical simulation is therefore required to enable the precise calculation of the image formation of the MAX IV matching cell dipole SR at large horizontal opening angles, considering the variation of the beta functions within the observable range of the diagnostic beamline (Figure 2 of Paper **IV**). Measurements of the horizontal beam sizes at two locations of different dispersions and beta functions are envisaged on both MAX IV storage rings and will enable experimental access to the beam energy spread.

Vertical beam size measurements with SR in the few micrometer range have been performed with a diagnostic beamline at the Swiss Light Source and are presented in Paper **III**. The obstacle diffractometer methods have been useful in finding systematic deviations in beam size measurements, leading to a better understanding and more accurate modeling of the diagnostic beamline in the simulation code. The same principle, applied in the MAX IV 3 GeV storage ring diagnostic beamline, gives an estimate of systematic measurement errors (see Table 1 of Paper **IV**) and allows for determination and correction of error sources. The progress in storage ring commissioning in terms of reduction of betatron coupling and spurious vertical dispersion, leading to smaller vertical beam sizes, will there-

fore be accompanied by the commissioning of the diagnostic beamlines to eventually enable vertical beam size measurements at 2 to 3 μm.

The bunch lengthening by harmonic cavities, required for the operation of the MAX IV 3 GeV storage ring, has been studied experimentally at the MAX III storage ring with time-resolved diagnostics of SR, and good agreement with simulations is found (Paper **II**). Subject to this paper, however, is a wider range of harmonic cavity parameters that will be investigated experimentally at the MAX IV 3 GeV storage ring. Although the sampling technique used for the bunch shape measurements is applicable only at a longitudinally stable beam, it does enable the determination of the longitudinal charge distribution with high precision. Applying a complementary measurement with a photo diode and in a single passage of the bunch, possible longitudinal bunch oscillations can be studied.

A scheme for vertical emittance control has been introduced in Paper **I**, that raises the vertical emittance to a desired level to restore Touschek lifetime while maintaining good source properties at the insertion devices. The skew quadrupoles suggested for this scheme are available in the MAX IV 3 GeV storage ring today. The effectiveness of closed controlled dispersion bumps can, however, only be tested experimentally once spurious vertical dispersion and betatron coupling are sufficiently reduced. As storage ring commissioning progresses, this scheme may be implemented and verified experimentally in terms of vertical dispersion increase in the arcs, Touschek lifetime increase and possibly IBS-induced emittance blowup reduction by the appropriate diagnostics. Eventually, the effectiveness and eligibility of the successive closed vertical dispersion bump scheme will be decided during machine operation for SR production.

ACKNOWLEDGMENTS

While working on this thesis I have received help and support from many people, from my supervisors, colleagues, friends and family. Here I take the opportunity to express my gratitude to them.

I am deeply grateful for the supervision and the guidance I have received from Dr. Åke Andersson, and for the invaluable professional experience I have gained in many discussions with him. He has given me the opportunity to conduct my studies independently in several projects, and he has provided great support and encouragement when needed. I am looking back on five inspiring years of study and research work under his guidance.

I express my sincere gratitude to Dr. Simon Leemann for the highly motivating and productive studies he has enabled me to conduct under his supervision, studies that have resulted in a substantial contribution to this work.

Dr. Lars Malmgren is acknowledged for guiding me in a project early on in my time at Maxlab. I thank Prof. Dr. Sverker Werin, head of the department, who has given me access to education, research and professional experience.

In a collaboration with the Paul Scherrer Institute in Switzerland I have been invited many times to work in the groups of Dr. Andreas Streun and Dr. Volker Schlott. I am grateful that I have been given the opportunity to conduct experimental studies at the Swiss Light Source diagnostic beamlines with my collaborators.

Thanks to my colleagues at the MAX IV Laboratory I have experienced a work environment in which I have received help and assistance in many concerns. My special thanks go to all colleagues involved in the design and the installation of the diagnostic beamlines, and to everyone participating in the development and the operation of the accelerators. Dr. Pedro F. Tavares is acknowledged for his perspicuous explanations whenever things have gotten too complicated for me. Many thanks go to Dr. Anders Rosborg for the instructive Monday night shifts that we have spent at the old MAX III, where I have gained first storage ring experience.

I am thankful for the good times we have had as the MAX IV student group, with Teresia Olsson, Alan Mak, Walan Grizolli and Christian Stråhlman. My thanks go to Joel Andersson for contributing his views on things from another perspective, and to Jonas Björklund Svensson for sharing common interests on two wheels. Olivia Karlberg has been the best travel companion, be it to Idaho Springs or to Ica Tuna. Many thanks go to Galina Skripka for her company and her advice and encouragement during our time in Lund.

Liebe Francis, für Dein Verständnis, Deine Geduld, und für das Zuhause, das Du uns schaffst, bin ich Dir sehr dankbar. Danke für die Stillen Nächte in Kaarz, liebe Ružica und lieber Broder, für Eure tatkräftige Unterstützung und für die vielen Rufe zur Kunst. Danke für Deine Fürsorge aus der Ferne, liebe Cornelie, ob in Päckchenform oder als Anruf.

BIBLIOGRAPHY

M. Aiba, M. Böge, N. Milas, and A. Streun. Ultra low vertical emittance at SLS through systematic and random optimization. *Nuclear Instruments and Methods in Physics Research Section A*, 694:133 – 139, 2012.

E. Al-Dmour, J. Ahlback, D. Einfeld, P. F. Tavares, and M. Grabski. Diffraction-limited storage-ring vacuum technology. *Journal of Synchrotron Radiation*, 21(5):878–883, 2014.

L. W. Alvarez. The design of a proton linear accelerator. *Physical Review*, 70:799, 1946.

Å. Andersson, M. Böge, A. Lüdeke, V. Schlott, and A. Streun. Determination of a small vertical electron beam profile and emittance at the Swiss Light Source. *Nuclear Instruments and Methods in Physics Research A*, 591:437–446, 2008.

J. Bengtsson. Tracy-2 User's Manual. Unpublished.

J. S. Berg, R. L. Warnock, R. D. Ruth, and E. Forest. Construction of symplectic maps for nonlinear motion of particles in accelerators. *Physical Review E*, 49:722–739, 1994.

C. Bernardini, G. F. Corazza, G. Di Giugno, G. Ghigo, J. Haissinski, P. Marin, R. Querzoli, and B. Touschek. Lifetime and beam size in a storage ring. *Physical Review Letters*, 10:407–409, 1963.

J. Biasci, J. Bouteille, N. Carmignani, J. Chavanne, D. Coulon, Y. Dabin, F. Ewald, L. Farvacque, L. Goirand, M. Hahn, J. Jacob, G. LeBec, S. Liuzzo, B. Nash, H. Pedroso-Marques, T. Perron, E. Plouviez, P. Raimondi, J. Revol, K. Scheidt, and V. Serrière. A low-emittance lattice for the ESRF. *Synchrotron Radiation News*, 27 (6):8–12, 2014.

J. M. Byrd and M. Georgsson. Lifetime increase using passive harmonic cavities in synchrotron light sources. *Phys. Rev. ST Accel. Beams*, 4:030701, 2001.

N. Christofilos. Focussing system for ions and electrons, 1950. US Patent 2,736,799. Published 1956.

O. V. Chubar. Synchrotron Radiation Workshop. `http://www.esrf.eu/Accelerators/Groups/InsertionDevices/Software/SRW`.

O. V. Chubar. Precise computation of electron beam radiation in nonuniform magnetic fields as a tool for beam diagnostics. *Review of Scientific Instruments*, 66(2): 1872–1874, 1995.

J. D. Cockcroft and E. T. S. Walton. Experiments with high velocity positive ions. (I) further developments in the method of obtaining high velocity positive ions. *Proceedings of the Royal Society of London A: Mathematical, Physical and Engineering Sciences*, 136(830):619–630, 1932.

E. D. Courant and H. S. Snyder. Theory of the alternating-gradient synchrotron. *Annals of Physics*, 3(1):1 – 48, 1958.

E. D. Courant, M. S. Livingston, and H. S. Snyder. The strong-focusing synchroton - A new high energy accelerator. *Physical Review*, 88:1190–1196, 1952.

F. Curbis, N. Čutić, M. Eriksson, O. Karlberg, F. Lindau, A. Mak, E. Mansten, S. Thorin, and S. Werin. Extension of the MAX IV Linac for a Free Electron Laser in the X-ray Region. In *Proceedings of the 4th International Particle Accelerator Conference (IPAC 2013)*, page TUPEA050, 2013.

D. Einfeld and M. Plesko. Design of a diffraction-limited light source. In *Proceedings of SPIE*, pages 201–212, 1993.

D. Einfeld, J. Schaper, and M. Plesko. Design of a diffraction limited light source (DIFL). In *Proceedings of the Particle Accelerator Conference (PAC) 1995), TPG08*, 1995.

D. Einfeld, M. Plesko, and J. Schaper. First multi-bend achromat lattice consideration. *Journal of Synchrotron Radiation*, 21(5):856–861, 2014.

F. R. Elder, A. M. Gurewitsch, R. V. Langmuir, and H. C. Pollock. Radiation from electrons in a synchrotron. *Physical Review*, 71:829–830, 1947.

E. Forest and R. D. Ruth. Fourth-order symplectic integration. *Physica D: Nonlinear Phenomena*, 43(1):105 – 117, 1990.

A. Franchi, L. Farvacque, J. Chavanne, F. Ewald, B. Nash, K. Scheidt, and R. Tomás. Vertical emittance reduction and preservation in electron storage rings via resonance driving terms correction. *Phys. Rev. ST Accel. Beams*, 14:034002, 2011.

H. Goldstein, C. Poole, and J. Safko. *Classical Mechanics*. Addison Wesley, 2002. ISBN 9780201657029.

R. Hettel. DLSR design and plans: an international overview. *Journal of Synchrotron Radiation*, 21(5):843–855, 2014.

A. Hofmann and F. Méot. Optical resolution of beam cross-section measurements by means of synchrotron radiation. *Nuclear Instruments and Methods in Physics Research*, 203(1):483 – 493, 1982.

A. Hofmann and S. Myers. Beam dynamics in a double RF system. (CERN-ISR-TH-RF-80-26), 1980.

J. D. Jackson. *Classical Electrodynamics Third Edition*. 1999.

M. Johansson, B. Anderberg, and L.-J. Lindgren. Magnet design for a low-emittance storage ring. *Journal of Synchrotron Radiation*, 21(5):884–903, 2014.

W. Joho, P. Marchand, L. Rivkin, and A. Streun. Design of a Swiss Light Source (SLS). In *in Proceedings of the European Particle Accelerator Conference (EPAC) 1994)*, pages 627–629, 1994.

K. J. Kim. Optical and power characteristics of synchrotron radiation sources [also Erratum 34(4)1243(Apr1995)]. *Optical Engineering*, 34(2):342–352, 1995.

L. Landau. On the vibrations of the electronic plasma. *Journal of Physics USSR*, 10, 1946.

E. O. Lawrence and N. E. Edlefsen. *Science*, 72:376–377, 1930.

S. C. Leemann. Interplay of Touschek scattering, intrabeam scattering, and rf cavities in ultralow-emittance storage rings. *Phys. Rev. ST Accel. Beams*, 17:050705, 2014.

S. C. Leemann and M. Eriksson. Coupling and brightness considerations for the MAX IV 3 GeV storage ring. In *Proceedings of PAC 2013, Pasadena, USA*, 2013.

S. C. Leemann, Å. Andersson, M. Eriksson, L.-J. Lindgren, E. Wallén, J. Bengtsson, and A. Streun. Beam dynamics and expected performance of Sweden's new storage-ring light source: MAX IV. *Phys. Rev. ST Accel. Beams*, 12:120701, 2009.

L. Liu, N. Milas, A. H. C. Mukai, X. R. Resende, and F. H. de Sá. The Sirius project. *Journal of Synchrotron Radiation*, 21(5):904–911, 2014.

MAX IV Facility. MAX IV Detailed Design Report. `http://www.maxiv.lu.se/publications/`, 2010.

C. E. Nielsen and A. M. Sessler. Longitudinal space charge effects in particle accelerators. *Review of Scientific Instruments*, 30(2):80–89, 1959.

A. Piwinski. Intra-beam scattering. In *Proceedings of the 9th International Conference on High Energy Accelerators (Stanford, CA, USA)*, page 405, 1974.

K. W. Robinson. Radiation effects in circular electron accelerators. *Physical Review*, 111:373–380, 1958.

J. Safranek. Experimental determination of storage ring optics using orbit response measurements. *Nuclear Instruments and Methods in Physics Research Section A*, 388(1–2):27 – 36, 1997.

M. Sands. The physics of electron storage rings - an introduction. Tech. Rep. SLAC 121, Stanford Linear Accelerator Center, Stanford, USA, 1970.

P. Schmüser, M. Dohlus, and J. Rossbach. *Ultraviolet and Soft X-Ray Free-Electron Lasers*. Springer, Berlin, Germany, 2009.

J. Schwinger. On the classical radiation of accelerated electrons. *Physical Review*, 75: 1912–1925, 1949.

C. Steier. Possibilities for a diffraction-limited upgrade of a soft x-ray light source. *Synchrotron Radiation News*, 27(6):18–22, 2014.

A. Streun. OPA lattice design code. `https://ados.web.psi.ch/opa/`.

A. Streun. SLS Note 18/97. `https://ados.web.psi.ch/slsnotes/sls1897a.pdf`, 1997.

P. F. Tavares, S. C. Leemann, M. Sjöström, and Å. Andersson. The MAX IV storage ring project. *Journal of Synchrotron Radiation*, 21(5):862–877, 2014.

S. Thorin, J. Andersson, F. Curbis, M. Eriksson, O. Karlberg, D. Kumbaro, E. Mansten, D. Olsson, and S. Werin. The MAX IV Linac. In *Proceedings, 27th Linear Accelerator Conference, LINAC2014*, 2014.

R. Q. Twiss and N. H. Frank. Orbital stability in a proton synchrotron. *Review of Scientific Instruments*, 20(1):1–17, 1949.

S. Werin, S. Thorin, M. Eriksson, and J. Larsson. Short pulse facility for MAX-lab. *Nuclear Instruments and Methods in Physics Research Section A*, 601(1–2):98 – 107, 2009.

H. Wiedemann. *Particle Accelerator Physics*. Springer, Berlin, Heidelberg, Germany, 2007.

A. Wolski. Alternative approach to general coupled linear optics. *Phys. Rev. ST Accel. Beams*, 9:024001, 2006.

A. Wolski. *Beam dynamics in high energy particle accelerators*. Imperial College Press, London, UK, 2014.

A. Wolski, D. Rubin, D. Sagan, and J. Shanks. Low-emittance tuning of storage rings using normal mode beam position monitor calibration. *Phys. Rev. ST Accel. Beams*, 14:072804, 2011.

COMMENTS ON THE PAPERS

I **Improving Touschek lifetime in ultralow-emittance lattices through systematic application of successive closed vertical dispersion bumps**
This paper describes a method to design vertical dispersion bumps in a fourth generation light source. The purpose of these dispersion bumps is the adjustment of the vertical emittance to a desired level, while preserving source properties for insertion devices. This approach is relevant in ultralow-emittance lattices, where a vertical emittance lower than required leads to unnecessary Touschek lifetime reduction and emittance blowup from IBS. I have developed the algorithm for the design of the dispersion bumps under given boundary conditions and I have studied the performance of the MAX IV 3 GeV storage ring lattice when employing these dispersion bumps in numerical simulations. I wrote most of the manuscript.

II **Equilibrium bunch density distribution with passive harmonic cavities in a storage ring**
Subject of this paper is the operation mode of passive harmonic cavities in the MAX IV 3 GeV storage ring, an essential ingredient to reach the targeted beam lifetime and emittance. These passive harmonic cavities are operated in a parameter range in which the amplitude, but also the phase of waves excited in these cavities depend on the electron bunch shape. I have contributed to the measurements in the MAX III storage ring, where I have prepared and carried out the bunch shape measurements. I wrote parts of the manuscript that relate to these measurements.

III **Methods for measuring sub-pm rad vertical emittance at the Swiss Light Source**
This paper introduces a refined concept of vertical beam size measurements with visible to ultraviolet synchrotron radiation from bending magnets, employing a diffraction obstacle. At a diagnostic beamline at the Swiss Light Source effects of the diffraction obstacle on the beam image have been studied experimentally. During several visits I have participated in preparations and modifications of this diagnostic beamline. I have contributed to the measurements, developed numerical models of the beamline, evaluated the measurement data and developed ways to quantify and compare measurement accuracy. I wrote most of the manuscript.

IV **Emittance diagnostics at the MAX IV 3 GeV storage ring**
In this paper the diagnostic beamline concept for ultralow-emittance measurements with synchrotron radiation from bending magnets in the MAX IV 3 GeV storage ring is introduced. While the vertical beam size is measured with the obstacle diffractometer method in the near-ultraviolet spectral range, the horizontal beam size is inferred from a fringe pattern formed by infrared SR at wide horizontal acceptance angles. I have participated in the design of the MAX IV diagnostic beamlines, their installation and the commissioning of the first beamline. I have performed the numerical calculations and I participated in the measurements presented in this paper. I wrote the manuscript and presented this work at the conference.

Papers

Paper I

Improving Touschek lifetime in ultralow-emittance lattices through systematic application of successive closed vertical dispersion bumps

J. Breunlin, S. C. Leemann, and Å. Andersson.

Physical Review Accelerators and Beams **19**, 060701 (2016).

PHYSICAL REVIEW ACCELERATORS AND BEAMS **19,** 060701 (2016)

Improving Touschek lifetime in ultralow-emittance lattices through systematic application of successive closed vertical dispersion bumps

J. Breunlin,* S. C. Leemann, and Å. Andersson
MAX IV Laboratory, Lund University, SE-22100 Lund, Sweden
(Received 4 December 2015; published 9 June 2016)

In present ultralow-emittance storage ring designs the emittance coupling required for the production of vertically diffraction-limited synchrotron radiation in the hard x-ray regime is achieved and in many cases surpassed by a correction of the orbit and the linear optics alone. However, operating with a vertical emittance lower than required is disadvantageous, since it decreases Touschek lifetime and reduces brightness due to the transverse emittance increase from intrabeam scattering. In this paper we present a scheme consisting of closed vertical dispersion bumps successively excited in each arc of the storage ring by skew quadrupoles that couple horizontal dispersion into the vertical plane to a desired level and thereby raise the vertical emittance in a controlled fashion. A systematic approach to vertical dispersion bumps has been developed that suppresses dispersion and betatron coupling in the straight sections in order to maintain a small projected emittance for insertion devices. In this way, beam lifetime can be significantly increased without negatively impacting insertion device source properties and hence brightness. Using simulation results for the MAX IV 3 GeV storage ring including magnet and alignment imperfections we demonstrate that Touschek lifetime can be increased by more than a factor 2 by adjusting the vertical emittance from 1.3 pm rad (after orbit correction) to 8 pm rad (after application of dispersion bumps) using two to three independent skew quadrupole families all the while ensuring deviations from design optics are restrained to a minimum.

DOI: 10.1103/PhysRevAccelBeams.19.060701

I. INTRODUCTION

Today's ultralow-emittance (ULE) storage rings are based on multibend achromat (MBA) lattices. In such storage rings the emittance coupling required to operate at the diffraction limit in the vertical plane is comparably high. With orbit corrections and linear optics corrections applied the vertical emittance resulting from imperfections (magnet and alignment errors) can, however, become extremely low, lower in fact than required to be diffraction-limited at the wavelengths of interest. This is a highly undesirable situation because of the resulting Touschek lifetime penalty [1–3] as well as brightness limitations caused by the increased emittance blowup from intrabeam scattering (IBS) [4].

We propose therefore to drive successive closed vertical dispersion bumps (SCVDBs) in the MBA arcs around the storage ring. Ideally, the vertical emittance is then created directly via quantum excitation in the bending magnets. Closing the vertical dispersion bump at the end of the arc ensures that the straights remain dispersion free. In this way, and by ensuring low betatron coupling in the straights, the electron beam in the insertion devices (IDs) provides small source properties in order to produce diffraction-limited synchrotron radiation (SR) and maintain high levels of transverse coherence [5]. The Touschek lifetime is, however, substantially improved by the increase in vertical emittance since it can be shown to scale like $\tau \propto \sqrt{\mathcal{E}_{\mathrm{II}}}$ (see Sec. II A).

As will be shown in this paper, a SCVDB lattice with properly closed vertical dispersion bumps but otherwise only minor deviations from the design lattice can be found. In such a lattice the dynamic aperture (DA) remains high and there is only negligible betatron coupling in the IDs where the vertical acceptance limitations are located. Therefore, lifetime can be considerably improved while injection efficiency remains excellent.

Vertical dispersion bumps have been proposed before. In one set of applications a local closed bump is required to achieve a transverse separation within an energy-modulated beam [6]; contrary to what is proposed in this paper such a bump is created explicitly within the ID. In other applications vertical dispersion waves for lifetime improvement have been proposed [7,8], however, in such cases the vertical dispersion follows a wave extending throughout both straights and arcs. It therefore improves the Touschek lifetime, but it also removes achromaticity and alters the source properties in the IDs. In ULE storage rings this is no longer an acceptable perturbation.

In contrast to such attempts, the method proposed here takes a more fundamental approach where achromaticity

*jonas.breunlin@maxiv.lu.se

and beam properties in the IDs are introduced as fixed boundary constraints. The vertical dispersion is then tailored in specific locations away from the IDs to exactly match lifetime requirements while respecting all boundary constraints. This systematic approach of successive closed vertical dispersion bumps and three examples of applications to the MAX IV 3 GeV storage ring along with estimates of the achievable performance, based on results from 6D tracking with Tracy-3 [9], will be presented in this paper.

II. BACKGROUND AND PRINCIPLE

A. Touschek lifetime and vertical emittance

Touschek scattering is the dominant beam loss mechanism in present storage ring light sources. The effect of vertical emittance on Touschek lifetime can be derived from [1–3]

$$\frac{1}{\tau} = \frac{r_e^2 c q}{8\pi e \gamma^3 \sigma_s C} \cdot \oint_C \frac{F\left(\left[\frac{\delta_{\mathrm{acc}}(s)}{\gamma \sigma_{x'}(s)}\right]^2\right)}{\sigma_x(s)\sigma_y(s)\sigma_{x'}(s)\delta_{\mathrm{acc}}^2(s)} ds, \quad (1)$$

where r_e denotes the classical electron radius, c the vacuum velocity of light, e the elementary charge, C the circumference of the storage ring, q the bunch charge and γ the Lorentz factor of the beam. The horizontal and vertical rms beam sizes are σ_x and σ_y, respectively, while σ_s denotes the rms bunch length, $\delta_{\mathrm{acc}}(s)$ the local momentum acceptance and $\sigma_{x'}(s)$ the horizontal rms beam divergence for an electron at $x \approx 0$, where Touschek scattering events are expected to occur. Finally, the function $F(x)$ is defined as

$$F(x) = \int_0^1 \left[\frac{1}{u} - \frac{1}{2}\ln\left(\frac{1}{u}\right) - 1\right] \exp\left(-\frac{x}{u}\right) du. \quad (2)$$

Under the assumption that both vertical dispersion and betatron coupling are negligible contributions to the vertical beam size ($\sigma_y(s) \approx \sqrt{\mathcal{E}_{\mathrm{II}}\beta_{\mathrm{II}}(s)}$) the Touschek lifetime then scales like

$$\tau \propto \sqrt{\mathcal{E}_{\mathrm{II}}}. \quad (3)$$

Hence a substantial improvement of the Touschek lifetime can be achieved by increasing the vertical emittance.

B. ULE lattices and vertical dispersion

A typical example for an ULE storage ring lattice is the design lattice of the MAX IV 3 GeV storage ring [10]. It shows a low horizontal dispersion in the arcs while the long straights are dispersion-free (achromatic lattice), see Fig. 1. Since the vertical dispersion is zero by design (flat lattice), the only sources of vertical emittance in the real storage ring, apart from quantum excitation from SR emission (amounting to less than 0.1 pm rad), are betatron coupling and spurious vertical dispersion, resulting from imperfections such as magnet and alignment errors.

It is common practice to minimize both vertical dispersion and betatron coupling in order to improve the DA[1] and to reduce beam losses on narrow vertical acceptances (usually found in the long straights as a consequence of narrow-gap chambers and in-vacuum IDs). This can be achieved following the widely used LOCO [14] approach: The betatron coupling is determined from off-diagonal elements in the orbit response matrix whereas vertical orbits from rf frequency shifts yield the vertical dispersion response matrix. Betatron coupling and vertical dispersion are then minimized by inversion of sensitivity matrices from a calibrated machine model, which describes the influence of correcting skew quadrupoles on the orbit and dispersion response matrix, for an example see [15]. However, the resulting low emittance coupling might reduce the Touschek lifetime to unacceptable values. Negative consequences of a short beam lifetime are an increased top-up rate and possibly radiation issues. Furthermore, a low emittance coupling further increases IBS blowup which is already severe in ULE lattices, when storing high current at medium energy [4].

To alleviate this problem the vertical emittance might be created from vertical dispersion in the arcs only up to the maximum permissible level (diffraction limit). In the presence of vertical dispersion the natural emittance for the vertical plane yields [16,17]:

$$\mathcal{E}_{\mathrm{II}} \approx C_q \gamma^2 \frac{I_{5,\mathrm{II}}}{I_2} \quad \text{with} \quad I_{5,\mathrm{II}} = \oint \frac{\mathcal{H}_{\mathrm{II}}}{|\rho|^3} ds, \quad (4)$$

where the constant is $C_q \approx 3.823 \times 10^{-13}$ m, I_2 and $I_{5,\mathrm{II}}$ are the second and fifth (vertical) synchrotron radiation integrals and the bending radius is ρ ($\rho = \rho_x$ in a flat machine). The chromatic invariant in the vertical plane is defined as

$$\mathcal{H}_{\mathrm{II}}(s) = \gamma_{\mathrm{II}}\eta_{\mathrm{II}}^2 + 2\alpha_{\mathrm{II}}\eta_{\mathrm{II}}\eta'_{\mathrm{II}} + \beta_{\mathrm{II}}\eta'^2_{\mathrm{II}}. \quad (5)$$

By excitation of skew quadrupole magnets horizontal dispersion can be coupled into the vertical plane, which, together with the excited betatron coupling [18,19] increases the vertical emittance [20].

With a suitable set of skew quadrupoles a local vertical dispersion bump with locally increased betatron coupling can be created. Once a dispersion bump has been designed for one achromat, the principle is leveraged by systematically applying it to each achromat, resulting in SCVDBs around the entire ring. Opening and closing each dispersion bump within the same arc ensures that the straight sections remain dispersion-free. If in addition to closing the vertical

[1]Maintaining sufficient DA is a crucial requirement considering off-axis injection e.g. [11], which is being employed in several new ULE rings [10,12,13].

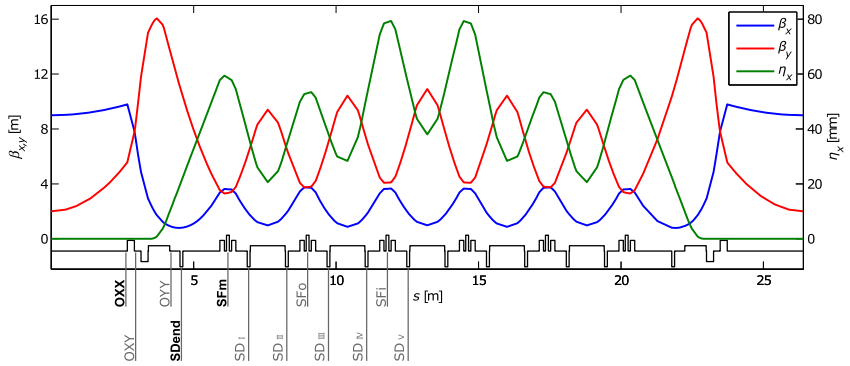

FIG. 1. Design optics of the MAX IV 3 GeV storage ring in one achromat. The design vertical dispersion is zero everywhere. The positions of the magnets are indicated at the bottom in black. The positions and names of sextupole and octupole magnets, equipped with auxiliary coils to generate skew quadrupole gradients, are indicated below. The sequence of magnets repeats mirror-symmetrically throughout the second half of the achromat.

dispersion bumps the betatron coupling is restricted to the arcs the increase in beam size is also mainly restricted to locations in the arcs. The source properties of IDs in the long straights[2] on the other hand are not altered, apart from the increase in vertical emittance, which is, however, adjusted below the diffraction limit.

In the simplest case and if no assumptions on the phase advance between skew quadrupoles are made, a closed vertical dispersion bump can be created with three skew quadrupoles. However, the dispersion function in the horizontal plane and beta functions present additional constraints. Since every deviation from the design lattice presents a potential source of undesired effects such as betatron coupling in the long straights or nonlinear optics detuning, the implementation of the vertical dispersion bumps must be done under consideration of those lattice functions. A certain flexibility in the choice of skew quadrupoles is helpful. It is therefore of great advantage that a large number of potential skew quadrupoles along the arcs have been built into the MAX IV 3 GeV storage ring from the start (Fig. 1). The task remaining is to identify those skew quadrupoles and their gradients that create the vertical dispersion as desired in an efficient way and with a minimum deviation from the design optics.

C. Vertical dispersion bump design using a SVD-based algorithm

Closed expressions for the electron optics, such as beta functions and dispersion, as a function of the gradients of a set of skew quadrupoles can in principle be derived within the framework of linear approximation (e.g. [21]). Finding suitable dispersion distributions as analytical solutions of such a system of equations, however, becomes impractical for large numbers of skew quadrupole magnets. Instead, our systematic approach to SCVDBs is based on the recording of the lattice response to skew quadrupole magnet excitations, in order to generate a sensitivity matrix. Inverting this matrix a skew quadrupole setting can then be found that generates a dispersion bump with the desired properties. The required optics calculations are carried out with e.g. Tracy-3 and are applied to the design magnetic lattice of the storage ring.

The implementation of the dispersion bump as well as undesired deviations from the design lattice can be characterized by a set of key parameters e.g. the vertical dispersion in the bending magnets (where vertical emittance is created) as well as the beta functions and dispersion in SR source points or in regions of narrow apertures. The response of the lattice, given by all key parameters $\vec{p} = p_1 \ldots p_n$, is then recorded as a function of the gradients of a set of skew quadrupoles $\vec{k} = k_1 \ldots k_m$. This skew quadrupole setting may include many potentially available skew quadrupoles, since the selection of the most efficient skew quadrupoles follows in a later step. Systematic variations in skew quadrupole strengths $\vec{k}$ and recordings of the related responses $\vec{p}$ subsequently form the matrices $\mathcal{P}_{j,n}$ and $\mathcal{K}_{j,m}$, where j denotes the index of the generated set of skew quadrupole setting and lattice response.

With the pseudoinverse of the $\mathcal{P}_{j,n}$ matrix, calculated via SVD (singular value decomposition) [22], the sensitivity matrix $\mathcal{M}$ is calculated as

$$\mathcal{M}_{n,m} = \mathcal{P}^{-1}_{n,j} \cdot \mathcal{K}_{j,m}, \tag{6}$$

with which the skew quadrupole strengths $\vec{k}_t$, required to approach a defined target $\vec{p}_t$ in the key parameter space, can be determined as follows:

[2]The MAX IV 3 GeV storage ring design does not include bending magnet SR source points.

$$\vec{k}_t = \vec{p}_t \cdot \mathcal{M}. \quad (7)$$

This target $\vec{p}_t$, expressible in terms of the key parameters, may represent the design lattice including the desired dispersion bump, or may be a more relaxed but still tolerable deviation from it. Once the lattice is adjusted for the setting $\vec{k}_t$ and the lattice response is recorded, the success in approaching the target parameters is evaluated. In an iterative process the parameter space, given by the combinations and gradients of the available skew quadrupoles, is searched for suitable dispersion bump implementations.

In addition to the direct evaluation of the implemented dispersion bumps, the analysis of the sensitivity matrix itself provides valuable information. Due to lattice symmetry several groups of potential skew quadrupoles might be located where the ratios of the betatron functions and the horizontal dispersion are similar, and are therefore expected to have similar effects on the optics. Such a linear dependence presents an inefficient use of skew quadrupoles and should be avoided. For testing this the sensitivity matrix is written in its factorized form as follows (SVD):

$$\mathcal{M} = U\Sigma V^T \quad (8)$$

Here U and V are orthogonal matrices and Σ is a $n \times m$ matrix with the singular values of $\mathcal{M}$ along its diagonal. Any inefficiently implemented dispersion bump can then be identified by a smaller number of nonvanishing singular values (the rank of the sensitivity matrix $\mathcal{M}$) compared to the number of employed skew quadrupoles. Furthermore, the sensitivity of each of the individual skew quadrupoles to the key parameters can be studied. This offers a systematic way to evaluate, compare, and improve dispersion bump implementations and their effect on the optics.

In practice the target parameters can often not be simultaneously fulfilled, but only approached. This can be caused by a dependency of the skew quadrupoles or just because the number of available skew quadrupole families is lower than the number of target parameters ($m < n$), which leads to an underdetermined system of equations. Under these conditions trade-offs between the boundary conditions become necessary and can be investigated by variations of the target parameters within tolerable limits. An example for this is discussed in Sec. III A.

Applying this systematic approach allows finding a set of suitable skew quadrupoles and their individual excitation required to increase the Touschek lifetime efficiently by an increase in vertical emittance, while respecting the defined boundary conditions. An added benefit of this approach compared to a derivation from closed expressions is generality since no solutions have to be *a priori* excluded. Furthermore, the method allows quantifying the cost in terms of deviation from the design optics, possibly connected to an increase in beam size in IDs, and the achieved lifetime gain as a function of effort. Verification of the implemented SCVDBs can be performed by measuring a vertical dispersion response matrix and applying a LOCO fit to the lattice. With a suitable emittance monitor, as it is in preparation for the MAX IV 3 GeV storage ring [23], the vertical emittance can be measured in a nondestructive way. This allows the controlled implementation and verification of SCVDBs even during user shifts.

III. CASES AND RESULTS

We use the MAX IV 3 GeV storage ring to showcase our approach. Throughout the design phase of this storage ring it has been assumed that the vertical emittance would be adjusted to desired values. In the Detailed Design Report [23] the vertical emittance was specified to be 8 pm rad, aiming for diffraction limited operation with 1 Å SR. Later optimizations, aiming for maximum brightness and transverse coherence, called for 2 pm rad vertical emittance [5].

Examples for how SCVDBs can be implemented in a real machine in order to meet such emittance requirements will now for the first time be demonstrated in detail. We present three design cases of SCVDB lattices to demonstrate how, with varying effort, the boundary constraints and target parameters can be enforced to required levels. Apart from the varying effort, represented by the number of individually powered skew quadrupole families (number of magnet power supplies), the cases are designed under slightly different trade-offs of the boundary constraints, to achieve the goal of a scalable Touschek lifetime increase with the least effect on the design optics.

A. Boundary constraints and target parameters

The MAX IV 3 GeV storage ring provides 12 potential skew quadrupole families. This high number is achieved by auxiliary coils available on all sextupole and octupole magnets that can be powered (among others) as skew quadrupoles. Each of these magnets has an effective length of 0.10 m and a maximum normalized skew quadrupole gradient of 0.10 m^{-2} to 0.26 m^{-2}, depending on the exact magnet type. The positions of all available auxiliary coils on sextupole and octupole magnets in the lattice are indicated in Fig. 1 for one half of the achromat. In accordance with the lattice symmetry the skew quadrupoles on mirror-symmetric positions within the achromat are paired and kept at identical gradients for the cases presented in this study. The presented cases presume that these skew quadrupole pairs are powered in each of the 20 achromats to generate identical vertical dispersion bumps around the entire storage ring. Therefore, one independent family of skew quadrupoles consists of 40 equally powered skew quadrupoles, and the lattice symmetry is unbroken (excluding machine imperfections).

Four of the five target parameters are set in order to minimize deviations from the design optics: Two

parameters, $\beta_x = 9.0$ m and $\beta_y = 2.0$ m in the center of the long straight, prevent excessive growth of the beta functions compared to the design optics. The main purpose of this target is to avoid an increase in beam size in the ID. Stipulating this target also prevents large betatron coupling in the long straights as an indirect effect. In the ideal design lattice the horizontal and vertical dispersion η_x and η_y are zero in the long straights to ensure a sufficiently small source size in the IDs. In order to maintain this achromaticity, two additional targets are stipulated: $|\eta_x| < 6$ mm and $|\eta_y| < 0.5$ mm in the long straights. This ensures that dispersive contributions to the beam size remain negligible in the IDs for the assumed energy spread of $\sigma_\delta = 0.8 \times 10^{-3}$. Since there are no bending magnet SR sources in the MAX IV 3 GeV storage ring no constraints are made to maintain source properties in the arcs. In principle this could however be done in the same manner as in the long straights. The fifth target parameter is related to the amplitude of the vertical dispersion bump. For this purpose one key parameter is introduced that depends on the vertical dispersion in the bending magnets, since this is where vertical emittance is generated. The exact amplitude of the vertical dispersion bump is, however, not controlled by a target parameter. This problem is addressed in Sec. III C. Solutions where the vertical dispersion bump is opened as far upstream as possible in the arc (and closed as far downstream as possible) are preferred since they allow for lower vertical dispersion (more bends are involved in increasing the vertical emittance). In the cases presented here, this is achieved by using skew quadrupoles close to the long straights, rather than those around the center of the arc.

B. Motivation of cases

In the following a brief motivation for the design of the three presented cases is given. A detailed and comparative investigation can be found in the following sections. The vertical dispersion created in one achromat is shown in Fig. 2 for the three SCVDB cases. The vertical emittance created by these three cases in the ideal lattice (i.e. without imperfections) is 6.6 pm rad.

Case 1 demonstrates that a considerable gain in Touschek lifetime can be achieved using just a single skew quadrupole family. In this case the vertical dispersion bump

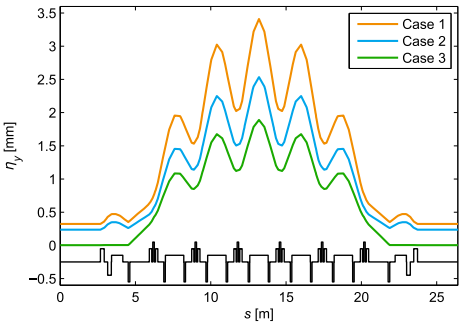

FIG. 2. Ideal vertical dispersion in Cases 1 to 3. Approximately 6.6 pm rad of vertical emittance is created in the ideal lattice which gives on average 7.9 pm rad when including imperfections.

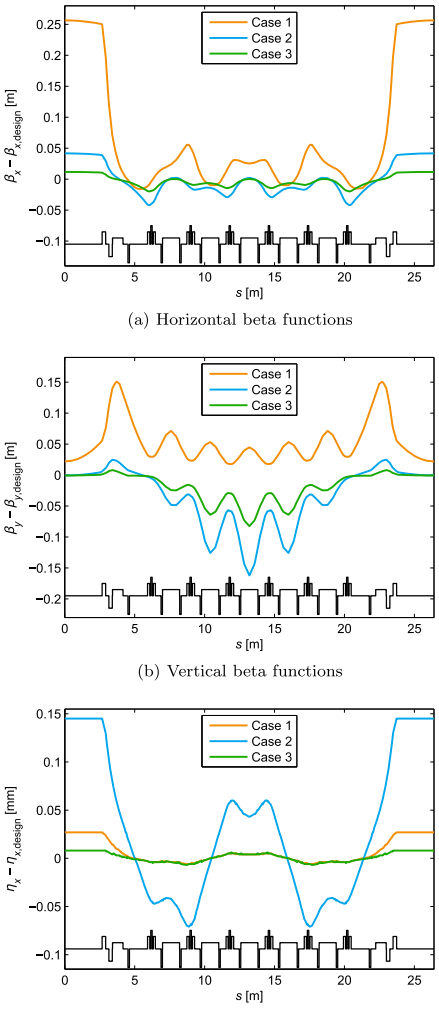

(a) Horizontal beta functions

(b) Vertical beta functions

(c) Horizontal dispersion functions

FIG. 3. Difference between the design optics functions and the optics functions from SCVDB lattices. For all cases, the vertical emittance is 6.6 pm rad in the ideal lattice and on average 7.9 pm rad when including imperfections.

is not closed but only suppressed in the long straights (Fig. 2). This case also shows considerable growth in the horizontal beta function compared to the design optics (Fig. 3(a)). The design of Case 2 makes use of two skew quadrupole families and is focused on minimizing the betatron coupling in the long straights, here an undesired side-effect of skew quadrupole excitation. Although the horizontal dispersion in the long straight appears comparably large [Fig. 3(c)], this example still shows advantages compared to Case 1. Case 3 shows a similar design as Case 2 but involves three skew quadrupole families, where the added family allows an efficient correction of the deficiencies of the previous cases. With the additional degree of freedom the defined target parameters can be approached more closely. However, further enforcing the target parameters does not appear to be of much practical benefit since the remaining discrepancies approach the level of deviations between ideal lattice and real lattice (i.e. lattices including imperfections, see Sec. III F).

C. Scaling of SCVDBs

The method introduced in Sec. II C provides SCVDB designs that can be easily scaled in vertical dispersion, generated vertical emittance and hence, Touschek lifetime as required. By adjusting the gradients proportionally in all skew quadrupoles, only the amplitude but not the general shape of the vertical dispersion bumps is changed [21], see Fig. 4. For adjusting the vertical emittance in practice the approximation $\mathcal{E}_{\mathrm{II}} \propto k^2$ [20] offers a simple way to scale without requiring a redesign via the sensitivity matrix approach. Since not only the vertical dispersion but also the deviations from the design optics scale with the skew quadrupole gradient it is useful to design SCVDBs with sufficient amplitude, followed by a down-scaling to the exact required vertical emittance. This ensures that the defined boundary constraints are not violated due to the scaling.

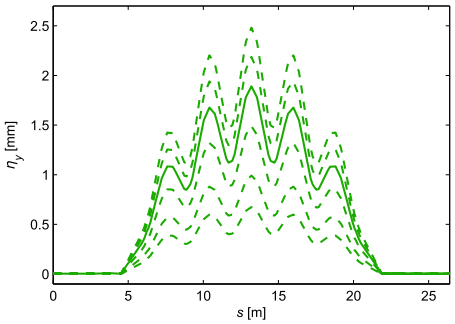

FIG. 4. SCVDB scaling in the ideal lattice of Case 3. Indicated with a solid line is the vertical dispersion that creates 6.6 pm rad of vertical emittance in the ideal lattice and on average 7.8 pm rad when including imperfections. The dashed lines show the vertical dispersions of scaled SCVDBs that create $\mathcal{E}_{\mathrm{II}} = 0.9$, 1.8, 4.1, 8.9 and 11.4 pm rad in the ideal lattice, respectively.

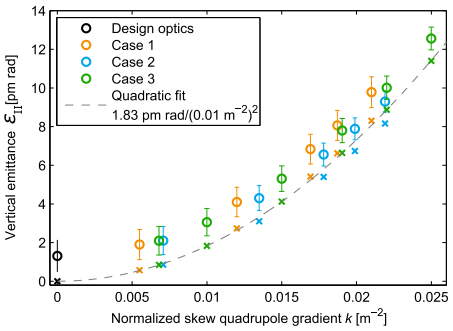

FIG. 5. Vertical emittance scales with skew quadrupole gradient squared. Ideal lattice (x) and error lattice (o) with standard deviations from 10 error seeds. Only the k of the strongest skew quadrupole involved in each case is considered.

Scaling is demonstrated in Fig. 5, where the vertical emittance generated in Case 1, 2, and 3 in the ideal lattice is shown as a function of the required normalized skew quadrupole gradient k. Since Cases 2 and 3 are based on more than one skew quadrupole family (see Table I for details), the strongest skew quadrupole is considered here. The quadratic fit for Case 3 gives 1.83 pm rad vertical emittance per $(0.01\ \mathrm{m}^{-2})^2$ skew quadrupole gradient.

D. Skew quadrupole gradients

Skew quadrupole gradients are constrained by the available gradients in the real machine (magnet coils, power supplies), but also by the design goal of minimum perturbations of the design optics, especially avoiding nonlinear effects. Therefore, one design criterion is minimizing required skew quadrupole gradient while enforcing target parameters to sufficient degree. In all presented cases the normalized skew quadrupole gradient required to achieve 8 pm rad vertical emittance (including lattice

TABLE I. Normalized skew quadrupole gradient k in m^{-2}, generated by auxiliary coils on the magnets used for the presented SCVDBs. The effective length of each magnet is 0.1 m. The vertical emittance $\mathcal{E}_{\mathrm{II}}$ given here is created in the ideal lattice (i.e. without magnet errors or misalignments).

	OXX	SDend	SFm	$\mathcal{E}_{\mathrm{II}}$ [pm rad]
Case 1	0	0.0187	0	6.62
Case 2	0.0198	0.0138	0	6.74
Case 3	0.0193	0.0114	−0.0017	6.64

imperfections) is less than 0.02 m^{-2} i.e. less than 20% of the maximum available gradient in these types of magnets. In comparison, the expected skew quadrupole gradient required to compensate for coupling effects from EPUs is approximately 0.03 m^{-2} [24].

E. Impact on design optics and corrections

Deviations of the beta functions from design values induce small changes in the phase advance over the achromats and, thus, shift the machine working point.

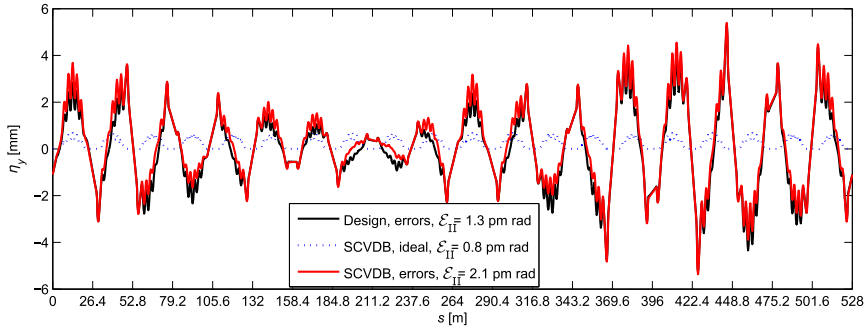

(a) Resulting vertical emittance, $\mathcal{E}_{II} = 2$ pm rad scaling.

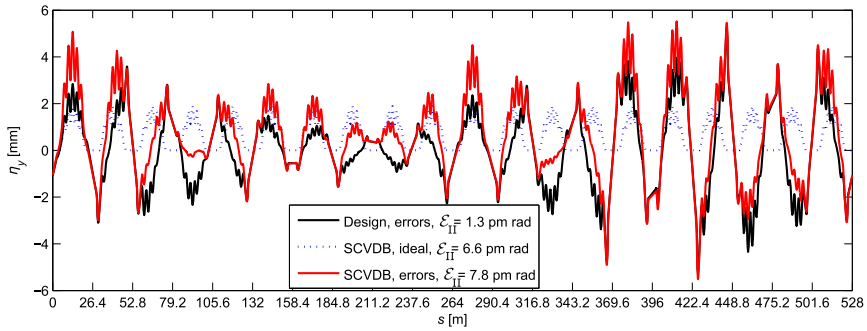

(b) Resulting vertical emittance, $\mathcal{E}_{II} = 8$ pm rad scaling.

FIG. 6. Vertical dispersion in the entire storage ring (20 achromats) for the design lattice and Case 3 lattice with identical error seed for two scalings. The ideal lattice SCVDB is shown for comparison.

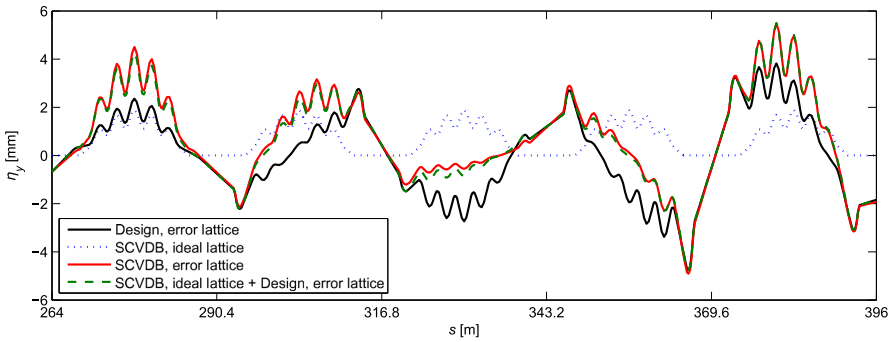

FIG. 7. Detail of vertical dispersion Case 3 in five achromats. Adding the vertical dispersion from the two independent sources, lattice imperfections and SCVDBs, linearly leads to a good estimate of the vertical dispersion under the influence of lattice errors.

TABLE II. Impact of SCVDBs on beam sizes, vertical projected emittance in IDs (center of long straights), eigenemittances and on the emittance ratio $\kappa = \mathcal{E}_{\mathrm{II}}/\mathcal{E}_{\mathrm{I}}$. All results are averaged over 20 straight sections and 10 error seeds. The standard deviation is also displayed.

	σ_x [μm]	σ_y [μm]	ϵ_y [pm rad]	$\mathcal{E}_{\mathrm{I}}$ [pm rad]	$\mathcal{E}_{\mathrm{II}}$ [pm rad]	κ [%]
Design	54.35 ± 0.37	1.89 ± 0.14	1.95 ± 1.27	328.3 ± 0.4	1.31 ± 0.82	0.40
Case 1	55.29 ± 0.43	4.66 ± 0.30	12.35 ± 1.05	330.2 ± 0.4	8.06 ± 0.78	2.44
Case 2	54.42 ± 0.44	4.13 ± 0.09	8.96 ± 0.88	327.4 ± 0.3	7.88 ± 0.57	2.41
Case 3	54.35 ± 0.40	4.09 ± 0.08	8.53 ± 0.97	327.8 ± 0.3	7.80 ± 0.63	2.38

This is easily corrected by a slight global tuning of the main quadrupoles in the storage ring. The required changes in quadrupole gradient are less than 0.1%. This adjustment of the quadrupole gradients can shift the linear chromaticity in both planes requiring a correction with at least two chromatic sextupole families. A change in sextupole gradient of less than 2% restores the linear chromaticities to the design values $\xi_{x,y} = +1.0$. These corrections are performed on the ideal lattice, before adding lattice imperfections to the simulation. Examples for deviations of higher order optics from design and their effect on the machine performance and beam lifetime are discussed in Sec. III I.

F. Effect of lattice imperfections on SCVDBs

Studies on error lattices are performed in order to estimate the performance of SCVDBs under realistic conditions. As in previous studies on the MAX IV 3 GeV storage ring [23,25], the generated error lattices include the effects of misalignments of magnets, magnetic field errors and multipole errors. For each error seed orbit correction is applied, however, no minimization of betatron coupling or spurious vertical dispersion is attempted at this point, since the vertical emittance of the error lattices is ≈1.3 pm rad and beam tilts from betatron coupling in the long straights are sufficiently small for user operation. The same 10 error seeds are applied to both the design lattice and to the three SCVDB cases. The increase in average vertical emittance due to errors varies between 1.1 pm rad and 1.4 pm rad, depending on the individual SCVDB case and scaling.

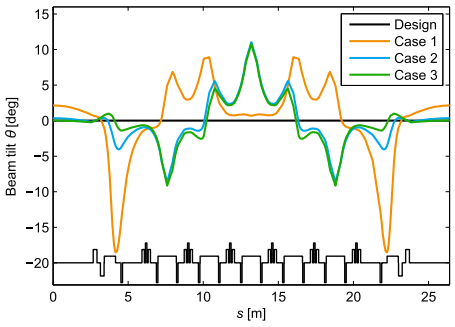

FIG. 8. Beam tilt angle Θ in the ideal lattice.

The effect of errors on the Case 3 vertical dispersion function is shown in Fig. 6(a) and (b) for one error seed as an example. Note that orbit correction is applied but spurious vertical dispersion and betatron coupling are not minimized. For a desired vertical emittance of 2 pm rad the necessary emittance increase by the SCVDB amounts to only half of the vertical emittance generated by errors. Therefore, the ideal vertical dispersion from the SCVDB is small compared to the vertical dispersion caused by errors in the design lattice [see Fig. 6(a)]. As expected, the vertical dispersion of the SCVDB lattices with errors does not deviate much from the vertical dispersion of the design lattice. For 8 pm rad desired vertical emittance the SCVDBs are the dominant source of vertical emittance, since they create approximately 6.6 pm rad. Figure 6(b) illustrates the working principle of the SCVDB lattice as a shift of the design vertical dispersion caused by random errors toward positive values. A relatively small increase in vertical dispersion is sufficient to achieve the targeted vertical emittance.

It is an interesting observation that the vertical dispersion of the SCVDB lattice without imperfections added linearly to the vertical dispersion in the design lattice generated randomly by imperfections, provides a good approximation[3] of the total vertical dispersion of the SCVDB lattices including errors. This behavior is shown in Fig. 7.

G. Beam sizes, beam tilt and projected emittance

Apart from the expected growth of the vertical beam size, following the approximate relation $\sigma_y \propto \sqrt{\mathcal{E}_{\mathrm{II}}}$, only Case 1 shows an increased vertical beam size in the center of the long straight (Table II). The Case 1 lattice shows the largest deviations from design in terms of beta function [see Fig. 3(a) and (b)]. Furthermore, the betatron coupling created in the arc is not closed and a comparably large systematic beam tilt angle [18] is introduced in the long straight (see Fig. 8). In all cases the beam sizes are dominated by the betatronic contribution while the dispersive contributions can be neglected. This is in

[3]The error lattice contains among others rolled sextupoles as well as misaligned and rolled octupoles as nonlinear sources of dispersion, leading to deviations from a strictly linear behavior.

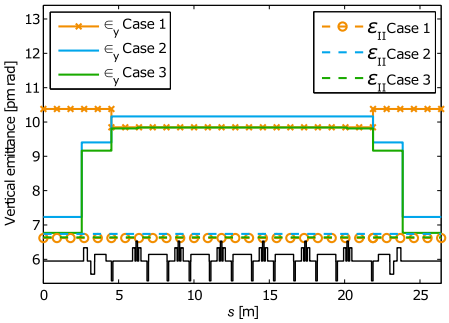

FIG. 9. Vertical projected emittance ϵ_y (solid lines) and vertical eigenemittance $\mathcal{E}_{\mathrm{II}}$ (dashed lines) in the ideal lattice for the three cases. (Markers are displayed for Case 1 since traces partially overlap.)

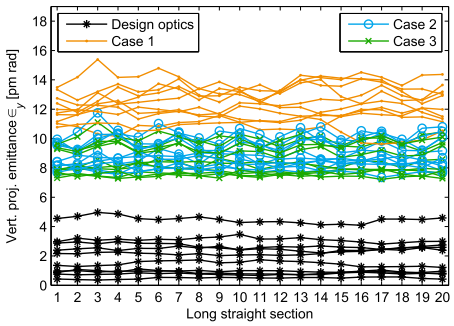

FIG. 10. Vertical projected emittance ϵ_y in the long straight sections (ID locations) including lattice imperfections (10 error seeds) for the design optics and the three SCVDB cases.

accordance with the original design paradigm where maximum tolerable $\eta_{x,y}$ contributions were specified for the long straights (see Sec. III A).

Both electron beam size and divergence define the phase space surface occupied by the beam in the laboratory frame and form the projected emittance ϵ [19,26,27] as a relevant source parameter in terms of matching electron beam optics to the intrinsic radiation from IDs [5]. Unlike the constant eigenemittance $\mathcal{E}$, the projected emittance ϵ varies along the storage ring and is equal to the eigenemittance only in the absence of coupling. Both emittances in the vertical plane, ϵ_y and $\mathcal{E}_{\mathrm{II}}$, are shown in Fig. 9 for the three cases and excluding lattice imperfections. Only in Case 2 and Case 3 does ϵ_y approach $\mathcal{E}_{\mathrm{II}}$ in the long straight sections, demonstrating the effective local betatron coupling suppression of these SCVDBs. Case 1 on the other hand shows an increase of vertical projected emittance in the long straight sections, amounting to $\epsilon_y = 10.4$ pm rad in the ideal lattice, and is therefore not compatible with the targeted diffraction limited operation with 1 Å SR.

A slight improvement of Case 1 is, however, possible without much extra effort by changing the polarity of the skew quadrupoles in every other achromat. The result is a zero crossing (instead of a constant deviation from zero, see Fig. 2) of the vertical dispersion and a reduction of the beam tilt angle in the long straights (Fig. 8). Nevertheless, since the vertical dispersion and betatron coupling are not properly closed, the vertical projected emittance remains substantially higher than the vertical eigenemittance ($\epsilon_y = 9.5$ pm rad, $\mathcal{E}_{\mathrm{II}} = 6.6$ pm rad).

When including the effects of lattice imperfections the vertical projected emittance of the design optics becomes 1.95 pm rad averaged over 20 long straight sections and 10 error seeds (Fig. 10). This is an increase of 0.64 pm rad compared to the vertical eigenemittance. In the SCVDBs Case 1, 2, and 3 the vertical projected emittance in the long straight sections exceeds the vertical eigenemittance by 4.29, 1.08, and 0.73 pm rad, respectively, as shown in Table II.

H. Touschek lifetime results from tracking

Touschek lifetime was calculated from local lattice momentum acceptance derived from tracking in 6D around the entire storage ring with Tracy-3. The Touschek lifetime calculated here, however, does not take into account bunch elongation from Landau cavities which increases the Touschek lifetime by roughly a factor five [4] independently of the vertical emittance adjustments detailed here. Lattice errors are included in the simulations and the vertical aperture is globally limited to ± 10 mm, corresponding to the vertical acceptance of the vacuum system without in-vacuum undulators or narrow-gap chambers. The tracking is performed over a full synchrotron period which in the MAX IV 3 GeV storage ring (without Landau cavities) is $\tau_s = 880$ μs (500 turns). Results are displayed in Table III.

Under the approximation $\tau \propto \sqrt{\mathcal{E}_{\mathrm{II}}}$ (see Sec. II A) the Touschek lifetime gain achieved with SCVDBs compared to the design lattice can be quantified with a *Figure Of Merit* (FOM) as follows:

$$\mathrm{FOM}_i = \frac{\tau_i}{\hat{\tau}_i} \cdot \sqrt{\frac{\hat{\mathcal{E}}_{\mathrm{II},i}}{\mathcal{E}_{\mathrm{II},i}}} \tag{9}$$

TABLE III. Tracking results for Touschek lifetime along with FOM for each case. Mean value and standard deviation are given for 10 error seeds.

	$\mathcal{E}_{\mathrm{II}}$ [pm rad]	τ[h]	FOM
Design	1.31 ± 0.82	5.06 ± 1.64	1
Case 1	8.06 ± 0.78	11.23 ± 0.36	0.854 ± 0.017
Case 2	7.88 ± 0.57	12.12 ± 0.58	0.931 ± 0.033
Case 3	7.80 ± 0.63	12.55 ± 0.51	0.969 ± 0.019

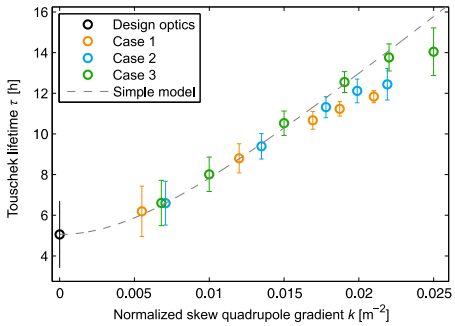

FIG. 11. Touschek lifetime as a function of skew quadrupole gradient. Tracking with errors, average and standard deviation for 10 seeds. Only the gradient of the strongest skew quadrupole used in each case is considered in this plot.

where $\hat{\tau}$ and $\hat{\mathcal{E}}_{\mathrm{II}}$ relate to the design lattice, τ and $\mathcal{E}_{\mathrm{II}}$ relate to the SCVDB lattice, and i is an identifier for the error seed. Thus, a resulting FOM < 1 indicates that the Touschek lifetime gain is lower than expected from the simple $\tau \propto \sqrt{\mathcal{E}_{\mathrm{II}}}$ relation. Possible reasons for this behavior are discussed in the following section. The FOM as an average over 10 error seeds is shown in Table III for the three SCVDB lattice designs. It is important to note that the FOM must be calculated for the individual error seed, as indicated in Eq. (9), in order to be a realistic measure of the performance of a SCVDB lattice under different conditions of lattice imperfections. Scaling averaged lifetimes with averaged vertical emittances will not lead to the same result.

A rough estimate of the general performance of the presented cases in terms of Touschek lifetime τ as a function of the normalized skew quadrupole gradient k, based on the relation $\tau \propto \sqrt{\mathcal{E}_{\mathrm{II}}}$, and including the effect of lattice imperfections is given by

$$\tau = a\sqrt{b \cdot k^2 + \langle \hat{\mathcal{E}}_{\mathrm{II}} \rangle}, \tag{10}$$

where $\langle \hat{\mathcal{E}}_{\mathrm{II}} \rangle = 1.31$ pm rad is the vertical emittance of the design lattice, including lattice imperfections and averaged over 10 error seeds. The fitted parameters are $a = 4.42$ hours Touschek lifetime per $\sqrt{\mathrm{pm\,rad}}$ of vertical emittance and b, the 1.83 pm rad vertical emittance per $(0.01\ \mathrm{m}^{-2})^2$ skew quadrupole gradient, mentioned in Sec. III C. The curve based on this simple model, representing a FOM $= 1$, is shown, together with the tracking results for Touschek lifetime, in Fig. 11.

I. Discrepancies in lifetime gain

Generally, the FOM is higher for lower skew quadrupole excitation and thus SCVDBs closer to the design lattice.

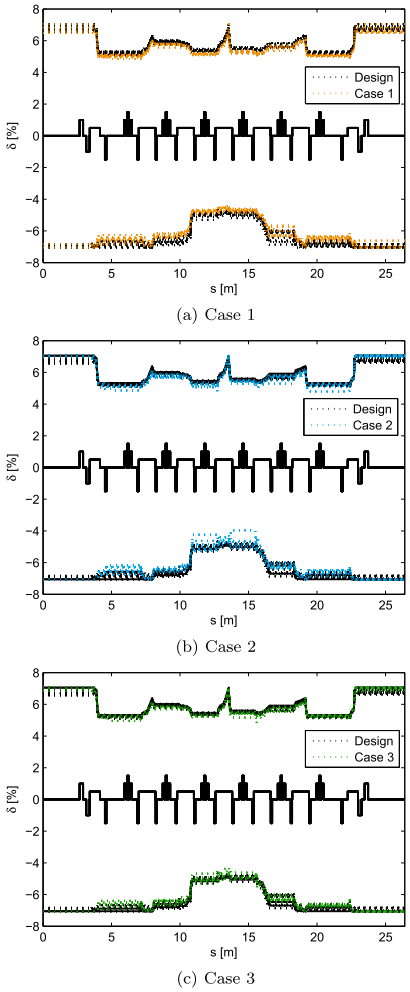

(a) Case 1

(b) Case 2

(c) Case 3

FIG. 12. Momentum aperture from 10 error seeds for the 3 cases, compared to design lattice (black) in the first achromat. The SCVDB lattices are scaled to approximately $\mathcal{E}_{\mathrm{II}} = 8$ pm rad while the design lattice with errors is on average at 1.3 pm rad.

This is illustrated in Fig. 11, where the deviation from the theoretical, ideal behavior becomes larger with increasing skew quadrupole gradient. Also, the differences between the SCVDB lattices become apparent, since designs that fulfill the target parameters to higher degree show less deviation from the theoretical assumption of FOM $= 1$.[4]

[4]Situations with FOM < 1 can occur if the dispersive contribution to the vertical beam size is not negligible. However, this is in contradiction to the initial assumptions.

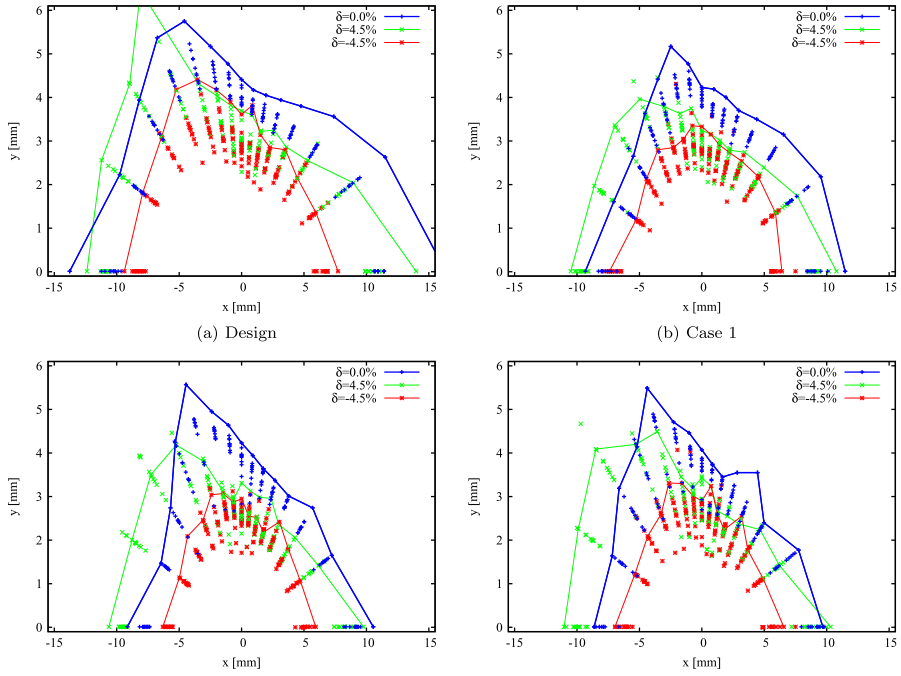

FIG. 13. Dynamic aperture for the ideal lattice and 10 error seeds. (a) shows the design lattice and (b)–(d) show the three SCVDB cases. The DA was calculated at the center of the first long straight section, close to the injection point.

To study the effects in detail that lead to beam loss and therefore reduced Touschek lifetime we investigated momentum aperture (MA), dynamic aperture, amplitude dependent tune shift (ADTS) and nonlinear chromaticity for all 10 error seeds. The tendency of a larger MA with increasing number of involved skew quadrupoles supports the design paradigm of minimizing deviations from design optics in order to maximize SCVDB performance. The MAs shown for the three cases and the design lattice can be found in Fig. 12. Although the differences are small, Case 3 shows the least restrictions in MA and is closest to the MA of the design lattice. This agrees with the fact that the FOM approaches 1 even at vertical emittances of 8 pm rad for this SCVDB design.

The DA was simulated in the center of the first long straight section ($s = 0$), not far from the injection point [11]. For the MAX IV 3 GeV ring injection scheme (on-energy, off-axis) the on-energy horizontal DA is the relevant parameter in terms of injection efficiency and ideally needs to be maintained at or beyond 7 mm. Figure 13 shows that with lattice errors included the DA stays within tolerable limits.

Generally, the small deviations from design in the linear optics, followed by a correction of betatron tunes and linear chromaticity keep the ADTS within acceptable limits in the three presented SCVDB cases. Performance limitations in terms of Touschek lifetime that originate in restricted local MA may, however, be explained by increased ADTSs. For example, Case 1 shows large negative horizontal tune shift with vertical amplitude [Fig. 14(b)] compared to the design optics and the Case 3 optics [Fig. 14(a) and (c)]. Also, for Case 3 only slight changes of the chromatic tune shifts compared to the design lattice can be recognized (see Fig. 15).

In principle the ADTS as well as the quadratic chromaticity can be corrected after the implementation of a dispersion bump, with expected positive effects on the beam lifetime and the injection efficiency. For such corrections the MAX IV 3 GeV storage ring is equipped with three families of octupole magnets (where corrections of ADTS and quadratic chromaticity are both first order effects) and five families of sextupole magnets in various locations. During the original lattice design the ADTS and quadratic chromaticity were optimized with these magnets

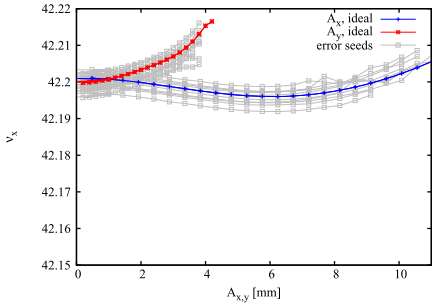

(a) Design

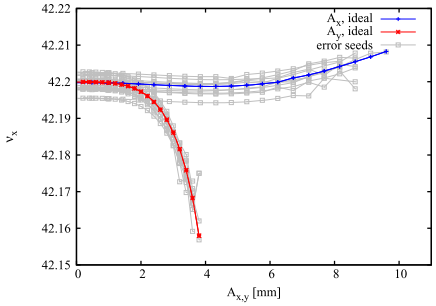

(b) Case 1

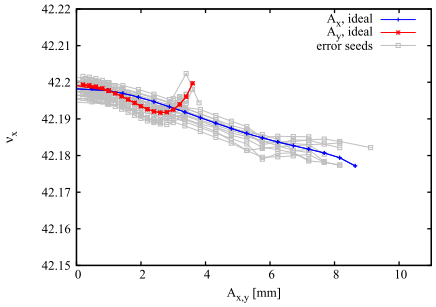

(c) Case 3

FIG. 14. Amplitude dependent tune shifts [horizontal tune (ν_x)] for the design lattice and Case 1 and 3 SCVDB lattices, adjusted for $\mathcal{E}_{\mathrm{II}} = 6.6$ pm rad without errors. Ideal lattice in blue (horizontal) and red (vertical). Ten error seeds in gray.

[10,28]. In this study, however, we focus on a SCVDB implementation with minimum impact on the design lattice. Corrections of ADTS and quadratic chromaticity with octupoles, combined with detailed frequency map analysis remain, therefore, as an option for further performance improvement, but are, as shown here, not inevitable for good SCVDB performance.

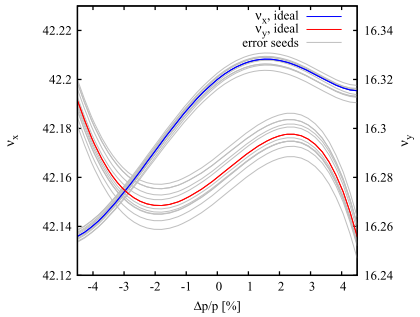

(a) Design

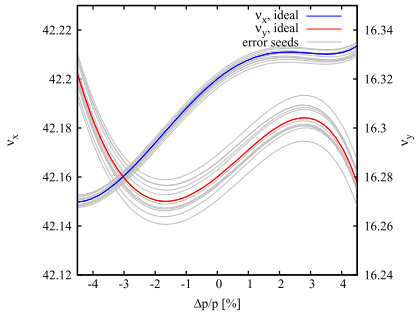

(b) Case 3

FIG. 15. Chromatic tune shifts for the design lattice and the Case 3 SCVDB lattice, adjusted for $\mathcal{E}_{\mathrm{II}} = 6.6$ pm rad without errors. Ideal lattice in blue (horizontal) and red (vertical). Ten error seeds in gray.

IV. SUMMARY

We have presented a systematic way of increasing the Touschek lifetime by employing successive closed vertical dispersion bumps that generate vertical emittance in a storage ring in a controlled fashion. By increasing the vertical emittance from 1.3 to 8 pm rad we can increase the Touschek lifetime by a factor 2 to 2.5 with normalized skew quadrupole gradients of 0.02 m^{-2} in the MAX IV 3 GeV storage ring. For a high-brightness operation mode [5] cases with a lower skew quadrupole excitation, leading to a vertical emittance of 2 pm rad and a Touschek lifetime increase by 30%, have been studied as well.

The systematic SVD-based approach allows a thoughtful, reasonable trade-off between the targeted lifetime increase, required effort and possible risks in terms of deviations from design optics. By keeping deviations from design optics low the dynamic aperture of the design lattice is preserved and injection efficiency remains high.

Employing just two independently excited skew quadrupole families, deviations from design optics of the MAX IV

3 GeV storage ring can be reduced to a level that is comparable to deviations caused by lattice imperfections. Since vertical dispersion and betatron coupling are restricted to the arcs the source properties for IDs are not significantly altered except for the growth in vertical beam size due to the desired vertical emittance increase. By adding a third skew quadrupole family residual betatron coupling and vertical dispersion in the ID source points can be further reduced, however, considering the benefit during actual user operation the additional effort might not be justified.

Finally it remains to be emphasized that the presented approach to SCVDBs, starting from an ideal design lattice, is applicable to any ULE storage ring as long as a sufficient number of skew quadrupoles is available.

ACKNOWLEDGMENTS

One of the authors (J. B.) would like to thank Teresia Olsson for her helpful advice on the Tracy-3 code.

[1] C. Bernardini, G. F. Corazza, G. Di Giugno, G. Ghigo, J. Haissinski, P. Marin, R. Querzoli, and B. Touschek, Lifetime and Beam Size in a Storage Ring, Phys. Rev. Lett. **10**, 407 (1963).

[2] H. Bruck, *Accélérateurs circulaires de particules* (Presses Universitaires de France, Paris, 1966).

[3] A. Streun, Report No. SLS Note 18/97, https://ados.web.psi.ch/slsnotes/sls1897a.pdf.

[4] S. C. Leemann, Interplay of Touschek scattering, intrabeam scattering, and rf cavities in ultralow-emittance storage rings, Phys. Rev. ST Accel. Beams **17**, 050705 (2014).

[5] S. C. Leemann and M. Eriksson, Coupling and brightness considerations for the MAX IV 3 GeV storage ring, in *Proceedings of the 25th Particle Accelerator Conference, PAC, Pasadena, CA, 2013* (IEEE, New York, 2013), MOPHO05, p. 243.

[6] C. Steier, E. Forest, L. Nadolski, H. Nishimura, D. Robin, W. Wan, Y. Wu, and A. Zholents, Accelerator physics challenges of the fs-slicing upgrade at the ALS, in *Proceedings of the 20th Particle Accelerator Conference, PAC, Portland, OR, 2003* (IEEE, New York, 2003), WOAB006, p. 397.

[7] C. Steier, D. Robin, A. Wolski, G. Portmann, and J. Safranek, Coupling correction and beam dynamics at ultralow vertical emittance in the ALS, in *Proceedings of the 20th Particle Accelerator Conference, PAC, Portland, OR, 2003* (IEEE, New York, 2003), RPPG018, p. 3213.

[8] C. Montag, J. Bengtsson, and B. Nash, Touschek lifetime calculations and simulations for NSLS-II, in *Proceedings of the 22nd Particle Accelerator Conference, PAC, Albuquerque, NM, 2007* (IEEE, New York, 2007), FRPMS113, p. 4375.

[9] J. Bengtsson, Tracy-2 User's Manual (unpublished).

[10] S. C. Leemann, Å. Andersson, M. Eriksson, L.-J. Lindgren, E. Wallén, J. Bengtsson, and A. Streun, Beam dynamics and expected performance of Sweden's new storage-ring light source: MAX IV, Phys. Rev. ST Accel. Beams **12**, 120701 (2009).

[11] S. C. Leemann, Pulsed sextupole injection for Sweden's new light source MAX IV, Phys. Rev. ST Accel. Beams **15**, 050705 (2012).

[12] L. Liu, N. Milas, A. H. C. Mukai, X. R. Resende, and F. H. de Sá, The Sirius project, J. Synchrotron Radiat. **21**, 904 (2014).

[13] J. Biasci, J. Bouteille, N. Carmignani, J. Chavanne, D. Coulon, Y. Dabin, F. Ewald, L. Farvacque, L. Goirand, M. Hahn *et al.*, A low-emittance lattice for the ESRF, Synchrotron Radiat. News **27**, 8 (2014).

[14] J. Safranek, Experimental determination of storage ring optics using orbit response measurements, Nucl. Instrum. Methods Phys. Res., Sect. A **388**, 27 (1997).

[15] G. Wang, L. Yu, Y. Li, T. Shaftan, and L. Yang, NSLS-II storage ring coupling measurement and correction, in *Proceedings of IPAC, Richmond, USA, 2015* (IEEE, New York, 2015), TUPHA009, p. 1983.

[16] A. Wolski, Alternative approach to general coupled linear optics, Phys. Rev. ST Accel. Beams **9**, 024001 (2006).

[17] A. Wolski, D. Rubin, D. Sagan, and J. Shanks, Low-emittance tuning of storage rings using normal mode beam position monitor calibration, Phys. Rev. ST Accel. Beams **14**, 072804 (2011).

[18] A. W. Chao and M. J. Lee, Particle distribution parameters in an electron storage ring, J. Appl. Phys. **47**, 4453 (1976).

[19] A. W. Chao, Evaluation of beam distribution parameters in an electron storage ring, J. Appl. Phys. **50**, 595 (1979).

[20] G. Guignard, Reports No. CERN-ISR-BOM-79-30 and No. CERN-LEP-Note-154, 1979.

[21] J. Bengtsson and I. Pinayev, Report No. NSLS-II Tech Note 7, 2007.

[22] W. H. Press, S. A. Teukolsky, W. T. Vetterling, and B. P. Flannery, *Numerical Recipes: The Art of Scientific Computing*, 3rd ed. (Cambridge University Press, Cambridge, England, 2007).

[23] MAX IV Detailed Design Report, http://www.maxiv.lu.se/publications/, 2010.

[24] S. C. Leemann and H. Tarawneh, Impact of Insertion Devices on the MAX IV Storage Rings, in *Proceedings of IPAC, Richmond, USA, 2015* (IEEE, New York, 2015), TUPJE038, p. 1696.

[25] S. C. Leemann, MAX IV Internal Note 20121107, http://www.maxiv.lu.se/publications/.

[26] K. Ohmi, K. Hirata, and K. Oide, From the beam-envelope matrix to synchrotron-radiation integrals, Phys. Rev. E **49**, 751 (1994).

[27] A. Franchi, L. Farvacque, J. Chavanne, F. Ewald, B. Nash, K. Scheidt, and R. Tomás, Vertical emittance reduction and preservation in electron storage rings via resonance driving terms correction, Phys. Rev. ST Accel. Beams **14**, 034002 (2011).

[28] S. C. Leemann and A. Streun, Perspectives for future light source lattices incorporating yet uncommon magnets, Phys. Rev. ST Accel. Beams **14**, 030701 (2011).

Paper II

Equilibrium bunch density distribution with passive harmonic cavities in a storage ring

P. F. Tavares, Å. Andersson, A. Hansson, and J. Breunlin.

Physical Review Special Topics – Accelerators and Beams **17**, 064401 (2014).

PHYSICAL REVIEW SPECIAL TOPICS - ACCELERATORS AND BEAMS **17,** 064401 (2014)

Equilibrium bunch density distribution with passive harmonic cavities in a storage ring

Pedro F. Tavares, Åke Andersson, Anders Hansson, and Jonas Breunlin
MAX IV Laboratory, Lund University, P.O. Box 118, SE-221 00 Lund, Sweden
(Received 23 January 2014; published 17 June 2014)

The MAX IV storage rings, currently under construction in Lund, Sweden, will use third harmonic cavities operated passively to lengthen the bunches and alleviate collective instabilities. These cavities are an essential ingredient in the MAX IV design concept and are required for achieving the final design goals in terms of stored current, beam emittance, and beam lifetime—such performance challenges are in fact common to all recent ultralow emittance storage ring designs and harmonic cavities are currently under consideration in several laboratories. In this paper, we report on parametric studies comparing different harmonic cavity settings in terms of the resulting bunch length, peak bunch density, and incoherent synchrotron frequency spread for the MAX IV 3 GeV ring. The equilibrium longitudinal bunch density distribution was calculated by establishing a self-consistent equation for the bunch form factor, describing the bunch shape. The calculations are fully self-consistent in the sense that not only the amplitude but also the phase of the waves excited by the beam in the harmonic cavity were assumed to be a function of the bunch shape, which allowed us to explore a wide parameter range not restricted to the region close to the conditions for which the first and second derivatives of the total rf voltage are zero at the synchronous phase. Our results indicate that up to a factor 5 increase in rms bunch length is achievable with a purely passive system for the MAX IV 3 GeV ring while keeping a relatively large harmonic cavity detuning, thus limiting the unavoidable Robinson antidamping rate from the fundamental mode of a passively operated harmonic cavity to values below the synchrotron radiation damping rate. The paper is complemented by results of measurements performed in the MAX III storage ring, which showed good agreement with calculations following the fully self-consistent approach.

DOI: 10.1103/PhysRevSTAB.17.064401 PACS numbers: 29.27.Bd, 41.75.Ht

I. INTRODUCTION

The MAX IV facility [1], currently under construction in Lund, Sweden, includes a 3 GeV storage ring optimized for hard x rays and featuring ultralow emittance (down to 0.2 nm rad) and a 1.5 GeV storage ring optimized for soft x rays and UV radiation production. A 3 GeV linear accelerator plays the role of a full-energy injector into both rings as well as delivers the beam to a short pulse facility designed to produce spontaneous radiation from undulators with pulse lengths down to 100 fs.

A key ingredient in achieving stable operation of the MAX IV rings at high beam current (500 mA nominal stored beam current) is the use of a low frequency (100 MHz) rf system [2] and third harmonic rf cavities which, together, lead to rms bunch lengths on the order of 5–6 cm.

The long bunches are essential for achieving the ultimate design performance parameters of the MAX IV rings. In fact, it is only with lengthened bunches that the low emittance can be preserved under the action of intrabeam scattering and the design intensity can be guaranteed against coherent collective effects, in particular, the long bunches help to keep the heat load due to induced fields in vacuum chamber components at an acceptable level and avoid excitation of high frequency trapped (high Q) modes in the chamber structures and rf cavity higher order modes (HOMs). Additionally, the long bunches allow us to cope with coupled-bunch resistive wall instabilities [3] that are enhanced by the very compact design of the storage ring vacuum chamber [4], which is in turn a consequence of the compact magnet design [5] required to reach a very low emittance in a relatively short machine circumference through the multibend achromat lattice concept. Moreover, the harmonic cavities increase the synchrotron frequency spread within the bunches, thus enhancing Landau damping of collective instabilities.

All of the issues mentioned above are in fact common to many recent ultralow emittance storage ring designs and the possibility of using harmonic cavities is contemplated in new projects [6,7] as well as in upgrade proposals [8].

Harmonic cavities have been successfully used for many years in second and third generation light sources in both active [9] as well as passive [10–14] configurations. The basic theory is described in [15] and beam instability

analyses under the presence of harmonic cavities have been carried out by several authors (e.g. [16,17]).

In this paper, we focus on the MAX IV 3 GeV ring and describe calculations of the equilibrium longitudinal bunch density distribution in the double rf system (main and harmonic cavities), having in mind that the harmonic cavities will be operated passively, i.e., the fields in those cavities will be excited by the beam itself. Passive operation implies therefore that the fields excited in the harmonic cavities depend on the bunch density distribution, which, in turn, is determined by the sum of the fields in the main cavities and those in the harmonic cavities. Clearly a self-consistent solution for the density distribution needs to be found.

This problem has been treated by various authors before. In some cases (e.g [18]), the influence of the bunch shape on the excitation of the fields in the harmonic cavity is disregarded, i.e. the bunch lengths are assumed to be negligible when compared to the rf wavelength (even in lengthened conditions). In other cases [11], the influence of the bunch shape on the amplitude of the wave excited by the beam in the harmonic cavity is taken into account by introducing a bunch form factor F, which is equal to unity for a pointlike bunch and decreases as the bunches get longer, as a result of the reduced overlap of the bunch spectrum with the impedance of the fundamental mode of the harmonic cavity. In this way, a self-consistent equation is established for the determination of the equilibrium density distribution, in which the beam frequency spectrum depends on the bunch shape and the frequency response of the harmonic cavity depends on the cavity properties (shunt impedance, quality factor, tuning angle). A more direct, but more time consuming approach is to perform multiparticle tracking including the effects of the long-range wakefields of the harmonic cavities (e.g. [19]).

The self-consistent equation approach described above (which we call a *scalar* approach) works well for certain ranges of harmonic cavity settings (i.e. harmonic cavity shunt impedance and tuning angle). In particular, if the shunt impedance is low enough, the scalar approach is sufficient for any choice of tuning angle. Moreover, if the shunt impedance and tuning angle are close to the so-called flat potential conditions, in which the first and second derivatives of the longitudinal potential well are zero at the synchronous phase, the density distribution may safely be calculated using the scalar method. However, passive operation of the harmonic cavities implies operation on the Robinson unstable slope of those cavities, generating a Robinson growth rate that needs to be counteracted by other damping mechanisms such as synchrotron radiation damping and Robinson damping in the main cavities. This can be made easier if the harmonic cavities are tuned far away from resonance, which in turn implies the need for high shunt impedance to reach the necessary field amplitudes that provide enough lengthening. Such conditions, with high shunt impedance and far away from flat potential conditions may lead to a significant deformation of the bunch shape and cannot be treated by the scalar self-consistent approach. Instead, both the amplitude and the phase of the fields in the harmonic cavities must be assumed to depend on the bunch shape when writing up the self-consistent equations, which then become two dimensional—in other words, the bunch form factor that describes the excitation of fields in the harmonic cavities is now a complex number with an amplitude and a phase and we may define a fully self-consistent solution.

Once the equilibrium bunch density distribution is obtained, parameters such as the rms bunch length, the peak bunch density, and the distribution of incoherent synchrotron frequencies within the bunch can be calculated and used to compare different settings for the harmonic cavity system.

This paper is structured as follows. In Sec. II, we briefly review the theoretical background to calculations of the equilibrium bunch density distribution in double rf systems—the analysis here is general in the sense that it applies to both active and passive harmonic rf systems. We then go on, in Sec. II A, to the specific case of passive harmonic systems and consider the usual solution to the equilibrium bunch density distribution with the use of a real form factor for defining the bunch shape, whereas the fully self-consistent treatment with a complex form factor is described in Sec. II B. Section III shows the numerical results for the MAX IV 3 GeV ring case—first the difference between the scalar and fully self-consistent solutions is illustrated by analyzing two extreme cases, namely, a low shunt impedance/small detuning case and a high shunt impedance/large detuning case. We then define a metric to quantify the difference between the two approaches and identify the parameter region where the fully self-consistent approach is essential. The resulting beam density distribution is then analyzed and different harmonic cavity settings are compared. Finally, in Sec. IV we present results of longitudinal bunch profile measurements performed in the MAX III storage ring, which are compared to the calculated bunch distribution.

II. EQUILIBRIUM BUNCH DENSITY DISTRIBUTION IN DOUBLE RF SYSTEMS

Double rf systems have been analyzed by many authors (see e.g. [11,15]) to which we refer the reader for a detailed discussion. Below we list the relevant results and establish our notation and conventions. We assume a rf system composed of main and harmonic cavities so that the total accelerating voltage seen by the beam on every turn is given by

$$V_T(\varphi) = V_{\mathrm{MC}}(\varphi) + V_{\mathrm{HC}}(\varphi), \tag{1}$$

where $V_{\mathrm{MC}}(\varphi) = V_{\mathrm{rf}} \sin(\varphi + \varphi_s)$ is the main cavity voltage and $V_{\mathrm{HC}}(\varphi) = kV_{\mathrm{rf}} \sin(n\varphi + n\phi_h)$ is the harmonic cavity

voltage. The harmonic cavity is assumed to resonate at a frequency close to the nth harmonic of the radio frequency. The parameters k and ϕ_h define the amplitude and phase of the fields in the harmonic cavity. The equations of motion of a particle with phase deviation φ and relative energy deviation ϵ are

$$\frac{d\varphi}{dt} = \alpha_c \frac{2\pi h}{T_0}\epsilon, \tag{2}$$

$$\frac{d\epsilon}{dt} = \frac{1}{E_0 T_0}[e_0 V_T(\varphi) - U_0], \tag{3}$$

where α_c is the momentum compaction factor, h the harmonic number, E_0 is the nominal beam energy, T_0 is the revolution period, and U_0 is the energy loss due to synchrotron radiation per turn. The synchronous phase in the absence of a harmonic cavity (the unperturbed synchronous phase) is given by

$$e_0 V_{\rm rf} \sin\varphi_{s0} = U_0, \tag{4}$$

while the presence of the harmonic cavity causes the synchronous phase to shift to a new value φ_s given by

$$e_0 V_T(0) = e_0 V_{\rm rf}(\sin\varphi_s + k\sin n\phi_h) = U_0. \tag{5}$$

Note that we choose φ_s such that $\cos\varphi_s < 0$. The canonical equations of motion above can be derived from a Hamiltonian:

$$H(\varphi,\epsilon) = \frac{2\pi h\alpha_c}{T_0}\left\{\frac{1}{2}\epsilon^2 + \frac{Q_{s0}^2}{h^2\alpha_c^2}\frac{1}{\cos\varphi_{s0}} \times \int_0^{\varphi}\frac{e_0 V_T(\varphi') - U_0}{e_0 V_{\rm rf}}d\varphi'\right\}, \tag{6}$$

where we introduced the unperturbed synchrotron tune

$$Q_{s0}^2 = -\frac{h\alpha_c e_0 V_{\rm rf}\cos\varphi_{s0}}{2\pi E_0}, \tag{7}$$

and the corresponding equilibrium bunch density distribution is given by

$$\rho(\varphi,\epsilon) = \rho_0 \exp\left(-\frac{T_0}{2\pi h\alpha_c}\frac{H(\varphi,\epsilon)}{\sigma_p^2}\right) \tag{8}$$

where σ_p is the equilibrium relative energy spread determined by the interplay between quantum excitation and radiation damping. This distribution in the (φ,ϵ) phase space can be projected onto the φ axis to yield the longitudinal equilibrium bunch density distribution:

$$\rho(\varphi) = \rho_0 \exp\left(-\frac{1}{\alpha_c^2\sigma_p^2}\Phi(\varphi)\right), \tag{9}$$

where

$$\Phi(\varphi) = \frac{\alpha_c^2\sigma_p^2}{\cos\varphi_{s0}\sigma_{\phi 0}^2}\left\{\cos\varphi_s - \cos(\varphi+\varphi_s) + \frac{k}{n}[\cos n\phi_h - \cos(n\varphi + n\phi_h)] - (\sin\varphi_s + k\sin n\phi_h)\varphi\right\}, \tag{10}$$

where the natural bunch length is $\sigma_{\phi 0} = \frac{h\alpha_c}{Q_{s0}}\sigma_p$. The equations above are general in the sense that they apply to both actively and passively operated cavities. In the active case, however, both amplitude and phase can be chosen independently, whereas in the passive case, once the cavity shunt impedance is fixed (by its construction) only one parameter is available for optimization, namely, the cavity tuning angle (or equivalently the cavity resonant frequency). In particular, we may choose the harmonic cavity voltage and phase such that both the first and second derivatives of the voltage at the synchronous phase are zero and an approximately quartic potential well is formed. This is achieved when the harmonic cavity voltage and phase are [11]

$$k_{\rm fp} = \sqrt{\frac{1}{n^2} - \frac{1}{n^2-1}\left(\frac{U_0}{e_0 V_{\rm rf}}\right)^2}, \tag{11}$$

$$\tan n\phi_{h,\rm fp} = -\frac{\frac{nU_0}{e_0 V_{\rm rf}}}{\sqrt{(n^2-1)^2 - \left(n^2\frac{U_0}{e_0 V_{\rm rf}}\right)^2}}, \tag{12}$$

where the subscript fp identifies this as the *flat potential* case. This is possible for both passive and active operation, but in the passive case, once the harmonic cavity shunt impedance is fixed by its construction, these conditions are only reached at a given beam current and a given harmonic cavity detuning.

A. Scalar self-consistency

The response of the harmonic cavity to the excitation by the beam can be described by the cavity impedance [11]

$$Z_{\rm HC} = R_s\left(1 + iQ\frac{\omega_r^2-\omega^2}{\omega\omega_r}\right)^{-1} \approx R_s\left(1 + iQ\frac{2\Delta f}{f_r}\right) \tag{13}$$

where R_s is the cavity shunt impedance, Q the quality factor, and $\omega_r = 2\pi f_r$ is the resonant frequency. In terms of the harmonic cavity detuning Δf and tuning angle ψ_h

$$\Delta f = nf_{\rm rf} - f_r, \tag{14}$$

$$\tan\psi_h = 2Q\frac{\Delta f}{f_r}, \tag{15}$$

we may write the voltage induced in the cavity as

$$V_{\mathrm{HC}}(\varphi) = -2I_0R_sF\cos\psi_h\cos(n\varphi-\psi_h), \tag{16}$$

where I_0 is the stored beam current and we have introduced the (real) bunch form factor

$$F[\rho] = \left|\frac{\mathcal{F}[\rho(\varphi)]_{\omega=n\omega_{\mathrm{rf}}}}{\mathcal{F}[\rho(\varphi)]_{\omega=0}}\right| \tag{17}$$

given by the absolute value of the Fourier transform of the bunch density distribution at the nth harmonic of the radio frequency, normalized to the dc component and we identify

$$k = \frac{2I_0FR_s|\cos\psi_h|}{V_{\mathrm{rf}}}, \tag{18}$$

$$n\phi_h = \frac{\pi}{2}-\psi_h. \tag{19}$$

The equations above give us the recipe for finding $\rho(\varphi)$, namely, given the beam current, harmonic cavity shunt impedance, harmonic cavity tuning angle, and a bunch form factor, we calculate the harmonic cavity voltage from Eq. (16), determine the total voltage from Eq. (1) and corresponding potential from Eq. (10), and finally calculate the bunch density distribution from Eq. (9). Once the bunch density distribution is known, the bunch form factor can be calculated back from Eq. (17), which leads to a self-consistent equation in one variable (F) of the form

$$F = f(I,R_s,\psi_h,F), \tag{20}$$

where the functional form f stands for the series of calculations described in the preceding paragraph. The equilibrium bunch form factor, which is a solution of the equation above, can be easily determined numerically as the root of the penalty function (see Appendix C),

$$g(F) = F - f(I,R_s,\psi_h,F). \tag{21}$$

For the flat potential case, the required shunt impedance and harmonic cavity tuning angle are given by

$$R_{s,\mathrm{fp}} = \frac{k_{fp}V_{\mathrm{rf}}}{2IF_{\mathrm{fp}}|\cos\psi_{h,\mathrm{fp}}|}, \tag{22}$$

$$\psi_{h,\mathrm{fp}} = \frac{\pi}{2}-n\phi_{h,\mathrm{fp}}, \tag{23}$$

where k_{fp} and $\phi_{h,\mathrm{fp}}$ are given in Eqs. (11) and (12).

B. Full self-consistency

The full self-consistency is implemented by writing the harmonic cavity fields as

$$V_{\mathrm{HC}}(\varphi) = kV_{\mathrm{rf}}\sin(n\varphi+n\phi_h-\varphi_{\mathrm{FF}}), \tag{24}$$

where we have introduced the form factor phase φ_{FF} and the harmonic phase ϕ_h is determined by the harmonic cavity detuning ψ_h (Eq. 19), just as in the scalar case. The potential is obtained from Eqs. (5) and (10) by replacing $n\phi_h$ with $n\phi_h-\varphi_{\mathrm{FF}}$ and the same self-consistent equation (20) above can be used, but the form factor is now a complex quantity

$$\tilde{F} = |\tilde{F}|e^{i\varphi_{\mathrm{FF}}}, \tag{25}$$

which may be determined from the density distribution ρ by

$$\tilde{F}[\rho] = \frac{\mathcal{F}[\rho(\varphi)]_{\omega=n\omega_{\mathrm{rf}}}}{|\mathcal{F}[\rho(\varphi)]_{\omega=0}|}, \tag{26}$$

and the numerical root finding algorithm of the scalar case is replaced by a two-dimensional minimization of the penalty function (see Appendix C)

$$g(\tilde{F}) = |\tilde{F}-f(I,R_s,\psi_h,\tilde{F})|, \tag{27}$$

which gives us both amplitude and phase of the complex form factor $\tilde{F}$. Clearly both approaches lead to the same results when the form factor phase φ_{FF} is close to zero, which, as we will see, will be the case for conditions close to the flat potential case or for low harmonic cavity voltage ratios.

III. RESULTS AND DISCUSSION

Table I shows the MAX IV 3 GeV ring parameters assumed in the calculations reported in this paper. Only operation at full current (500 mA) was considered and all 176 bunches were assumed equally populated, which implies that our treatment does not consider transient effects[1] due to the presence of a gap in the bunch train. This limitation is, however, not a problem for the MAX IV case in its baseline configuration, which does not foresee the use of such gaps.

The equilibrium bunch parameters when no harmonic cavities are present (or when they are tuned far away from resonance) are shown in Table II. The harmonic cavity was assumed to operate at the third harmonic of the radio frequency and flat potential conditions are realized for $k = k_{\mathrm{fp}} = 0.277$, corresponding to $R_{s,\mathrm{fp}} = 2.017$ MΩ and $\psi_{h,\mathrm{fp}} = 103.717°$ or, equivalently a harmonic cavity detuning of $\Delta f = -28.43$ kHz, which leads to a rms bunch length of 54.1 mm, a peak bunch current of 8.9 A, and a perturbed synchronous phase $\varphi_s = 143.786°$.

These figures were confirmed by a direct solution of the scalar (21) and fully self-consistent (27) equations, as

[1]An extension of the proposed method to include transient effects could be considered by defining a separate complex form factor for each individual bunch. The self-consistent equations become, however, more involved and it is doubtful that this method would allow for a faster solution than direct multiparticle tracking in this case.

TABLE I. MAX IV 3 GeV ring parameters.

Parameter	Description	
E_0	energy	3 GeV
I_0	current	500 mA
T_0	revolution period	1.76 μs
f_{rf}	radio frequency	99.93 MHz
h	harmonic number	176
U_0	energy loss per turn	856 keV
α_c	momentum compaction factor	3.07×10^{-4}
Q_{s0}	small amplitude unperturbed synchrotron tune	1.994×10^{-3}
φ_{s0}	unperturbed synchronous phase	148.32°
τ_s	longitudinal radiation damping time	25.6 ms
σ_p	relative energy spread	7.82×10^{-4}
V_{rf}	peak rf voltage	1.63 MV
Q	harmonic cavity quality factor	21600

TABLE II. Equilibrium bunch parameters without harmonic cavities.

Parameter	Description	
σ_l	rms bunch length	10.1 mm
I_p	peak current	59.1 A
F	bunch form factor at third harmonic	0.998

shown in Fig. 1. Clearly, in that parameter range, the scalar and fully self-consistent approaches lead to essentially the same results. However, the small detuning implied by the flat potential brings about a significant Robinson growth rate from the interaction of the beam with the fundamental mode of the harmonic cavity. This growth rate (cf. Appendix B) is too large (67 s^{-1}) to be compensated by radiation damping alone (39 s^{-1}) and Robinson damping from the fundamental mode of the main cavity is required to maintain a stable beam under those conditions.

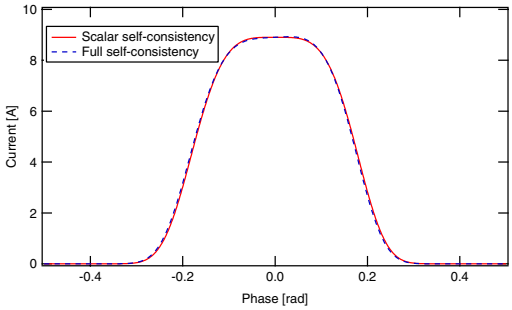

FIG. 1. Equilibrium density distribution for $R_s = 2.017$ MΩ and $\Delta f = -28.43$ kHz calculated with both scalar (solid line) and fully self-consistent (dashed line) approaches. The rms bunch length is 54.1 mm.

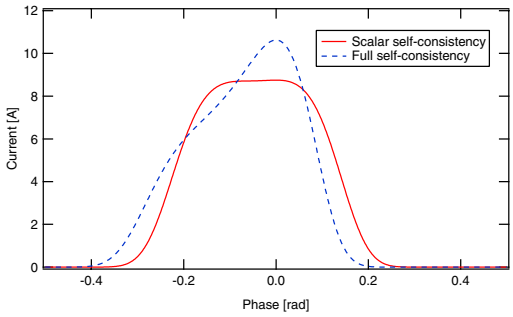

FIG. 2. Equilibrium density distribution for $R_s = 4.2$ MΩ and $\Delta f = -60.36$ kHz calculated with both scalar (solid line) and fully self-consistent (dashed line) approaches.

It is, however, possible to reduce the Robinson anti-damping due to the harmonic cavity while maintaining significant bunch lengthening, as long as we abandon the flat potential condition and allow the cavity detuning to grow while increasing the cavity shunt impedance. Such a situation is illustrated in Fig. 2, in which the self-consistent distribution calculated using both scalar and fully self-consistent approaches is shown for $R_s = 4.2$ MΩ and $\psi_h = 96.558°$ corresponding to $\Delta f = -60.36$ kHz. It is clear that a fully self-consistent calculation is mandatory under such conditions. We also see from the fully self-consistent results that, even far away from the flat potential conditions, we can reach a comparable rms bunch length (54.2 mm) at the cost of a slightly larger peak density (10.6 A) and an asymmetric bunch profile. The Robinson growth rate is then reduced by more than a factor 4 down to 15.3 s^{-1}, well within the range in which radiation damping alone can deal with it.

The results above indicate that for some (potentially interesting) parameter ranges, the scalar self-consistency is not capable of predicting the equilibrium density distribution correctly, which naturally raises the question of when one may safely apply the simpler scalar approach. In order to address that issue, we define the parameter ξ to compare two density distributions $\rho_1(\varphi)$ and $\rho_2(\varphi)$ and quantify how different they are,

$$\xi^2 = \frac{1}{2\pi}\int_{-\pi}^{\pi} [\rho_2(\varphi) - \rho_1(\varphi)]^2 d\varphi \tag{28}$$

where both ρ_1 and ρ_2 are normalized such that $\int_{-\pi}^{\pi} \rho_1(\varphi)d\varphi = \int_{-\pi}^{\pi} \rho_2(\varphi)d\varphi = 2\pi$.

Figure 3 shows the parameter ξ as a function of the product $R_s|\cos(\psi_h)|$, proportional to the harmonic cavity voltage for various values of the harmonic cavity detuning. For any cavity detuning, the difference between the two approaches becomes negligible as the harmonic cavity voltage decreases whereas for a fixed harmonic cavity voltage, the fully

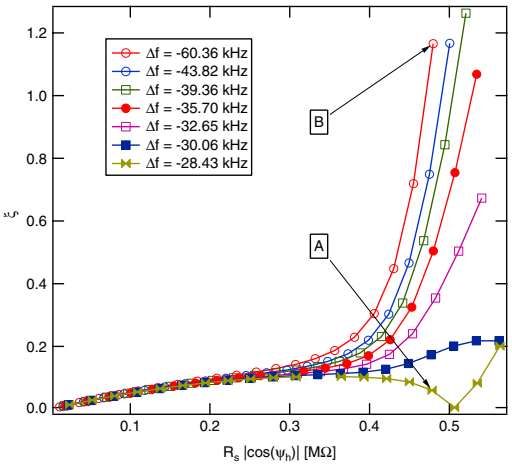

FIG. 3. Difference ξ between self-consistent and scalar solutions to the bunch density distribution as a function of $R_s|\cos\psi_h|$ for various values of harmonic cavity detuning. The points identified by A and B correspond to the cases displayed in the plots of Fig. 1 and Fig. 2, respectively.

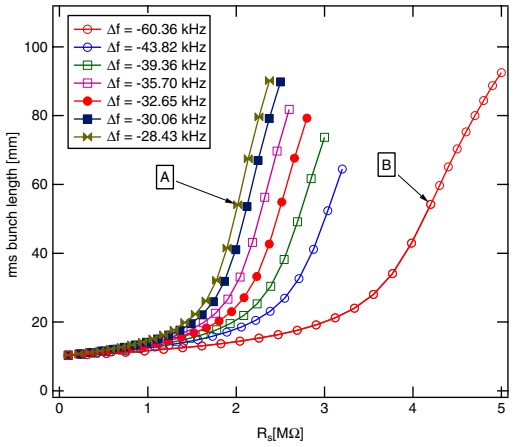

FIG. 4. The rms bunch length as a function of harmonic cavity shunt impedance for various values of harmonic cavity detuning. The points identified by A and B correspond to the cases displayed in the plots of Fig. 1 and Fig. 2, respectively.

self-consistent approach becomes essential as the harmonic cavity detuning is increased from the value corresponding to flat potential conditions[2] ($\Delta f = -28.43$ kHz). This plot confirms and details the trend illustrated by the two extreme cases explored above, which are indicated in Fig. 3 as points A and B.

In order to determine optimum values for shunt impedance and detuning parameters for the harmonic cavity system, we considered three properties of the resulting equilibrium bunch density distribution: rms bunch length, peak bunch density, and incoherent synchrotron frequency spread.

Figure 4 shows the rms bunch length vs shunt impedance for various values of harmonic cavity detuning. The bunch length grows monotonically with shunt impedance for all detuning values and we see that lengthening much larger than the lengthening corresponding to flat potential conditions may be obtained. However, as shown in Fig. 5, such overstretched conditions actually lead to peak densities somewhat above the minimum achievable. In fact, the peak density vs shunt impedance curves show a minimum at a shunt impedance value which decreases as the detuning decreases. That minimum peak density varies only slightly as the detuning increases. In other words, by going to larger shunt impedance and detuning (while keeping the harmonic cavity voltage approximately constant), one may obtain essentially the same rms bunch lengths at the cost of a slightly larger peak density. This is in fact the approach adopted for the MAX IV 3 GeV ring, where a significant margin in shunt impedance above the flat potential condition is provided by installing three identical harmonic cavities, each with a shunt impedance of 2.5 MΩ. Having the total shunt impedance split among three different

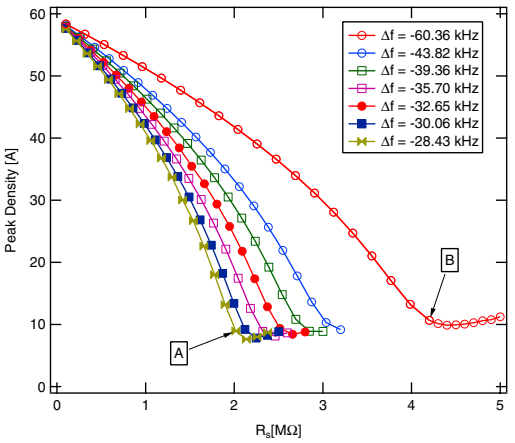

FIG. 5. Peak current as a function of harmonic cavity shunt impedance for various values of harmonic cavity detuning. The points identified by A and B correspond to the cases displayed in the plots of Fig. 1 and Fig. 2, respectively.

[2]Note that, if one reduces the detuning further from the flat potential case values towards zero, the difference between scalar and full self-consistency results for a given value of $R_s|\cos\psi_h|$ grows again (cf. Fig. 17 in Appendix C 2). However, this case has less interest in this context as it does not lead to reduced Robinson growth rates.

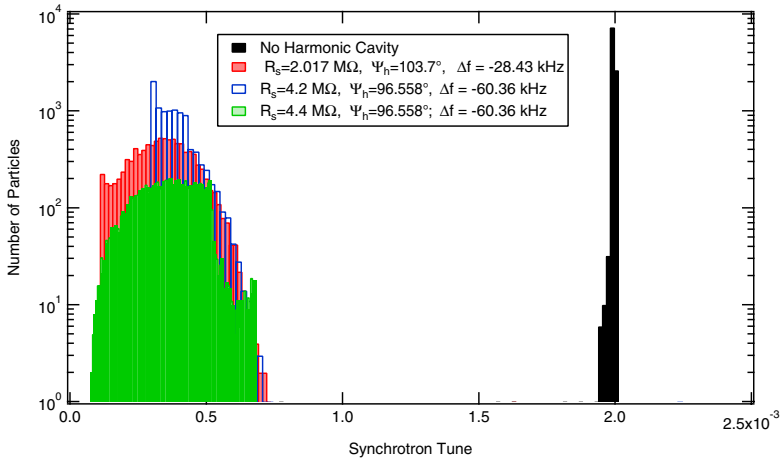

FIG. 6. Histogram of incoherent synchrotron tune distributions for different harmonic cavity settings. The tune distribution without harmonic cavities is shown for comparison.

cavities allows us to tailor the actual shunt impedance seen by the beam by tuning each cavity independently and additionally permits us to keep the power dissipated in each cavity within acceptable levels.

Another figure of merit that allows us to compare different choices of parameters for the harmonic cavity system is the incoherent synchrotron frequency spread, directly related to the Landau damping of collective instabilities. Figure 6 shows the numerically determined (see Appendix A) density distribution in synchrotron tune space for various cases. Compared to the situation without harmonic cavities, the average synchrotron tune is significantly reduced and the spread is increased when harmonic cavities are included. Even though this increase is larger for conditions close to the flat potential case ($R_s = 2.017$ MΩ) than for the high shunt impedance/large detuning case analyzed earlier ($R_s = 4.2$ MΩ), the tune spread can be reobtained for large detuning by going to even larger shunt impedance (see for example the case $R_s = 4.4$ MΩ in Fig. 6).

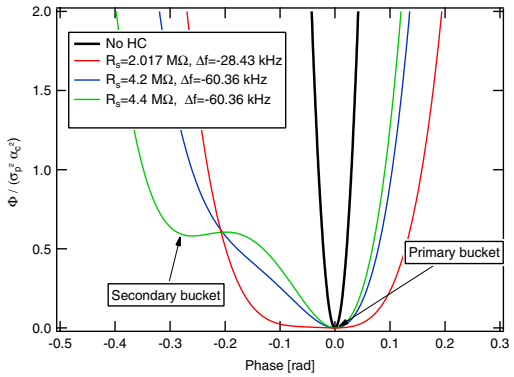

FIG. 7. Potential distribution for various settings of the harmonic cavity. The (approximately parabolic) potential when no harmonic cavity is present is also shown for comparison.

One can better understand those results by considering the behavior of synchrotron frequency as a function of the Hamiltonian invariant [Eq. (6)] and the corresponding potential functions [Eq. (10). As the potential well becomes wider (Fig. 7), the tunes are reduced and span a wider range as a function of the Hamiltonian invariant (Fig. 8). Moreover, instead of the usual decrease in synchrotron tune for increasing oscillating amplitude, which characterizes a single rf system, the double rf system actually shows an increasing synchrotron tune as a function of amplitude for amplitudes above a threshold value. This threshold value and the synchrotron tune at the threshold is lower when we are close to flat potential conditions than for the high impedance, large detuning conditions, implying a larger tune spread for the flat potential condition case.[3] However, as the shunt impedance is increased further, the minimum of the synchrotron tune at the threshold is decreased and approaches the flat potential situation, which causes the corresponding tune distribution to extend to lower synchrotron tunes in Fig. 6. Moreover, when the distortion of the potential well is so large that a second stable fixed point of the Hamiltonian (a secondary bucket) is created, as in the case of $R_s = 4.4$ MΩ, a new set of synchrotron

[3]Exactly at flat potential conditions, the synchrotron tune reduces to zero for vanishing oscillation amplitude.

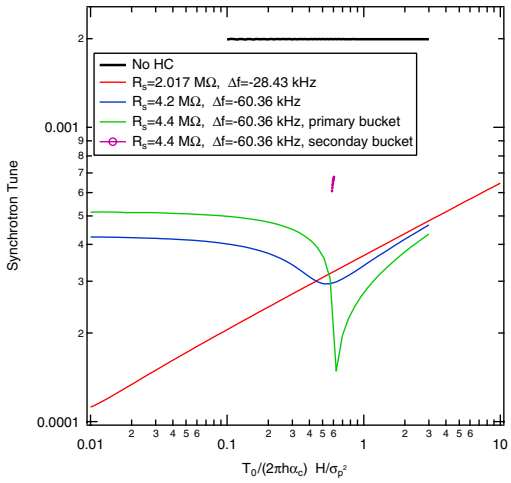

FIG. 8. Synchrotron tune as a function of the (normalized) Hamiltonian for various settings of the harmonic cavities. The (nearly constant) curve corresponding to the case without harmonic cavities is also shown for comparison.

frequencies, corresponding to oscillatory motion around this secondary synchronous phase, appears. These synchrotron frequencies are shown by the magenta curve in Fig. 8 and lead to the extended shoulder to the right of the corresponding tune distribution in Fig. 6.

IV. BUNCH PROFILE MEASUREMENTS IN THE MAX III STORAGE RING

MAX III is a third generation synchrotron light source with an electron energy of 700 MeV intended for synchrotron radiation generation in the infrared and ultraviolet region. It was commissioned in 2006 and characterized in 2008 [20]. The rf system in MAX III consists of three rf cavities: the main cavity at 100 MHz and two passive rf cavities at the third and the fifth harmonic. The fifth harmonic cavity was installed at the startup of MAX III and is currently detuned during regular user operation in order to avoid the excitation of coupled bunch modes by HOMs. The third harmonic cavity, a prototype for the MAX IV harmonic cavity [2], was installed in October 2011 and has been tuned in during user operation since then.

MAX III is equipped with a diagnostic beam line observing the visible synchrotron radiation emitted from the center of a dipole magnet [21]. In order to measure the longitudinal bunch shape, the time structure of the synchrotron light is resolved with an optical sampling oscilloscope (OSO). In the sampling head of the OSO, the incident light is focused and converted into photoelectrons at a photocathode. The electron path is bent by deflecting plates and swept over a slit. The electrons passing the slit impinge on a phosphor screen generating light which is transformed into an electric signal by a photomultiplier tube. The signal was sampled with 2048 points on a 2.4 ns time axis. The total data acquisition time was about 70 sec per measured bunch profile.

The relative energy spread was 6.0×10^{-4} and the momentum compaction was 0.03288 [22]. The main cavity voltage during the measurements was $V_{\mathrm{rf}} = 108 \pm 1$ kV and the rf was 99.925 MHz. The third harmonic cavity with $Q = 20430 \pm 40$ and $R_s = 2.68 \pm 0.015$ MΩ had a detuning $\Delta f = -197 \pm 1$ kHz. The fifth harmonic cavity with $Q = 21720 \pm 50$ and $R_s = 1.57 \pm 0.01$ MΩ was detuned by $\Delta f = -703 \pm 1$ kHz. Despite its large detuning, the fifth harmonic cavity contributes to the total accelerating voltage seen by the beam and has to be considered in calculations. In the case of the fully self-consistent approach applied to the triple rf system of MAX III, two independent complex form factors are required to calculate the voltages in each harmonic cavity. Numerically the self-consistency has to be found by a now four-dimensional minimization of the penalty function [compare Eq. (27)].

Figure 9 shows three examples of measured bunch shapes together with the corresponding calculations based on the fully self-consistent approach. At low currents (left-hand plot in Fig. 9), the effect of the harmonic cavities is negligible. The bunch shape is Gaussian and the bunch

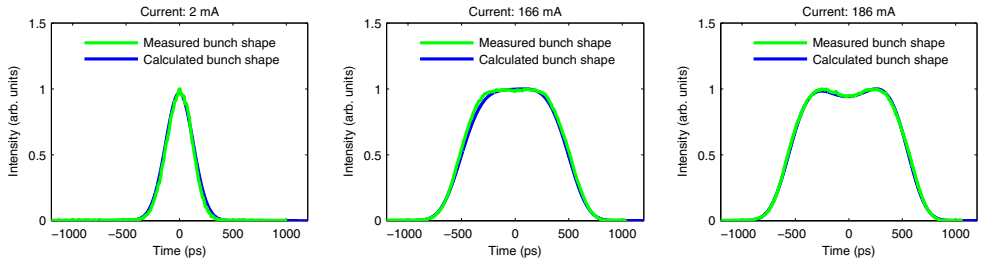

FIG. 9. Examples of measured bunch shapes compared to calculated density distributions. The calculations are based on the full self-consistency approach. Gaussian bunch (left) with natural bunch length at low currents. Elongated bunch (middle) close to flat potential conditions for medium currents. At higher currents (right) the bunch is overstretched by the harmonic cavities.

length is close to the natural bunch length. At medium currents, the fields in the harmonic cavities are excited and lead to bunch lengthening. The conditions for the middle plot in Fig. 9 are close to the flat potential conditions. At higher currents (right-hand plot in Fig. 9) the fields in the harmonic cavities overstretches the bunch and the density in the bunch center decreases.

In order to verify that the overstretched bunch shape was real and not a time-averaging artifact of the optical sampling oscilloscope, measuring on an unstable beam, a measurement of the shape of a single bunch (and in one turn) was done with a fast diode. Although the single-shot bunch shapes were noisy, it was still clear that the overstretched bunch shape was real.

The symmetry of the bunch density distributions suggests that, contrary to the MAX IV case, a treatment with full self-consistency is not required for the range of parameters covered in the MAX III experiments. In fact, the MAX III synchronous phase is closer to 180° and a relevant difference in the result of the scalar and fully self-consistent approaches is expected only for larger values of the harmonic cavity voltage ratio k, which were not accessible in MAX III (see Fig. 18 in Appendix C 2).

V. CONCLUSIONS

We have analyzed the effect of a passively operated third harmonic cavity in the MAX IV 3 GeV electron storage ring for a uniform fill (i.e. transient effects associated with the presence of a gap in the bunch train are excluded from the analysis). The calculation of a fully self-consistent equilibrium longitudinal beam density distribution, in which both the amplitude and phase of the waves excited by the electron beam in the harmonic cavity are assumed to depend on the bunch current and bunch shape, allowed us to explore a wide range of parameter settings for the harmonic cavity system.

Our results indicate that it is possible to achieve bunch lengthening in MAX IV by about a factor 5 with passive operation even if the harmonic cavity detuning is significantly increased in order to reduce Robinson antidamping due to the interaction of the beam with the fundamental mode of the harmonic cavity. Even though the bunch shape is no longer perfectly flat under those conditions, the rms bunch length is comparable to or longer than what can be obtained by setting the first and second derivatives of the rf voltage to zero at the synchronous phase. The peak bunch density becomes only slightly larger and a comparable incoherent synchrotron frequency spread can also be obtained. The price to be paid in order to allow operation in that regime is a significantly larger harmonic cavity shunt impedance. We have also shown that, under those circumstances, it is essential to take into account the dependence of the phase of the waves induced by the beam in the harmonic cavity on the bunch shape by establishing a fully self-consistent solution for the equilibrium bunch density distribution.

Finally, we found good agreement in a comparison of longitudinal bunch profile measurements done in MAX III with calculations following the fully self-consistent approach. We note that, for the MAX III parameters, the fully self-consistent approach gives approximately the same results as the scalar approach. The MAX IV 3 GeV ring will, on the other hand, offer the opportunity to cover experimentally a range of parameters in which the fully self-consistent method is essential.

ACKNOWLEDGMENTS

We thank Erik Wallén for highlighting the need to take the phase of the waves excited by the beam into account when calculating the equilibrium density distribution and Galina Skripka for help with the MAX III experiments.

APPENDIX A: EVALUATING EQUILIBRIUM BUNCH DENSITY DISTRIBUTIONS

Given the motivations listed in the introduction for lengthening the bunches, some obvious figures of merit which we can use to compare the effectiveness of two distributions generated by different harmonic cavity settings are the rms bunch length, the peak bunch density, and the distribution of incoherent synchrotron tunes. The first two parameters affect directly the beam lifetime (through the Touschek component) and the heat load on vacuum components due to interaction of the beam with the chamber impedance, whereas the third affects how the beam center-of-mass motion reacts to the wakefields produced by the beam itself. In fact, lengthening of the bunches alleviates the impact of coherent collective instabilities in two complementary ways—on the one hand by reducing the driving forces to the instabilities, i.e. reducing the excitation of unstable modes through a reduction of the overlap of the bunch spectrum with the machine impedance and on the other hand by reducing the responsiveness of the beam to those wakefields through an increase in synchrotron frequency spread and the ensuing Landau damping of the instabilities.

The calculation of the rms bunch length and peak bunch densities are trivial once the density distribution is known. In order to calculate the distribution of synchrotron tunes, we must first obtain the expression of the synchrotron period corresponding to a given oscillating orbit in (ϵ, φ) phase space, identified by the motion invariant H

$$T_s(H) = \frac{1}{Q_s(H)} = 2\int_{\varphi_-}^{\varphi_+} \frac{d\varphi}{\dot{\varphi}} = 2\int_{\varphi_-}^{\varphi_+} \frac{d\varphi}{\alpha_c \frac{2\pi h}{T_0}\sqrt{2\left(\frac{T_0}{2\pi h \alpha_c} H - \frac{\Phi(\varphi)}{\alpha_c^2}\right)}}. \quad \text{(A1)}$$

The integral is to be done over half an oscillation cycle, during which $\dot{\varphi}$ does not change sign and the integration limits correspond to two return points of the oscillation, where $\epsilon = \dot{\varphi} = 0$. For the limiting case of a single rf cavity, this reduces to a complete elliptic integral leading to the familiar decrease of the oscillation frequency as a function of invariant amplitude H. In the case of a double rf system tuned such that the first and second derivatives of the total rf voltage at the synchronous phase are zero, the potential Φ becomes approximately quartic close to the synchronous phase and the potential well is flat. Approximate expressions for the synchrotron period as a function of the invariant amplitude valid in that limit are given in [15]. For the general case of a double rf system tuned to arbitrary conditions, one is forced to resort to numerical integration. The area encircled by an oscillating orbit with invariant H is

$$A(H) = 2\int_{\varphi_-}^{\varphi_+} d\varphi \sqrt{2\left(\frac{T_0}{2\pi h\alpha_c}H - \frac{\Phi(\varphi)}{\alpha_c^2}\right)}, \tag{A2}$$

and the distribution of synchrotron tunes can be written as

$$\frac{dN}{dQ_s} = \rho(H)\frac{dA}{dH}\frac{dH}{dQ_s}, \tag{A3}$$

where the distribution $\rho(H)$ is given by Eq. (8).

Numerical calculation of the functions Q_s and A as a function of H then yields the tune distribution through the numerical differentiations above. Alternatively, one may construct histograms in tune space by generating a particle distribution in the (φ, ϵ) phase space following the distribution $\rho(H)$ and calculating the synchrotron tune for every particle.

Even though the procedure outlined above is general, one must keep in mind that, depending on the relative amplitudes and phases of the main and harmonic voltages, situations may arise in which additional stable fixed points of the Hamiltonian (i.e. more than one synchronous phase) exist within a narrow phase range. In that case, the tune of trajectories around each stable point must be calculated and the resulting distributions must be combined to generate the full distribution, since there is no longer a one-to-one relationship between the invariant H and a tune value—instead the same H value may correspond to different trajectories, around different stable fixed points.

APPENDIX B: ROBINSON GROWTH RATES FROM THE FUNDAMENTAL MODE OF THE HARMONIC CAVITY

The growth rate for the lowest order Robinson mode for a multibunch beam in the short bunch approximation driven by a high Q resonance of shunt impedance R_s and quality factor Q at the angular frequency ω_r close to the mth revolution harmonic is given by [23]

$$\tau^{-1} = \frac{I_0 e_0 \alpha_c \omega_0}{4\pi\omega_s E_0}\{(m\omega_0 + \omega_s)\Re(Z_0^{\|})(m\omega_0 + \omega_s) - (m\omega_0 - \omega_s)\Re(Z_0^{\|})(m\omega_0 - \omega_s)\}, \tag{B1}$$

where ω_0 is the angular revolution frequency, ω_s is the angular synchrotron frequency, and $Z_0^{\|}$ is a longitudinal resonator impedance

$$Z_0^{\|}(\omega) = \frac{R_s}{1 + iQ(\frac{\omega_r}{\omega} - \frac{\omega}{\omega_r})}. \tag{B2}$$

Figure 10 shows the real part of the harmonic cavity impedance and corresponding beam harmonic and synchrotron sidebands for the cases of Fig. 1 ($\Delta f = -28.43$ kHz, $R_s = 2.017\,\mathrm{M\Omega}$) and Fig. 2 ($\Delta f = -60.36$ kHz, $R_s = 4.2$ MΩ). In this range of parameters, the impedance terms can be simplified to

$$Z_0^{\|}(m\omega_0 + \omega_s) \approx Z_0^{\|}(m\omega_0) + \omega_s\frac{dZ_0^{\|}}{d\omega}(m\omega_0) \tag{B3}$$

so that the growth rate becomes

$$\tau^{-1} = \frac{I_0 e_0 \alpha_c \omega_0}{4\pi E_0} 2m\omega_0 \frac{dZ_0^{\|}}{d\omega}(m\omega_0), \tag{B4}$$

and we obtain finally

$$\tau^{-1} \approx \frac{I_0 e_0 \alpha_c \omega_0}{\pi E_0} R_s Q^2 \frac{(1-x^2)(x^2+1)}{x^4[1 + Q^2(\frac{1}{x} - x)^2]^2}, \tag{B5}$$

where $x = \frac{m\omega_0}{\omega_r}$.

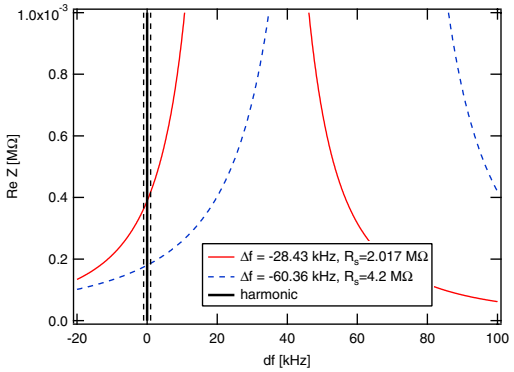

FIG. 10. Real part of harmonic cavity impedance for two different values of detuning and shunt impedances. The beam harmonic and synchrotron sidebands are indicated by the vertical black lines.

APPENDIX C: SOLVING THE SELF-CONSISTENT EQUATIONS

1. Direct solution

The Brent method [24] as implemented in IGOR [25] is used to obtain the numerical solution of the scalar self-consistent equation (20) for the real form factor F, or equivalently to find the roots of the penalty function g defined in Eq. (21). On physical grounds, the roots are conveniently bracketed to the interval [0, 1]. Figure 11 shows example plots of the penalty function g for two different sets of harmonic cavity shunt impedance and harmonic cavity tuning angle.

In order to solve the fully self-consistent equation (27), the IGOR implementation of the optimization method by Dennis and Schnabel [26] is used to obtain approximate zeros of the penalty function $g(\tilde{F})$, where $\tilde{F}$ is the complex form factor. Again, we can bracket the search for a minimum of g to the interval $(0 < |\tilde{F}| < 1)$ and $(-\pi < \varphi_{\mathrm{FF}} < \pi)$. A rough search on a rectangular grid within this interval is used to generate an initial guess for the desired root as an input to the minimization algorithm.

Figure 12 shows a contour plot of the penalty function g for $R_s = 2.017$ MΩ and $\Delta f = -28.43$ kHz on the $(|\tilde{F}|, \varphi_{\mathrm{FF}})$ plane. While at this relatively low harmonic cavity shunt impedance the penalty function g presents a single root in the interval $(-\pi < \varphi_{\mathrm{FF}} < \pi)$, for combinations of shunt impedance and tuning angle such that two minima of the potential function (or two stable fixed points of the corresponding Hamiltonian) are formed, the penalty function has more than one root, as can be seen in the contour plot in Fig. 13, which is calculated for $R_s = 4.4$ MΩ and $\Delta f = -60.36$ kHz. Note however that the various possible solutions correspond to the same physical situation, but with a different (arbitrary) choice of synchronous phase—one can indeed choose any of the extrema (maxima or minima) of the potential function as a synchronous phase φ_s in the equation defining the cavity voltage $V_{\mathrm{MC}}(\varphi) = V_{\mathrm{rf}} \sin(\varphi + \varphi_s)$ without changing any of the equations in Sec. II. In other words, the self-consistent equations as written in Secs. II A and II B assume a phase coordinate whose origin ($\varphi = 0$) is always

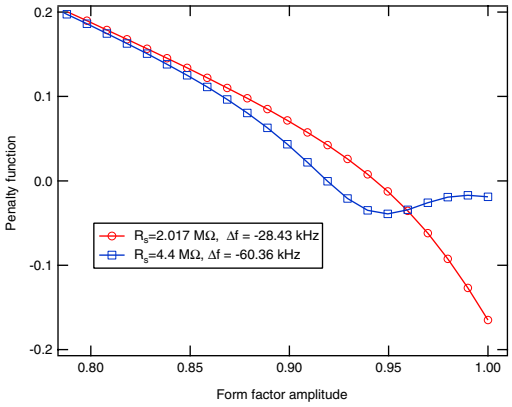

FIG. 11. Penalty as a function of the scalar form factor for low and high harmonic cavity shunt impedance cases.

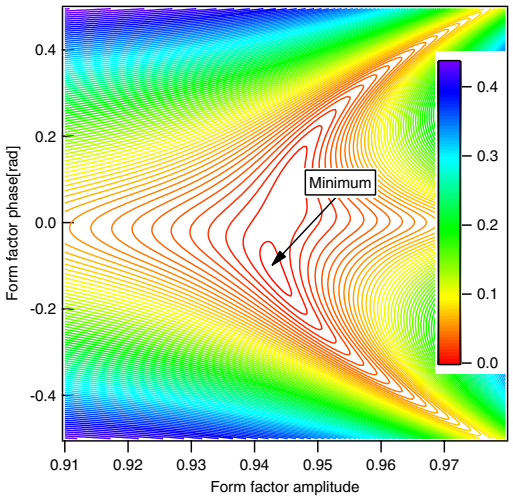

FIG. 12. Contour plot of the penalty function g for $R_s = 2.017$ MΩ and $\Delta f = -28.43$ kHz.

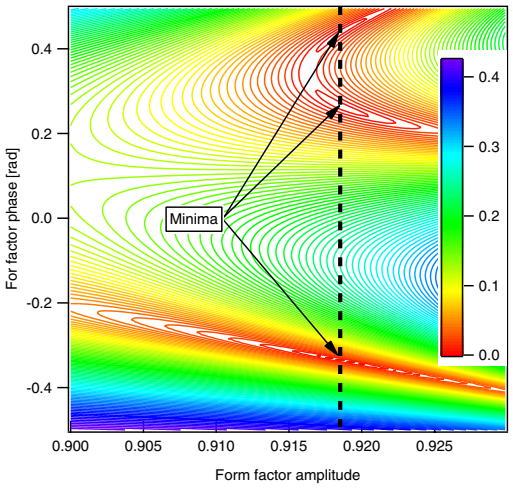

FIG. 13. Contour plot of the penalty function g for $R_s = 4.4$ MΩ and $\Delta f = -60.36$ kHz. The origin of the phase coordinate is chosen such that $V_{\mathrm{MC}}(\varphi) = V_{\mathrm{rf}} \sin(\varphi + \varphi_s)$. The vertical dashed line indicates the form factor amplitude value corresponding to all three minima.

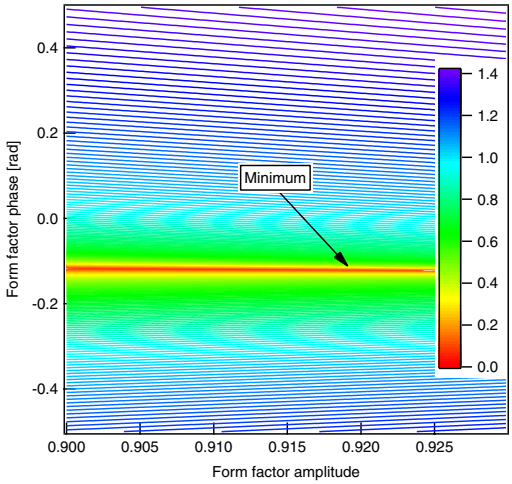

FIG. 14. Contour plot of the penalty function g for $R_s = 4.4$ MΩ and $\Delta f = -60.36$ kHz. The origin of the phase coordinate is chosen such that $V_{\mathrm{MC}}(\varphi) = V_{\mathrm{rf}} \sin\varphi$.

at a point for which the energy gain from the main cavity exactly compensates for the energy lost to synchrotron radiation as well as the energy loss to excite the fields in the harmonic cavity—and more than one phase satisfying that condition may exist.

Since any one of those possible solutions leads to the same physical properties (bunch length, bunch density, synchrotron frequency spread), this has no practical consequences, except if one is interested in comparing distributions calculated with different methods, as done in Sec. III. In order for Eq. (28) to be a valid comparison, one has to make sure that both calculations are done with the same phase axes origin and a convenient way to do that is to rewrite the equations in Secs. II A and II B in the phase coordinate system for which the main cavity voltage is $V_{\mathrm{MC}}(\varphi) = V_{\mathrm{rf}} \sin(\varphi)$. When this is done, the g function has a single minimum in the interval $(-\pi < \varphi_{\mathrm{FF}} < \pi)$, as shown in Fig. 14. As expected, the calculated self-consistent form factor amplitude is independent of the choice of phase coordinate system origin.

2. Implicit solution

Even though the approach described above is straightforward and conceptually simple to describe, it is possible to determine self-consistent solutions without actually solving the self-consistent equations by first determining a density distribution and calculating back the shunt impedance and tuning angle that correspond to that solution. This "implicit" solution approach has the advantage not to involve any iterative numerical procedure, with associated convergence issues, and is useful as a cross-check as well as a way to illustrate some of relevant scaling laws of the problem.

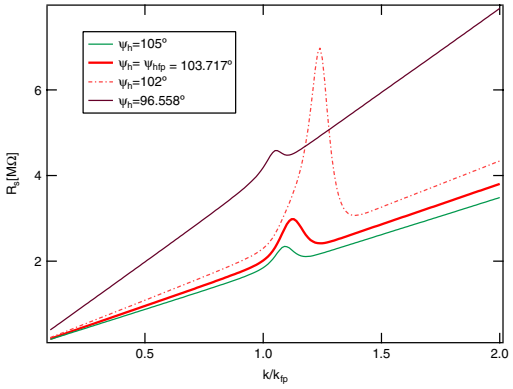

FIG. 15. Shunt impedance vs harmonic voltage ratio normalized to the flat potential voltage ratio k_{fp} for different harmonic cavity tuning angles.

For the scalar self-consistency problem, the implicit approach consists in taking an assumed ratio k of harmonic cavity voltage to main cavity voltage and determining the resulting density distribution, which gives the corresponding bunch form factor F. The shunt impedance that leads to that particular equilibrium is then calculated back from Eq. (18). Note that R_s has now become an output parameter of the problem, and by scanning a range of values of k one generates a set of values of R_s to choose from.

Figure 15 shows an example of such a calculation, for the MAX IV parameters. It is interesting to note that the shunt impedance vs k curve is not monotonic, i.e. the same value of shunt impedance may correspond to two different values of k—or correspondingly, as shown in Fig. 16, more than

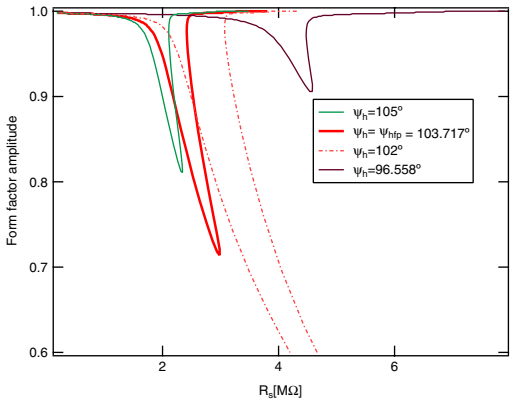

FIG. 16. Bunch form factor vs cavity shunt impedance for different values of harmonic cavity tuning angle.

one solution of the scalar self-consistent equation with different bunch form factors may exist for a given set of R_s, ψ_h values. In the direct approach described in the previous section, such cases show up in the form of multiple roots of the penalty function in the (0, 1) interval. There is, however, no fundamental physical meaning to these *degenerate* solutions—as soon as the full self-consistency is implemented, and both phase and amplitude of the bunch form factor are allowed to depend on the bunch distribution, the indeterminacy is eliminated and there is a single solution to the self-consistent equations. This is another indication of the limitations of the scalar approach to obtaining equilibrium distributions.

Following the same reasoning above, one may also implement an implicit solution for the full self-consistency problem, by making use of the following property of the potential function $\Phi(\varphi)$ and its corresponding distribution:

$$\Phi(k, \psi_h, \varphi_{\mathrm{FF}}; \varphi) = \Phi(k, \psi_h - \delta, \varphi_{\mathrm{FF}} + \delta; \varphi). \qquad \text{(C1)}$$

In other words, given assumed values for k, ψ_h, and φ_{FF}, the corresponding potential and density distribution functions do not change if we keep k fixed and shift the phases ψ_h and φ_{FF} by the same amount and in opposite directions. That gives us a simple recipe to construct self-consistent solutions (in the full self-consistency sense), namely, start with assumed values of k and φ_{FF}, determine the resulting distribution and calculate the corresponding form factor amplitude and phase. If the calculated form factor phase differs from the assumed φ_{FF}, then calculate a new tuning angle ψ_h shifted from the initially assumed ψ_h by the difference between assumed and calculated bunch form factors. Once a new ψ_h is determined, the shunt impedance may again be calculated as for the scalar case and we thus obtain a pair of values R_s, ϕ_h which self-consistently generates the distribution with the assumed k and φ_{FF}.

Even though the approach described in the preceding paragraph does provide a handy cross-check for the direct solution approach, it is not as convenient to use as the implicit approach for the scalar case—in fact, instead of a one-dimensional map from k to R_s one is now confronted with a two-dimensional nonlinear map from $(k, \varphi_{\mathrm{FF}})$ to (ψ_h, R_s).

We conclude this appendix by using the implicit solution to the scalar self-consistent equation to consider once more the issue of when the full self-consistency is mandatory. Full self-consistency will be relevant whenever the phase of the form factor calculated through the scalar approach is significantly different from zero. Figure 17 shows how the form factor phase determined by the scalar approach varies with harmonic cavity voltage ratio for different harmonic cavity tuning angles. We see the same trends as in Fig. 3, namely, that the difference between scalar and full self-consistency approaches increases significantly for harmonic cavity voltage ratios above the flat potential condition k_{fp}. Moreover, for k/k_{fp} slightly above 1, the differences become larger as the harmonic cavity tuning angle deviates from the flat potential detuning $\psi_{h,\mathrm{fp}}$. In particular, full self-consistency becomes important as the tuning angle is brought towards 90° in order to reduce the Robinson growth rate. Figure 18 shows the corresponding curves calculated for the MAX III parameters ($\phi_{s0} = 173.204°$, $\sigma_{\varphi 0} = 47.46$ mm) and indicates that the

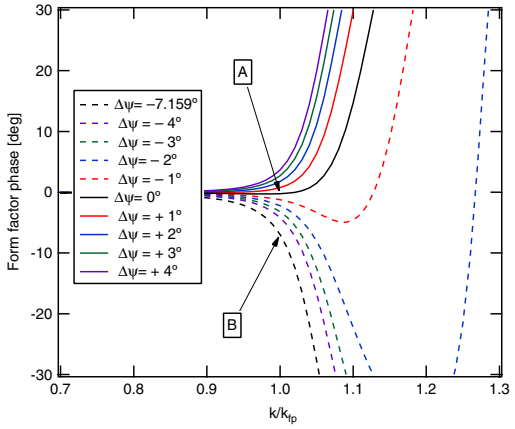

FIG. 17. Phase of the bunch form factor as determined by the implicit scalar approach, for the MAX IV parameters, as a function of the harmonic cavity voltage ratio k normalized to the flat potential voltage ratio k_{fp}. The curves are plotted for different values of $\Delta\psi = \psi_h - \psi_{h,\mathrm{fp}}$. The points identified by A and B correspond to the cases displayed in the plots of Figs. 1 and 2, respectively.

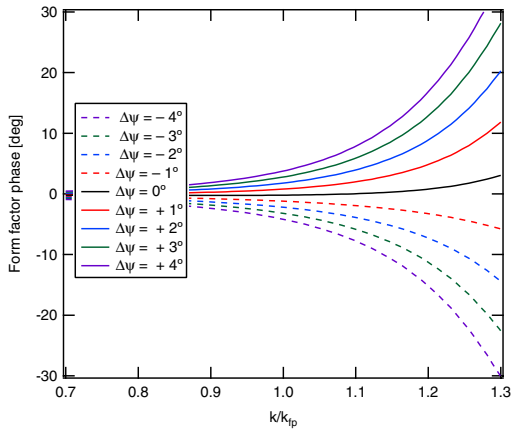

FIG. 18. Phase of the bunch form factor as determined by the implicit scalar approach, for the MAX III parameters, as a function of the harmonic cavity voltage ratio k normalized to the flat potential voltage ratio k_{fp}. The curves are plotted for different values of $\Delta\psi = \psi_h - \psi_{h,\mathrm{fp}}$.

full self-consistency is less relevant in that parameter range. This is basically a result of the larger unperturbed synchronous phase of MAX III compared to MAX IV, which leads to a larger flat potential harmonic cavity voltage ratio k_{fp} and to a flat potential tuning angle $\psi_{h,\mathrm{fp}}$ closer to 90°, making higher shunt impedances necessary to enter a regime significantly far from flat potential conditions.

[1] M. Eriksson, J. Ahlbäck, Å. Andersson, M. Johansson, D. Kumbaro, S. C. Leemann, C. Lenngren, P. Lilja, F. Lindau, L.-J. Lindgren, J. Modéer, J. Tagger, P. F. Tavares, S. Thorin, E. Wallén, S. Werin, B. Anderberg, and L. Dallin, in *Proceedings of the 2nd International Particle Accelerator Conference, San Sebastián, Spain* (EPS-AG, Spain, 2011), pp. 3026–3028.

[2] Å. Andersson, E. Elafifi, M. Eriksson, D. Kumbaro, P. Lilja, L. Malmgren, R. Nilsson, H. Svensson, P. F. Tavares, J. Hottenbacher, A. Salom, and A. Milan, in *Proceedings of the 2nd International Particle Accelerator Conference, San Sebastián, Spain* (EPS-AG, Spain, 2011), pp. 193–195.

[3] P. F. Tavares, R. Nagaoka, and T. F. Günzel, in *Proceedings of the 2nd International Particle Accelerator Conference, San Sebastián, Spain* (EPS-AG, Spain, 2011), pp. 754–756.

[4] E. Al-Dmour, D. Einfeld, J. Pasquaud, M. Quispe, J. Ahlbäck, P. F. Tavares, and M. Grabski, in *Proceedings of the 2nd International Particle Accelerator Conference, San Sebastián, Spain* (EPS-AG, Spain, 2011), pp. 1554–1556.

[5] M. Johansson, B. Anderberg, and L.-J. Lindgren, in *Proceedings of the 2nd International Particle Accelerator Conference, San Sebastián, Spain* (EPS-AG, Spain, 2011), pp. 2427–2429.

[6] A. Blednykh, S. Krinsky, B. Podobedovs, J. Rose, N. Towne, and J.-M. Wang, in *Proceedings of the 21st Particle Accelerator Conference, Knoxville, TN, 2005* (IEEE, Piscataway, NJ, 2005), pp. 2544–2546.

[7] L. Lin, N. Milas, A. Mukai, X. R. Resende, A. R. D. Rodrigues, and F. de Sá, in *Proceedings of the 4th International Particle Accelerator Conference, IPAC-2013, Shanghai, China* (JACoW, Shanghai, China, 2013), pp. 1874–1876.

[8] R. Bartolini and T. Pulampong, in *Proceedings of the 4th International Particle Accelerator Conference, IPAC-2013, Shanghai, China* (JACoW, Shanghai, China, 2013), pp. 237–239.

[9] R. Biscardi, S. L. Kramer, and G. Ramirez, Nucl. Instrum. Methods Phys. Res., Sect. A **366**, 26 (1995).

[10] M. Georgsson, Å. Andersson, and M. Eriksson, Nucl. Instrum. Methods Phys. Res., Sect. A **416**, 465 (1998).

[11] J. M. Byrd and M. Georgsson, Phys. Rev. ST Accel. Beams **4**, 030701 (2001).

[12] M. Georgsson, W. Anders, D. Krämer, and J. M. Byrd, Nucl. Instrum. Methods Phys. Res., Sect. A **469**, 373 (2001).

[13] G. Penco and M. Svandrlik, Phys. Rev. ST Accel. Beams **9**, 044401 (2006).

[14] M. Pedrozzi, J. Raguin, W. Gloor, A. Anghel, M. Svandrlik, G. Penco, P. Craievich, A. Fabris, C. Passoti, E. Chiaveri, R. Losito, S. Marque, O. Aberle, P. Bosland, S. Chel, P. Bredy, and G. Devanz, in *Proceedings of the 11th Workshop on rf Superconductivity, Lübeck/Travemünde, Germany* (2003), pp. 91–94 [http://srf2003.desy.de/fap/paper/MoP25.pdf].

[15] A. Hofmann and S. Myers, CERN, Technical Report No. CERN-ISR-TH-RF/80-26, 1980.

[16] S. Krinsky and J. M. Wang, *Part. Accel.* ***17****, 109 (1985)*.

[17] R. A. Bosch, Phys. Rev. ST Accel. Beams **8**, 084401 (2005).

[18] M. Migliorati, L. Palumbo, and M. Zobov, Nucl. Instrum. Methods Phys. Res., Sect. A **354**, 215 (1995).

[19] M. Klein, R. Nagaoka, G. Skripka, P. F. Tavares, and E. Wallén, in *Proceedings of the 4th International Particle Accelerator Conference, IPAC-2013, Shanghai, China* (JACoW, Shanghai, China, 2013), pp. 1730–1732.

[20] M. Sjöström, E. Wallén, M. Eriksson, and L.-J. Lindgren, Nucl. Instrum. Methods Phys. Res., Sect. A **601**, 229 (2009).

[21] A. Hansson, E. Wallén, and Å. Andersson, Nucl. Instrum. Methods Phys. Res., Sect. A **671**, 94 (2012).

[22] A. Hansson, Å. Andersson, and E. Wallén, in *Proceedings of the 2nd International Particle Accelerator Conference, San Sebastián, Spain* (EPS-AG, Spain, 2011), pp. 1332–1334.

[23] A. W. Chao, *Physics of Collective Beam Instabilities in High Energy Accelerators* (John Wiley & Sons, New York, 1993).

[24] W. Press, S. Teukolsky, W. Vetterling, and B. Flannery, *Numerical Recipes in C* (Cambridge University Press, Cambridge, England, 1988).

[25] Wavemetrics, IGOR Pro 6.3 Reference Manual, http://www.wavemetrics.com.

[26] J. Dennis and R. Schnabel, *Numerical Methods of Unconstrained Optimization and Nonlinear Equations* (Society for Industrial and Applied Mathematics, Philadelphia, 1996).

PAPER III

Methods for measuring sub-pm rad vertical emittance at the Swiss Light Source

J. Breunlin, Å. Andersson, N. Milas, Á. Saá Hernández, and V. Schlott.
Nuclear Instruments and Methods in Physics Research A **803**, 55-64 (2015).

Nuclear Instruments and Methods in Physics Research A 803 (2015) 55–64

Contents lists available at ScienceDirect

Nuclear Instruments and Methods in Physics Research A

journal homepage: www.elsevier.com/locate/nima

Methods for measuring sub-pm rad vertical emittance at the Swiss Light Source

J. Breunlin [a,*], Å. Andersson [a], N. Milas [c], Á. Saá Hernández [b], V. Schlott [b]

[a] Lund University, MAX IV Laboratory, P.O. Box 118, SE-221 00 Lund, Sweden
[b] Paul Scherrer Institut, CH-5232 Villigen, Switzerland
[c] Laboratório Nacional de Luz Síncrotron, P.O. Box 6192, CEP 13083-970 Campinas - SP, Brazil

ARTICLE INFO

Article history:
Received 7 January 2015
Received in revised form
12 August 2015
Accepted 10 September 2015
Available online 24 September 2015

Keywords:
π-polarization
Synchrotron radiation
Low emittance
Interferometry
Diffraction

ABSTRACT

We report on methods capable of measuring a rms vertical electron beam size of 3 μm with a rms error of less than 10% at a diagnostic beamline at the Swiss Light Source (SLS). This corresponds to a vertical emittance of 0.6 pm rad with a 20% rms error. We showed this capability by presenting the theoretical basis for, and the data from, a series of measurements on a stable beam at 1.6 pm rad vertical emittance at the SLS. The methods presented utilized either π- or σ-polarized synchrotron radiation (SR) in the visible to ultra violet (vis-UV) spectral range. In addition to the established π-polarization method, we introduced a diffraction method with a potentially high resolution capability. Also an intensity imbalanced diffraction scheme was introduced, but was found to be prone to SR induced carbon contamination on optical elements.

1. Introduction

Future SR light sources will be able to reach vertical electron beam emittances below the pm rad level. Also damping rings for future colliding beam facilities aim towards this region. It is therefore of high importance to develop means to measure such small emittances.

Visible and near UV SR can be used to resolve vertical beam sizes at the few μm scale. This has been demonstrated by a first monitor built in 2008 at SLS for the determination of the vertical beam emittance [1]. The monitor uses the so-called *π-polarization method* to determine the vertical beam size from vertically polarized (π-polarized) vis-UV SR imaged onto a CCD camera. During measurements in 2011 the first monitor has reached its resolution limit [2] which is determined by a combination of many factors such as the transverse optical magnification of the source, the camera resolution but also the fact that complementary methods are not available.

As a part of the TIARA work package 6 [3] and in collaboration with the MAX IV Laboratory a new emittance monitor was designed and commissioned at the SLS. Besides an increased optical magnification the new monitor provided complementary measurement methods to the *π-polarization method*: the creation of a diffraction pattern of either vertically (π-) or horizontally (σ-) polarized SR from a simple, vertically centered, rectangular *diffraction obstacle*. See Fig. 1 for a schematic. The vertical beam size was then deduced from the detected diffraction pattern. A similar technique for beam size measurements using interferometry has originally been used at KEK with a double-slit interferometer and σ-polarized SR [4,5]. The diffraction obstacle, if it was not vertically centered in the path of the SR, enabled a diffraction method with imbalanced intensity contributions from below and above the mid-plane. This mode of operation was comparable to the intensity imbalance technique introduced in [6,7]. With a wide range of different widths of the diffraction obstacle and by using different SR polarizations we cross-checked our measurement results and reduced systematic measurement errors.

The commissioning of the new monitor started in the beginning of 2013 with a lens as the focusing element, see [8–10]. Experiences during commissioning had great influence on the design of the diagnostic beamlines at the MAX IV synchrotron light source [11,12].

In this work we investigated the achievable precisions of the available measurement methods, also with a perspective to the MAX IV light source. We present the principle of the different methods in Section 2 and describe the experimental setup of the SLS monitor beamline in Section 3. Section 4 we present vertical beam size measurements applying the introduced methods, taken during one dedicated low emittance machine shift at the SLS. Measurement results of the magnetic lattice functions at the source point and the horizontal beam size are given in Section 5.

* Corresponding author.
E-mail address: jonas.breunlin@maxlab.lu.se (J. Breunlin).

http://dx.doi.org/10.1016/j.nima.2015.09.032
0168-9002/

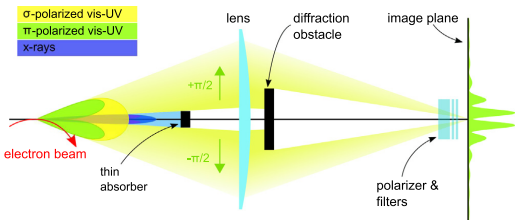

Fig. 1. Schematic of the new method using a vertically centered *diffraction obstacle*.

Section 6 presents the measurement results and ends with a discussion on the performance and limitations of the new monitor.

2. The methods

2.1. Theoretical foundation

The π-polarization method, described in [1,13], uses bending magnet SR in the vis-UV range that is focused to create an image of the electron beam. This image is highly dominated by effects inherent to SR emission and diffraction, especially for the π-polarized component of the SR. Since these effects are theoretically predictable it is possible to derive the horizontal and vertical size of the electron beam [14,15].

The theoretical calculations were done in Synchrotron Radiation Workshop (SRW) [16,17]. SRW is based on near-field calculations, preserving all phase information of the SR which is emitted by the electron beam while moving at relativistic velocity along its curved trajectory (in contrast to spherical waves originating from a point source, see Appendix A). It is required that the phenomena of SR emission, propagation and focusing are treated strictly within the framework of classical electrodynamics and wave optics, in order to derive a quantitatively correct intensity distribution in the image plane. The SRW code calculates the transverse components of the frequency-domain electric field of synchrotron radiation emitted by a relativistic electron moving in an external magnetic field, using an accurate method based on the Fourier transform of retarded potentials. It also allows the simulation of propagation of this field through optical elements and drift spaces of a beamline, using Fourier optics methods. Effects related to the finite emittance of the electron beam are accurately calculated as a convolution of the propagated single electron radiation intensities with the Gaussian phase-space volume occupied by the electron beam. One effect of this is seen in the image plane as a dilution of the fringes in the diffraction pattern. This feature is the basis for our *monitor response function* which is described in the following sections.

The applied SRW model was based on bending magnet radiation and included the relevant optical components and apertures of the beamline. Via an optical path length map the effect of the spherical aberration of the lens, as being the dominant Seidel (third-order) aberration, was included in the model: The optical path difference varies with the fourth power of the normal distance from the optical axis to the peripheral ray at the lens position. In our case it amounted to 7 nm for the outermost peripheral ray. The remaining Seidel aberrations were considerably suppressed by the small source size and the precise beamline alignment.

2.2. Imaging with π-polarized SR

The image of π-polarized SR in vertical projection typically shows two lobes of high intensity and a minimum between them,

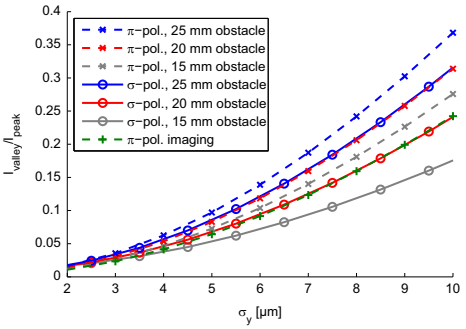

Fig. 2. Monitor response functions describing the relationship between the experimentally accessible valley-to-peak ratio and the vertical beam size. The monitor response functions were calculated in SRW for a wavelength of 325 nm for π-polarized (dashed lines) and σ-polarized (solid lines) SR and for different diffraction obstacle heights (15 mm corresponds to 3 mrad). The diffraction obstacles were vertically centered.

caused by a phase difference of the electric field of π between the upper and lower lobe, as can be seen from the solid line in Fig. 6. The ratio of the minimum intensity to the peak intensity, the *valley-to-peak ratio* (I_{valley}/I_{peak}), is identified with the vertical beam size in the theoretical SRW model, as established in [1]. The obtained relationship between the valley-to-peak ratio and the vertical beam size, the *monitor response function*, is shown in Fig. 2 for a wavelength of 325 nm. As a general behavior each monitor response function is steeper for shorter wavelengths, see for example [1].

In the case of π-polarized imaging the only relevant beamline component was the lens, since no restricting apertures (except horizontally) were used.

2.3. The obstacle diffractometer

In addition to the described imaging with π-polarized SR we performed measurements with simple rectangular diffraction obstacles of different heights, centered in the SR beam path. The diffraction obstacles were introduced into the SRW model and treated according to Section 2.1. The vertical intensity profiles of the resulting images are shown as solid lines in Figs. 8 and 9. The valley-to-peak ratio was again identified with the vertical beam size. For σ-polarized SR the low and high intensity regions were interchanged. By reason of experimental accessibility we did not relate the visibility to the vertical electron beam size, since for this a knowledge of the envelope functions of the intensity maxima and minima is required. The resulting monitor response functions are shown in Fig. 2. As a general behavior the response functions became steeper with increasing diffraction obstacle height, and with the use of π-polarized SR compared to σ-polarized SR. A method with a steeper monitor response function is favored for its higher sensitivity to the vertical beam size, resulting in a higher measurement precision for a given precision of the detected valley-to-peak ratio.

The obstacle diffractometer method resembled an interferometric method as presented in [5], where a double-slit has been used to create an interference pattern with σ-polarized SR. We expect, however, that the obstacle diffractometer technique is favorable in terms of beam size resolution for reasons given in Appendix B.

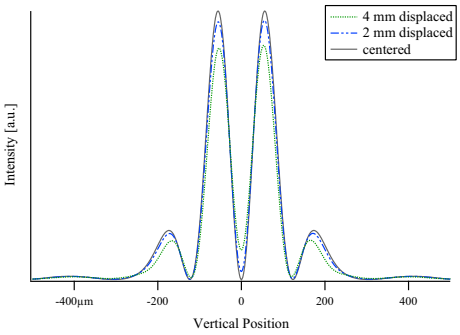

Fig. 3. Calculated vertical profiles of imaged π-polarized SR for a filament beam (zero electron beam size) for a centered and vertically displaced diffraction obstacles of 15 mm height. The imaging wavelength was 325 nm.

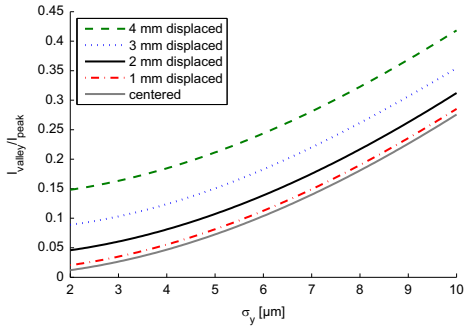

Fig. 4. Monitor response functions for a 3 mrad diffraction obstacle, vertically centered and displaced by 1–4 mm (0.2–0.8 mrad), calculated in SRW for π-polarized SR at a wavelength of 325 nm.

2.4. The intensity imbalanced obstacle diffractometer

If the diffraction obstacle was displaced vertically by a few millimeters (in this setup 1 mm at the position of the diffraction obstacle covers 0.2 mrad of the SR opening angle) from the SR mid-plane, the intensities from the upper and the lower lobes contributing to the image became imbalanced. In SRW this intensity imbalanced technique was modeled in analogy to the balanced case. In the imbalanced method the conditions for total destructive interference in the mid-plane were not fulfilled any longer for the filament beam, see Fig. 3. This led to a higher intensity in the central minimum (I_{valley}) for the same vertical beam size and might offer a way to improve the signal/noise ratio in the determination of the intensity minimum. The effect on the monitor response function in shown in Fig. 4. The same effect has been reached by introducing optical flats of different transmittances in a double-slit interferometer [6,7]. See Appendix B for a direct comparison of the two intensity imbalanced schemes. However, the slopes of the monitor response functions were not increased by the intensity imbalanced techniques which means that the monitor sensitivity was not generally improved.

3. Experimental setup

The beamline was designed to image the SR emitted by the electron beam in a bending magnet onto a CCD camera detector. See Fig. 5 for the beamline layout.

3.1. Beamline design

The source point of the radiation was the center of the central bending magnet ($B = 1.4035$ T) of sector 8 of the SLS. The beam energy was 2.411 GeV. Most of the SR power is emitted into a small vertical opening angle of $\propto 1/\gamma$, where γ is the Lorentz factor. This radiation, mostly x-ray SR, was absorbed by a thin absorber (4 mm height, covers approx. 0.9 mrad of vertical opening angle) to protect the subsequent optical elements from damage and heat-load induced surface deformation. This water-cooled absorber was retractable at low intensities (storage ring beam current of a few mA) to verify the camera alignment. The absorber was included in the theoretical model, however, its influence on the diffraction pattern was negligible: When imaging with π-polarized SR in the vis-UV range the intensity is close to zero around the mid-plane in the vicinity of the lens. For the obstacle diffractometer methods, the diffraction effects caused by the absorber were in all cases negligible when compared to those of the obstacle.

The beamline followed a zig-zag shape layout, defined by two planar mirrors, the first made of silicon carbide (SiC) because of its low ratio between expansion and heat transfer coefficients. The mirrors were held by *gimbal mounts*, pivoted supports that provided remote controlled angular adjustment. The lens, located between the mirrors at 5336 mm from the SR source, was plane-convex with a spherical surface. It was made of fused silica and had a diameter of 90 mm. The surfaces of the lens and the mirrors deviated with less than ± 15 nm from the ideal surfaces. Detailed information on the optical surface qualities is given in [10]. For the diffractometer methods an obstacle holder with rectangular diffraction obstacles of 15, 20 and 25 mm height (corresponding to 3, 4 and 5 mrad) was introduced into the beamline in vicinity of the lens. Their widths exceeded the horizontal acceptance of the beamline. Movable apertures, installed close to the second mirror, limited the horizontal acceptance angle at 4.4 mrad for imaging. The vertical acceptance angle was 9.5 mrad and was not limiting due to the vanishing SR intensity at large vertical angles.

The beamline was connected to the storage ring vacuum and was terminated with a vacuum window in an optics hutch, the beamline end station. The measurement wavelength was selected with interference bandpass filters of central wavelength 325 nm and a bandwidth of 1 nm FWHM. The used wavelength was a compromise between monitor response function (increasing slope at shorter wavelengths) and camera sensitivity. The choice of bandwidth is motivated in Section 3.3. A Glan–Taylor prism, made of pure calcite, was used to select the polarization of the SR. A CCD camera (Basler scA1300–32gm, pixel size 3.75 μm) was located in the image plane of the lens to record the beam images. The intensity response of the CCD was measured at a wavelength of 325 nm and over a large range of exposure times, while the light intensity was varied with neutral density filters. No significant deviation from a linear response were found. The distance along the optical path from the lens to the image plane was 10,072 mm, resulting in a transverse optical magnification of -1.888.

3.2. Alignment

The correct alignment of the lens is essential in order to minimize the Seidel aberrations coma and astigmatism. A laser beam from the beamline end station, aligned to the SR path, was reflected at both surfaces of the lens and formed the well-known *Newton's rings* interference pattern. From this pattern we deduced the angular alignment error of the lens, i.e. the angular deviation of the lens' optical axis w.r.t. the source-image axis. We reduced

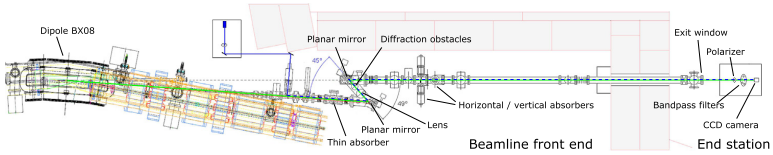

Fig. 5. Diagnostic beamline layout. The optical path of the SR is indicated from the source point in the center of the dipole magnet to the CCD camera in the beamline end station.

this alignment error to less than 2 mrad which allowed us to neglect third-order coma and astigmatism.

The detector needs to be aligned correctly to the laboratory reference system. We used the dipole SR for this purpose, since the bend plane of the dipole magnet is aligned in the laboratory coordinate system with a precision better than 0.1 mrad. With a retracted thin absorber the π-polarized SR intensity minimum along the mid-plane was detected and used to correct the roll (rotation around longitudinal axis) error of the CCD to within ± 3 mrad.

3.3. Design considerations

When considering a new beamline design, studies with a spherical mirror as focusing element were conducted. The main advantage of a spherical mirror is the high surface accuracy that can be attained, since the manufacturing process is simpler than for aspherical surfaces. But to keep Seidel aberrations within acceptable limits the angle of incidence must be chosen as small as possible which led to an unpractical, complicated design.

A spherical lens design combined the advantages of good surface accuracy and a simple way to verify a correct alignment. Under these conditions Seidel aberrations were predictable and were included in the theoretical model, although they were minor effects. The MAX IV diagnostic beamlines will be based on this design. As for all refractive optics, the focal length depends on the wavelength of the light, which required a bandwidth reduction to a few nm FWHM with interference filters. The use of such narrowband filters requires relatively large exposure times up to a few milliseconds. Therefore, special attention has to be paid to minimize vibrations. This will be accounted for in the MAX IV beamlines by a rigid design of vibration critical parts, such as mirror holders.

A toroidal mirror (replacing the lens and the first plane mirror) will be the future focusing element in the SLS beamline because of its aberration suppressing design combined with the advantages of reflective focusing optics. The wavelength independent focal length enables using a wider wavelength band than with refractive focusing optics resulting in a gain in light intensity. Furthermore a simpler change of the imaging wavelength is possible in practice. One disadvantage is the complicated alignment of the toroidal mirror due to the lack of a simple alignment verification technique [10]. Incorrect alignment affects image quality and measurement results due to aberrations. A first attempt with a toroidal mirror has already been performed [18], but the conclusion was that the image quality was inferior to the lens case, and thus an investigation of the toroid quality and its alignment was necessary. Furthermore, the effects of a broader wavelength band on the diffraction pattern need to be taken into account theoretically. However, once these difficulties are overcome the new SLS monitor beamline will benefit from the toroidal mirror in measurement precision, as a long term goal.

4. Beam size measurements

In several dedicated machine shifts during fall and winter 2013 the beamline performance was tested with small vertical emittance beams in the SLS. The storage ring was operated at design current and energy of 400 mA and 2.411 GeV, respectively. Prior to measurements the SLS was tuned towards small vertical emittance. The tuning was based on iterative response matrix measurement of 36 available skew quadrupoles (12 of them in dispersive sections), and subsequent matrix inversion and application of skew quad strengths for minimum vertical dispersion and minimum betatron coupling around the ring. On top of this, a random optimization was performed [2].

The data evaluated for this paper stem from one shift and one machine tuning. All measurement methods presented below were performed at 325 nm wavelength (1 nm FWHM). The CCD background signal was subtracted from all measured images before further analysis. This background was determined from the outer areas for each image since the diffraction pattern covered only a small fraction of the CCD in the center.

4.1. Imaging with π-polarized SR

Measured vertical profiles showed the characteristic double peak of the π-polarized SR above and below the mid plane (dots in Fig. 6). The valley-to-peak ratio of the profile was determined and transformed into a vertical beam size, according to the monitor response function for this method. A theoretical profile was calculated in SRW with the same vertical beam size and was scaled in the ordinate (SR intensity) to fit the peak intensity of the measured profile (line in Fig. 6).

For each method a set of 50 consecutive camera images was analyzed and the beam size was determined from each image. Fig. 7 shows a measurement set for π-polarized imaging. The error bars represent the single-shot random error for each of the 50 analyzed images. This random error was derived from the precision of the fits to the intensity minima and maxima in the measurement data to give a valley-to-peak ratio random error, which was propagated analytically via the monitor response function to the standard deviation of the vertical beam size σ_y. The source of these random errors, common to all methods applied, was to a large extent a vibration (~ 250 Hz) in either the mirrors or the lens. In order not to blur the image, we used exposure times no longer than 0.4 ms. As a consequence the images were underexposed and the occurring pixel noise limited the precision of the valley-to-peak ratio determination. On average the single-shot random errors corresponded well to the standard deviations from mean values presented in Table 1.

4.2. Obstacle diffractometer methods

The obstacle diffractometer method required that the diffraction obstacle was vertically centered in the path of the SR. The center position was found by a vertical scan of the diffraction obstacle position: according to theory the valley-to-peak ratio is minimized for a centered obstacle. Small deviations from the

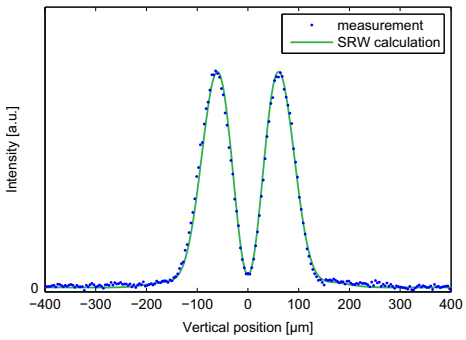

Fig. 6. Vertical profile of imaged π-polarized SR. The vertical beam size was $\sigma_y = 4.80 \pm 0.11$ μm, the valley-to-peak ratio was 0.059 ± 0.003.

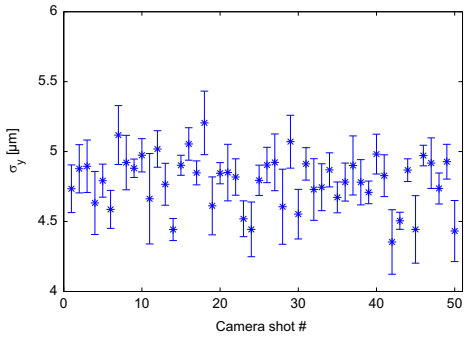

Fig. 7. Vertical rms beam sizes of 50 consecutive camera shots in the π-polarized imaging method. The error bars represent the standard deviation calculated for each single-shot measurement.

Table 1
Summary of beam size measurement results σ_y and their standard deviations for the applied methods.

Pol.	Diffraction obstacle angular size (mrad)	σ_y (μm)
π	–	4.79 ± 0.19
π	3	4.74 ± 0.14
π	4	4.70 ± 0.17
π	5	4.45 ± 0.22
σ	3	4.75 ± 0.19
σ	4	4.71 ± 0.18
σ	5	4.64 ± 0.19

center position (< 0.2 mm) were accounted for by adjusting the theoretical model accordingly. Even without such adjustments the effect on the final result was negligible (see the difference of the monitor response functions for the 1 mm displaced diffraction obstacle and the centered obstacle in Fig. 4). Measurements were taken for π-polarized and σ-polarized SR with all three available diffraction obstacles and were compared with the corresponding theoretical vertical profiles, see Figs. 8 and 9.

4.3. Intensity imbalanced obstacle diffractometer methods

We performed beam size measurements with the diffraction obstacle vertically displaced from the center position by up to 4 mm (up to 0.8 mrad) to each side, but the first analysis of the data revealed large, systematic inconsistencies of the final beam size results. Generally the vertical beam size was stronger underestimated the more the diffraction obstacle was displaced, see asterisks in Fig. 10 for an example with the displaced 3 mrad diffraction obstacle. The cause of this deviation from expected behavior turned out to be a reduction in transmittance of the beamline, probably due to the well-known problem of SR induced carbon contamination on beamline optics [19].

By investigating the relative SR intensity changes in the image plane when introducing the three differently sized centered diffraction obstacles, we compiled a map of a vertically non-uniform transmittance reduction of the beamline optics, see Appendix C. This map was included in the SRW model and affected predominantly the results for displacements larger than 1 mm (diamonds in Fig. 10). However, the evaluation of measurement data taken with higher diffraction obstacles and especially in σ-polarization still showed systematic beam size deviations in the 20% range. We believe that our simple approach to modeling SR induced carbon contamination, which takes only the reduction of transmission by the carbon layer into account, was insufficient. A refined model that includes also phase modifications of the SR might be necessary. However, our experimental data supports our assumption that the major discrepancies between theory and experiment are accounted for by introducing the transmission degradation.

Measurements with centered diffraction obstacles (or deviations from the center of less than 1 mm), nevertheless, were only slightly affected by the transmittance reduction model, as can be seen in Fig. 10, and were still valid. The intensity imbalanced obstacle diffractometer method, on the other hand, was prone to imperfections of the optics and was not applicable in the setup as it is. Only when having full knowledge about the effects of carbon contamination the advantage of this intensity imbalanced scheme can be accessed.

Further studies in SRW revealed that the intensity imbalanced scheme as introduced in [6,7], using optical flats of different transmittances in the SR path, was not sensitive to effects from carbon contamination as simulated in our SRW model (Appendix C). We therefore believe that an optical flat, creating different transmittances above and below the mid-plane, in combination with a centered diffraction obstacle, might be the favored setup for an intensity imbalanced scheme, although it requires additional experimental effort.

5. Auxiliary measurements

5.1. Magnetic lattice functions

The beta functions were determined by repetitive scans of individual quadrupole strengths and measurements of the resulting tune shifts. After each scan the betatron tunes were restored, rather than the individual quadrupole coil current, to avoid hysteresis effects. From the two quadrupoles adjacent to the sector 8 central bending magnet the beta functions in the SR source point (center of the bending magnet) were interpolated, using transfer matrices, to be $\beta_x = 0.481 \pm 0.008$ m and $\beta_y = 13.41 \pm 0.05$ m. A dispersion measurement was done with the monitor itself by observing the change in horizontal and vertical positions of the SR in the image plane when varying the rf frequency. By a variation $\Delta f_{rf} = \pm 1$ kHz in 21 steps a maximum relative momentum change of $\Delta p/p \approx \pm 0.0033$ was introduced. The results for the horizontal and vertical dispersion, derived using model based first and second order momentum compaction, were $\eta_x = 26.56 \pm 0.03$ mm and $\eta_y = -1.22 \pm 0.05$ mm.

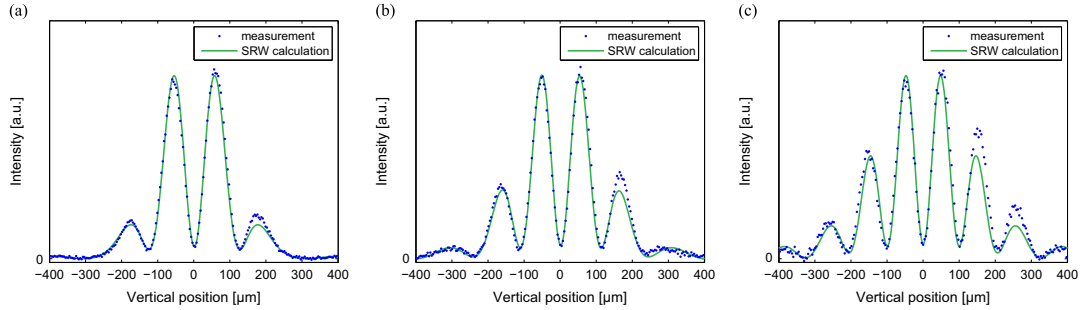

Fig. 8. Vertical profiles from obstacle diffractometer methods with three different diffraction obstacle heights, using π-polarized SR. (a) Diffraction obstacle covering 3 mrad, vertical beam size $\sigma_y = 4.81 \pm 0.13$ μm, valley-to-peak ratio $= 0.067 \pm 0.004$. (b) Diffraction obstacle covering 4 mrad, vertical beam size $\sigma_y = 4.68 \pm 0.16$ μm, valley-to-peak ratio $= 0.073 \pm 0.005$. (c) Diffraction obstacle covering 5 mrad, vertical beam size $\sigma_y = 4.58 \pm 0.19$ μm, valley-to-peak ratio $= 0.082 \pm 0.007$.

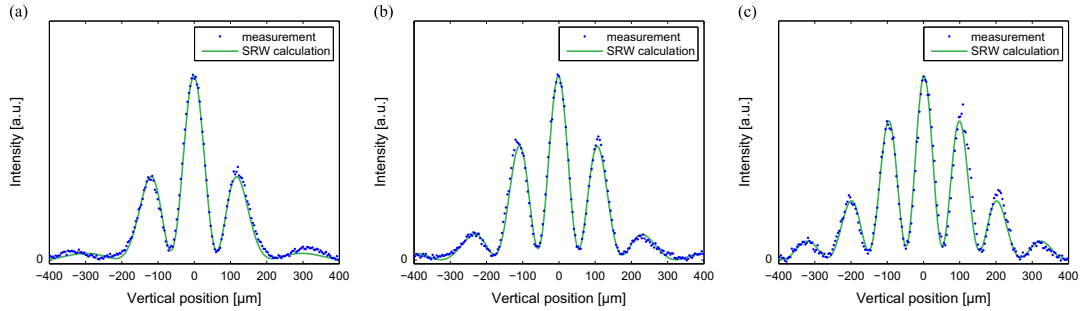

Fig. 9. Vertical profiles from obstacle diffractometer methods with three different interference obstacle heights, using σ-polarized SR. (a) Diffraction obstacle covering 3 mrad, vertical beam size $\sigma_y = 4.79 \pm 0.18$ μm, valley-to-peak ratio $= 0.052 \pm 0.003$. (b) Diffraction obstacle covering 4 mrad, vertical beam size $\sigma_y = 4.78 \pm 0.17$ μm, valley-to-peak ratio $= 0.062 \pm 0.004$. (c) Diffraction obstacle covering 5 mrad, vertical beam size $\sigma_y = 4.71 \pm 0.20$ μm, valley-to-peak ratio $= 0.076 \pm 0.006$.

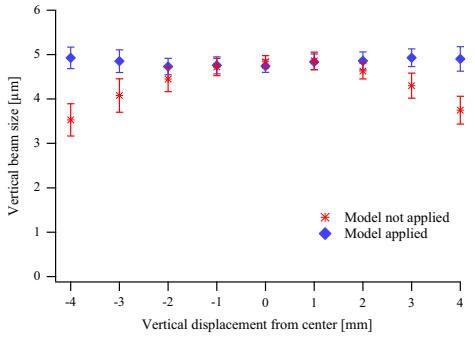

Fig. 10. Results of beam size measurements with the obstacle diffractometer method and 3 mrad (15 mm) diffraction obstacle height, displaced by −4 mm to 4 mm. The beamline transmittance reduction (Appendix C) was applied (diamonds) and not applied (asterisks).

5.2. Horizontal beam size

In contrary to the vertical profile, the horizontal profile of imaged SR is not dominated by diffraction because of the larger horizontal beam size of approximately 60 μm. We calculated horizontal intensity profiles of imaged SR with the same theoretical SRW model as for the vertical method described in Section 2.2 and at a wavelength of 325 nm. The widths of the calculated horizontal SR profiles were determined and identified with the horizontal electron beam sizes. The obtained relationship, now a monitor response function for horizontal beam size measurements, was then used to convert the experimental accessible widths of measured profiles to the horizontal electron beam size σ_x. In this way and under the same machine conditions as for the measurements in Section 4 we detected a horizontal beam size $\sigma_x = 59.8 \pm 0.8$ μm.

6. Results and discussion

6.1. Beam size results

Table 1 summarizes the measurement results for the vertical beam size from the applied methods. For reasons given in Section 4.3 the intensity imbalanced obstacle diffractometer methods were omitted. The vertical beam size result for each method is the mean value of 50 consecutive camera shots. The standard deviation is given for a comparison of the precision of the presented methods. Naturally a large derivative of the monitor response function leads to a higher measurement precision of σ_y. In this respect the method with π-polarized SR and widest diffraction obstacle would be preferred (Fig. 2). However, the precision of the fits to determine the extreme values of the diffraction pattern depended on the light intensity, especially in the minima. This could deteriorate the precision of methods with larger diffraction obstacles because of their intrinsically lower light intensity. Methods using σ-polarized SR had the advantage of a higher intensity due to a higher transmittance through the beamline, leading to comparable rms errors for the beam size result, although these methods were less sensitive in terms of monitor response functions.

In the present monitor design the light intensity in combination with the need for short exposure times due to vibration was the limiting factor (Section 4.1). Under these conditions and looking at Table 1, one may judge that the method with π-polarized SR using a moderate diffraction obstacle height, covering 3 mrad, is preferable.

6.2. Systematic errors

The effect of intensity reduction due to SR induced carbon contamination as a source for systematic errors is discussed in Sections 4.3 and Appendix C and was accounted for in the theoretical model. However, this model assumed a carbon contamination of vertical symmetry with respect to the central bending plane. The asymmetry in the measured vertical intensity profiles in Figs. 8 and 9 gives rise to the suspicion that either a slightly asymmetric carbon contamination or a non-uniform phase distortion from the thin carbon layer was present. It is interesting to note that a similar asymmetry in experimental data is present also in [4]. Different diffraction obstacle heights, leading to varying parts of the beamline optics that were covered, might have caused the observed discrepancies in the results from the applied methods. Furthermore, manufacturing errors of the optical components might explain the spread in results of the measurement methods. Even though the specifications on the surface qualities of the critical elements were driven to within ± 15 nm, one has to consider that the wavefront distortions caused by these optical surfaces might have added up and affected the final image.

6.3. Beam emittance results

With the results presented in Section 5.1 and Table 1 and according to [1] the horizontal and vertical emittances may be calculated:

$$\varepsilon_x = (\sigma_x^2 - (\sigma_\delta \eta_x)^2)/\beta_x \quad (1)$$

$$\varepsilon_y = (\sigma_y^2 - (\sigma_\delta \eta_y)^2(1 - (\sigma_\delta \eta_x/\sigma_x)^2))/\beta_y \quad (2)$$

It results in a horizontal emittance of $\varepsilon_x = 6.25 \pm 0.22$ nm rad and is in good agreement with the measured result in [1]. We assumed the theoretical, natural energy spread $\sigma_\delta = 9\ 10^{-4}$, since no beam instabilities were detected in this mode of operation. As indicated in Section 6.2 the spread of the results for the seven different methods presented in Table 1 is believed to be caused, to some extent, by systematic effects that could not be further specified. We combined these results by calculating their mean value, and the resulting vertical beam size is $\sigma_y = 4.68$ μm with a standard deviation of 0.11 μm. This leads to a vertical emittance of $\varepsilon_y = 1.56 \pm 0.08$ pm rad. In the presented case of the SLS beamline this standard deviation was determined to largest extent by the vertical beam size measurement error, and not by the measurement errors on the magnetic lattice functions.

Generally, the emittance uncertainties will grow with decreasing beta functions. Thus, the monitor performance in terms of emittance resolution will depend on the individual magnetic lattice and on the monitor location within this lattice. It is, however, expected, that the error contribution from the beam size and dispersion measurements will dominate over the error on the beta functions which are extracted to high precision by quadrupole scans, or by LOCO procedures [20].

6.4. Estimate of smallest measurable vertical beam size and emittance

To predict the monitor performance at smaller vertical beam sizes, smaller valley-to-peak ratios were investigated. These stem from the same measurement data as presented above, except that minima of higher order in the interference patterns (and thus, lower intensity, see Figs. 8 and 9) were analyzed. The analysis was conducted as described in Sections 4.1 and 4.2 with data sets of 50 camera images for both σ- and π-polarized SR and different centered diffraction obstacles. It showed that the measurement of a vertical beam size of $\sigma_y = 3$ μm with a standard deviation of less than 10% was feasible for the individual methods. In terms of vertical emittance this means $\varepsilon_y = 0.6$ pm rad with a standard deviation of 20%. A combination of the results from complementary methods has the potential to increase the measurement accuracy. The increased standard deviation, compared to the standard deviations of results presented in the previous sections, is due to the reduced slope of the monitor response functions for smaller beam sizes. These results refer to the present beamline and were, as mentioned above, limited in precision by the low SR intensity on the detector.

7. Conclusions

We analyzed the performance of several complementary beam size measurement methods using SR in the vis-UV range at a diagnostic beamline at the SLS. Combined with machine function measurements a vertical emittance of 1.56 pm rad with a standard deviation of 0.08 pm rad was determined. Extrapolating the analysis to smaller beam sizes, it would be possible with the beamline in the presented design to determine a vertical emittance of 0.6 pm rad with a 20% rms error, by using any of the methods. It is an interesting observation that, when analyzed theoretically, the obstacle diffractometer scheme showed an enhanced sensitivity to the vertical beam size in terms of a higher valley-to-peak ratio, compared to the traditional double-slit interferometer. Furthermore, the light transmitted to the detector is in general higher in the obstacle diffractometer scheme. We also investigated a simple intensity imbalanced obstacle diffractometer method, but found it prone to the problem of SR induced carbon contamination, and possibly to other minor deficiencies in the optical elements.

The limiting feature on the resulting precision of the present monitor design was light intensity in combination with the need for short exposure times due to vibration of an in-vacuum optical element. As a result of a trade-off between theoretically predicted sensitivity and limited light intensity of the present monitor a moderate diffraction obstacle covering 3 mrad performed best. Using a reflective focusing element instead of a lens, like a toroidal mirror, would alleviate the problem of low light intensities, since a wider bandwidth could be used.

8. Outlook

Currently, two diagnostic beamlines are in preparation in the 3 GeV storage ring at the MAX IV synchrotron light source [11,12]. These beamlines, following the concept presented in [1] and in this work, will allow a direct comparison of the obstacle diffractometer methods and the double-slit interferometric methods in experiment. The concept of two monitors in locations of different lattice functions enables cross-checking of measurement results and also presents a possibility to measure the energy spread of the beam. The multibend achromat lattice of the MAX IV 3 GeV storage ring and the resulting low emittance in both planes will be a new challenge to the emittance measurement methods.

Acknowledgments

We thank our colleagues from PSI; Andreas Streun for fruitful discussions, Masamitsu Aiba and Michael Böge for the low emittance operation of the SLS during measurements, and Martin Rohrer for the mechanical design of the beamline. We also thank Oleg Chubar for the correspondence and for his advice.

Appendix A. Analytical approach to the double-slit interferometer

In principle, the π-polarization method, the obstacle diffractometer method and the SR double-slit interferometer method are variations of the classical Young's double-slit interferometer. However, an important difference needs to be pointed out: in the classical case the transversely extended source is assumed to emit spherical waves isotropically, leading to a nearly homogeneous illumination of the interferometer slits. The SR radiation, on the other hand, has an intrinsic vertical opening angle, typically ± a few mrad at vis-UV wavelengths. Depending on the double-slit separation and slit widths the vanishing SR intensity at larger vertical angles causes an inhomogeneous illumination of the slits. Thus, we have a case which is not described correctly with the classical (visibility) formula from coherence theory of Van Cittert and Zernike, whereas the SRW code takes care of the feature highlighted above. To illustrate this, a comparison of double-slit interference patterns, calculated in SRW for a bending magnet (BM) SR source and calculated with an analytical expression for an isotropic source, was done.

The analytical approach follows the Fraunhofer diffraction and interference with quasi-monochromatic light [21]. The intensity profile of the source, denoted $f(y)$, is assumed to be Gaussian with a width of σ equal to the vertical electron beam size σ_y. The complex degree of spatial coherence is then calculated as the Fourier transform of the source:

$$\gamma(v) = \int f(y)\exp(-2\pi i v y)\, dy, \quad v = \frac{kd}{R} \tag{A.1}$$

where v is the spatial frequency with the center to center double-slit separation d and a distance R between source and double-slit and $k = 2\pi/\lambda$. The intensity as a function of the position on the detector y_0 is given by

$$I(y_0) \propto \sin c^2\left(\frac{ka}{R}\frac{y_0}{m}\right)\left\{1+\gamma(v)\cos\left(\beta - v\frac{y_0}{m}\right)\right\} \tag{A.2}$$

where $2a$ is the slit width, m the optical magnification of the system and the polarization is determined by

$$\beta = \begin{cases} 0 & \text{for } \sigma-\text{polarized SR} \\ \pi & \text{for } \pi-\text{polarized SR.} \end{cases} \tag{A.3}$$

The result of the analytical equation was compared to the calculations for a BM SR source, see Fig. A1. When the slit width was small the resulting interference patterns were in good agreement (Fig. A1(a)). For such a slit width the SR intensity variation over the slit, shown in Fig. A2, is small enough so that deviations from the analytically calculated interference pattern, assuming a homogeneously illuminated double-slit, are minor. For larger slit widths the characteristics of SR, treated correctly in the SRW model, had an increasing effect on the interference pattern (Fig. A1(b)) and the discrepancy between analytical model and SRW calculation grew. Here the interference pattern was dominated by the SR inherently limited vertical opening angle whereas the outer aperture restrictions of the double-slit were barely limiting (Fig. A2). Generally an interference (or diffraction) pattern from SR occurs without the need of outer vertical aperture restrictions (obstacle diffractometer methods) or even without any diffraction obstacle at all (imaging with π-polarized SR). The values for d and a were chosen to make the example comparable to the 25 mm (5 mrad)

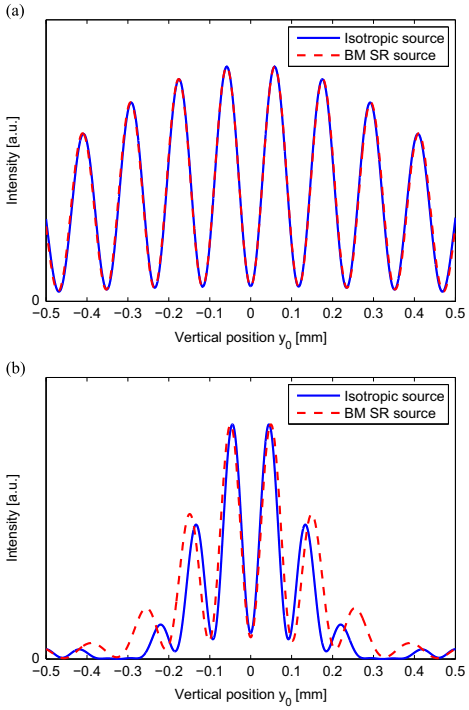

Fig. A1. Comparison of interference patterns calculated analytically for an isotropic source with Gaussian intensity profile (solid lines), following Eqs. (A.1) and (A.2), and calculated in SRW for a bending magnet (BM) SR source (dashed lines). The comparison was made for two double-slit interferometer configurations. The vertical beam size was $\sigma_y = 5$ μm and the wavelength was $\lambda = 325$ mm. (a) Double-slit separation $d = 27.5$ mm, slit width $2a = 2.5$ mm. (b) Double-slit separation $d = 35$ mm, slit width $2a = 10$ mm.

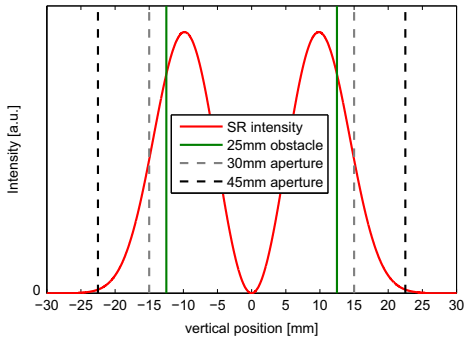

Fig. A2. Intensity of BM SR at the double-slit, calculated with SRW in π-polarization at 325 nm wavelength. The 25 mm diffraction obstacle and the 30 mm outer aperture form a double-slit of $d = 27.5$ mm, $2a = 2.5$ mm (Fig. A1(a)). The same diffraction obstacle and the 45 mm outer aperture form a double-slit of $d = 35$ mm, $2a = 10$ mm (Fig. A1(b)).

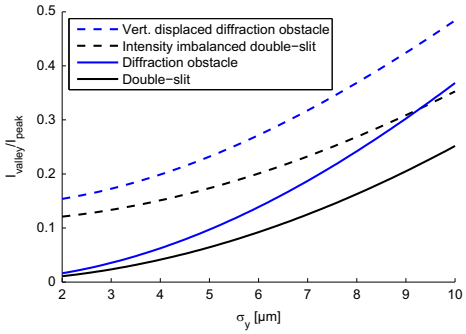

Fig. B1. Monitor response functions for the 5 mrad (25 mm) diffraction obstacle, centered (solid line) and displaced by 0.4 mrad (2 mm) (dashed line). Monitor response functions for a double-slit interferometer with $d=27.5$ mm slit separation and $2a=2.5$ mm slit width (solid line), and as an intensity imbalanced double-slit (dashed line). All response functions were calculated in SRW for SR of 325 nm wavelength and in π-polarization.

diffraction obstacle, for which a theoretical calculation of the diffraction pattern is presented together with experimental data Fig. 8(c).

Appendix B. Double-slit interferometer vs. obstacle diffractometer

The large vertical acceptance angle of our beamlines is an important design criterion. The beam size measurement methods based on the obstacle diffractometer, but also the π-polarization method, performed best in terms of the steepness of their response functions if the SR, emitted into larger vertical angles, contributed to the image. This can be understood with the classical Eqs. (A.1) and (A.2): increasing the vertical SR acceptance angle led effectively to an increased double-slit separation d. The consequence was an increased valley-to-peak ratio (in the classical picture: reduction in visibility), but also a higher sensitivity to the source size. Ideally, the beamline acceptance should therefore cover the full vertically emitted SR of the measurement wavelength to maximize its performance in terms of beam size resolution. In a double-slit interferometer, however, light emitted into larger vertical angles is blocked. Thus, a reduced performance in terms of beam size resolution was expected.

A simplified scenario based on the SLS beamline was modeled in SRW. The monitor response function for the 5 mrad (25 mm) diffraction obstacle in π-polarization was calculated. By adding a rectangular aperture restriction to the diffraction obstacle, a double-slit with a slit separation (center to center) of $d=27.5$ mm and a slit width of $2a=2.5$ mm was introduced (with the central part being identical to the 25 mm diffraction obstacle). The resulting monitor response functions are compared in Fig. B1 (solid lines). The method based on the 5 mrad (25 mm) diffraction obstacle showed a steeper response function (i.e. higher sensitivity to the vertical beam size) compared to the double-slit interferometer result. Another aspect in favor for the obstacle diffractometer method was the higher light intensity on the detector, a consequence of the effective increase in 'double-slit width a'. The difference between the π- and σ-polarization in the double-slit interferometer was minor in terms of response functions [22].

The intensity imbalanced double-slit interferometer was derived from the double-slit interferometer described above by reducing the transmittance to 0.5 on one slit only and the monitor response function was calculated. The intensity imbalanced obstacle diffractometer, with a 0.4 mrad (2 mm) vertical displacement of the diffraction obstacle from center, was calculated for a 5 mrad (25 mm) high diffraction obstacle. The resulting monitor response functions are compared in Fig. B1 (dashed lines).

The two intensity imbalanced approaches worked equally well in raising the valley-to-peak ratio for a given vertical beam size, but did not change the slope of the response function. The gain in valley-to-peak ratio was adjustable in both techniques by the choice of the vertical displacement of the diffraction obstacle and by the difference in transmittance through the double-slits, respectively. The intensity imbalanced obstacle diffraction method was, however, sensitive to the effects of carbon contamination on beamline optics, as described in Section 4.3.

Appendix C. Transmittance reduction model

Experience with former beamlines showed that the irradiation with the UV part of SR over weeks and months led to a degradation of the optical components. On mirrors with high SR irradiation a reduction of the reflectivity, visible by eye, was caused by carbon contamination [19].

To account for this effect in the theoretical model a reduction of transmittance through the beamline that is proportional to the local SR intensity was introduced. Since the total SR intensity (both polarizations, where the σ-polarization dominates) must be considered, an approximation with a Gaussian in the vertical plane was chosen. The highest SR intensity was in the mid-plane and reduced the transmittance to 65% of the initial value, see Fig. C1. The implementation in the SRW code was done by a flat optical element (no phase change) with an amplitude change as a function of vertical position, placed in vicinity of the lens. We validated this model by a relative comparison of the intensities between theoretical model and experiment when introducing diffraction obstacles of different heights, thus blocking varying areas on the optical components with varying transmittances. When including the transmittance reduction model, the measured reduced intensities were predicted by the SRW model within 1.4% of the measured intensities.

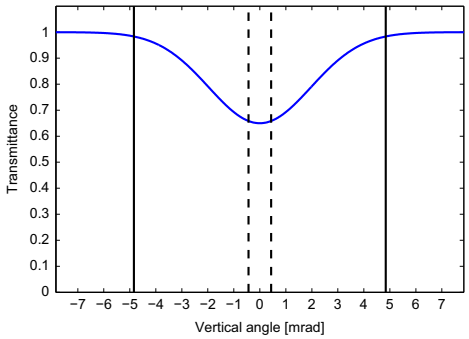

Fig. C1. Transmittance reduction function used to model the optical degradation of the experimental setup in SRW. The dashed lines show the vertical angle shadowed by the thin absorber and the solid vertical lines show the total vertical acceptance angle of the beamline.

References

[1] Å. Andersson, M. Böge, A. Lüdeke, V. Schlott, A. Streun, Nuclear Instruments and Methods in Physics Research A 591 (2008) 437.
[2] M. Aiba, M. Böge, N. Milas, A. Streun, Nuclear Instruments and Methods in Physics Research Section A: Accelerators, Spectrometers Detectors and Associated Equipment 694 (0) (2012) 133.
[3] ⟨http://www.eu-tiara.eu/rtd/index.php?id=42⟩, (accessed 03.08.15).
[4] T. Naito, T. Mitsuhashi, Physical Review ST Accelerators and Beams 9 (2006) 122802.
[5] T. Mitsuhashi, Measurement of small transverse beam size using interferometry, in: DIPAC, ESRF, France, 2001.
[6] M. Boland, T. Mitsuhashi, K. Wootton, Intensity imbalance optical interferometer beam size monitor, in: IBIC, Tsukuba, Japan, 2012.
[7] T. Mitsuhashi, Recent progress in SR interferometer, in: IBIC, Tsukuba, Japan, 2012.
[8] N. Milas, Á. Saá Hernández, V. Schlott, A. Streun, Å. Andersson, J. Breunlin, The new SLS beam size monitor, first results, in: IPAC, Shanghai, China, 2013.
[9] V. Schlott, M. Rohrer, Á. Saá Hernández, A. Streun, Å. Andersson, J. Breunlin, N. Milas, Commissioning experience and first results from the new SLS beam size monitor, in: IBIC, Oxford, UK, 2013.
[10] Á. Saá Hernández, A. Masamitsu, M. Böge, N. Milas, M. Rohrer, V. Schlott, A. Streun, Å. Andersson, J. Breunlin, Ultra-low vertical beam size instrumentation and emittance determination at the Swiss Light Source, in: Beam Dynamics Newsletter No. 62, International Committee for Future Accelerators, (Fermilab) Batavia, Illinois, USA, 2013.
[11] P.F. Tavares, S.C. Leemann, M. Sjöström, Å. Andersson, Journal of Synchrotron Radiation 21 (5) (2014) 862.
[12] ⟨https://www.maxlab.lu.se/maxlab/max4/index.html⟩, (accessed 03.08.15).
[13] A. Hansson, E. Wallén, Å. Andersson, Nuclear Instruments and Methods in Physics Research Section A: Accelerators, Spectrometers Detectors and Associated Equipment 671 (0) (2012) 94.
[14] O.V. Chubar, M.M. Samorukov, Technical Report iae-5377/14, 1991.
[15] O.V. Chubar, Resolution improvement in beam profile measurements with synchrotron light, in: IEEE Particle Accelerator Conference, Washington, 1993.
[16] O. Chubar, P. Elleaume, Accurate and efficient computation of synchrotron radiation in the near field region, in: EPAC, Stockholm, Sweden, 1998.
[17] ⟨http://www.esrf.eu/Accelerators/Groups/InsertionDevices/Software/SRW⟩, (accessed 03.08.15).
[18] J. Breunlin, Å. Andersson, Á. Saá Hernández, M. Rohrer, V. Schlott, A. Streun, N. Milas, Status of the new beam size monitor at SLS, in: IPAC, Dresden, Germany, 2014.
[19] T. Naito, M. Tadano, N. Terunuma, J. Urakawa, E. Nakamura, M. Hasumoto, H. Sakai, T. Shibuya, F. Sakai, H. Ohgaki, N. Sei, Nuclear Instruments and Methods in Physics Research Section A: Accelerators, Spectrometers Detectors and Associated Equipment 527 (3) (2004) 624.
[20] J. Safranek, Nuclear Instruments and Methods in Physics Research Section A: Accelerators, Spectrometers Detectors and Associated Equipment 388 (12) (1997) 27.
[21] M. Born, E. Wolf, Principles of Optics, seventh ed., Cambridge University Press, Cambridge, United Kingdom, 1999.
[22] T. Mitsuhashi, Spatial coherency of the synchrotron radiation at the visible light region and its application for the electron beam profile measurement, in: PAC, Vancouver, Canada, 1997.

PAPER IV

Emittance diagnostics at the MAX IV 3 GeV storage ring

J. Breunlin, and Å. Andersson.

In Proceedings of the 7th International Particle Accelerator Conference, IPAC 2016, Busan, Korea. **WEPOW034**, 2908-2910 (2016).

EMITTANCE DIAGNOSTICS AT THE MAX IV 3 GeV STORAGE RING

J. Breunlin*, Å. Andersson, MAX IV Laboratory, Lund University, Sweden

Abstract

With the MAX IV project in Lund, Sweden, an ultralow emittance storage ring light source is going into user operation in 2016. Due to its multibend achromat lattice design the 3 GeV storage ring reaches a horizontal emittance lower than 330 pm rad. Emittance diagnostics will involve two diagnostic beamlines to image the electron beam with infrared and ultraviolet synchrotron radiation from bending dipoles. Placed in locations of different optic functions the beamlines will provide experimental access to both horizontal and vertical emittance and to beam energy spread. Since bunch lengthening with harmonic cavities is essential for machine performance, time resolved measurements with synchrotron radiation for individual longitudinal bunch distributions are of special interest as well.

INTRODUCTION

Visible and near UV synchrotron radiation (SR) can be used to resolve vertical beam sizes at the few µm scale. This has been shown by imaging with π-polarized SR [1] and with the *obstacle diffractometer method* [2] at the Swiss Light source. The MAX IV diagnostic beamlines provide diffraction obstacles as well as double-slits for a direct experimental comparison of the double-slit interferometer [3, 4] and the obstacle diffractometer technique.

Due to the low horizontal emittance the horizontal beam size is 20 to 30 µm at the beamline locations in the MAX IV 3 GeV ring. To resolve such low beam sizes a technique based on imaging with a wide horizontal opening angle and at wavelength in the near IR will be applied.

At present one diagnostic beamline (matching dipole 1 in achromat 20) is under commissioning while the other (unit cell dipole 5 in achromat 2) is delayed due to a mechanical problem with one vacuum chamber. We present the achromat 20 beamline design, measured images of SR in comparison to results from theoretical models and a first estimate of the vertical beam size and emittance.

BEAMLINE DESIGN

The diagnostic beamline images SR from a bending magnet onto a CCD camera. See Fig. 1 for a schematic beamline layout. The bending magnet is the first matching dipole in achromat 20 of the MAX IV 3 GeV storage ring with a dipole field that increases from zero to 0.53 T within the observable range of the beamline (18.5 mrad or 490 mm along the dipole), see Fig. 2.

A thin water-cooled absorber, covering a vertical opening angle of 1.9 mrad, protects the beamline optics from powerful x-ray SR. At low beam currents (<3 mA) this absorber is retractable to allow unaltered imaging of SR. The first

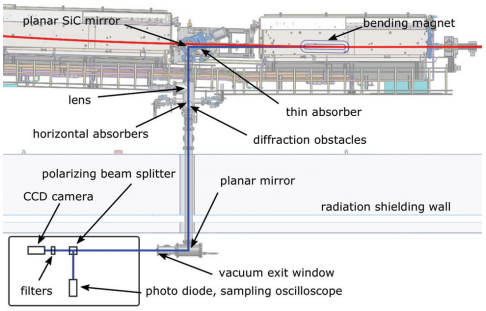

Figure 1: Schematic beamline layout. The electron beam path is indicated in red, the SR path is shown in blue. The distance from the center of the bending magnet to the planar SiC mirror is 1.85 m.

planar mirror, made of silicon carbide, is chamfered and installed in proximity to the electron beam (~1 mm from the electron beam pipe with 20 mm diameter). A second planar mirror outside the radiation shielding wall is required for radiation concerns. The lens (fused silica) is planar-convex with one spherical surface and a diameter of 76 mm. It is placed 2.45 m from the dipole center and images with an optical magnification of −2.18 at a wavelength of 488 nm.

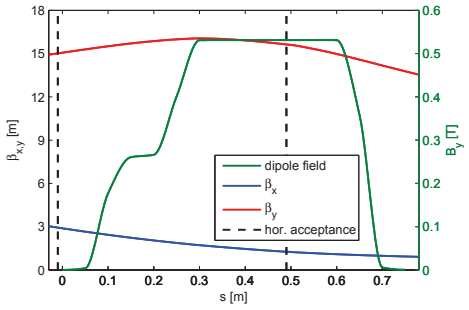

Figure 2: Design beta functions and dipole field strength in the matching dipole. The dashed lines mark the maximum horizontal angular acceptance of the diagnostic beamline.

Two movable horizontal absorbers installed close to the lens define the horizontal opening angle. The vertical acceptance angle of the beamline is limited by the vacuum chamber in the dipole and is ±4.5 mrad. A variety of diffraction obstacles and double-slits can be inserted close to the lens to generate vertical diffraction in a controlled fashion. Special attention has been turned to a solid beamline design

* jonas.breunlin@maxiv.lu.se

ISBN 978-3-95450-147-2

to avoid image blurring from mechanical vibrations during long exposure times.

The beamline front-end outside the radiation shielding holds an optical table with a polarizing beam splitter (Glan-Taylor prism), wavelength filters and the CCD camera. By using the ordinary ray from the polarizer time resolved measurements of SR with a sampling oscilloscope or a photodiode can be done simultaneously to SR imaging.

MODELING THE BEAMLINE

Images of the electron beam with SR in the IR-vis-UV range are highly dominated by effects inherent to SR emission and diffraction. These effects are theoretically predictable and it is thus possible to derive both the horizontal and vertical electron beam sizes from imaged SR. The theoretical calculations were done in the Synchrotron Radiation Workshop (SRW) [5, 6]. SRW is based on near-field calculations and preserves all phase information of the SR witch is emitted by the ultra-relativistic electron beam along its curved trajectory in the bending magnet. The SRW model of our beamline contains the varying bending magnet field as well as relevant optics such as apertures and the lens.

VERTICAL BEAM SIZE MEASUREMENTS

Vertical intensity profiles of imaged π-polarized SR offers vertical beam size resolution by evaluating the intensity ratio of maxima and minima in the diffraction pattern, see [1]. Such a profile is shown in Fig. 3 for an imaging wavelength of 488 nm at 1 nm bandwidth. Since in the present state

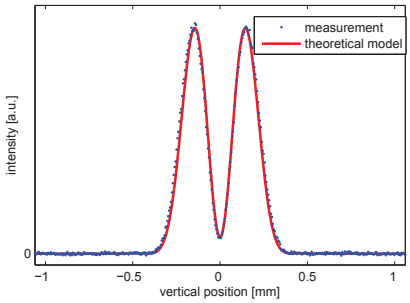

Figure 3: Vertical profile of imaged π-polarized SR at 488 nm wavelength. Measurement (blue dots) and SRW calculation (red lines). The vertical beam size is 11.5 µm.

of the MAX IV 3 GeV storage ring coupling and spurious vertical dispersion are not yet minimized it is not required to image in the near-UV. The diagnostic beamline is, however, prepared for wavelength ranges down to 250 nm in order to resolve vertical beam sizes less than 3 µm.

By introducing diffraction obstacles that cover various vertical angles of the SR (see Fig. 4), complementary measurement methods with a potentially higher sensitivity to the vertical beam size become available [2]. The obstacle heights range from 4.5 mm to 9 mm (from 1.83 mrad to 3.66 mrad vertical angle). A vertical profile measured using the obstacle diffractometer is shown in Fig. 5.

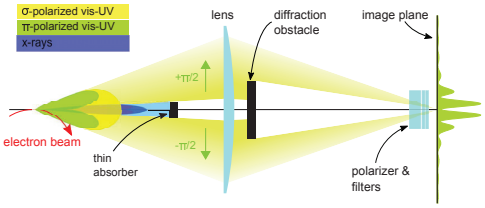

Figure 4: Schematic of the obstacle diffractometer technique.

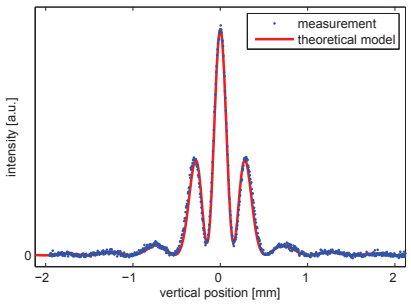

Figure 5: Vertical profile of imaged σ-polarized SR with 5 mm diffraction obstacle at 488 nm wavelength. Measurement (blue dots) and SRW calculation (red lines).

When using a double-slit with a narrow slit widths $2a$ the SR diffraction pattern can be predicted by analytical expressions [2, 4], see Fig. 6. These analytical expressions hold as long as the intensity variation over the slits, originating in the non-isotropic emission of SR, is small. Due to the narrow slits the intensity on the detector is, however, decreased by a factor 5 compared to a diffraction obstacle of same height.

Table 1: Summary of Vertical Beam Size Measurement Results

obstacle height [mm]	σ_y [µm] π-pol.	σ-pol.
-	11.5 ± 0.23	-
4	11.3 ± 0.17	10.5 ± 0.20
5	11.3 ± 0.21	10.7 ± 0.18
6	11.0 ± 0.15	10.7 ± 0.17
9	11.3 ± 0.21	10.6 ± 0.16

The beamsize results achieved with π-polarized imaging and with the obstacle diffractometer methods are shown in Table 1. With the combined result for the vertical beam size of 11.0±0.4 µm combined with beta functions from first

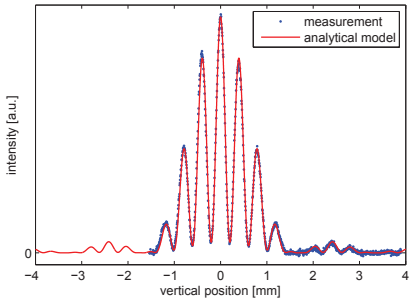

Figure 6: Vertical profile from a double-slit (d = 6.2 mm, $2a$ = 1.5 mm) at 488 nm wavelength. Measurement (blue dots) and analytical calculation (red line). The vertical beam size is 10.5 µm.

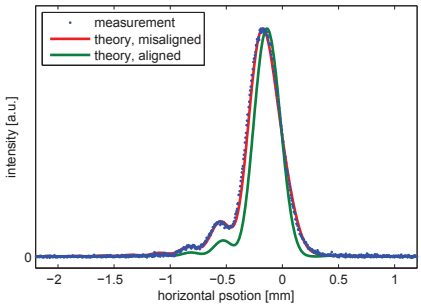

Figure 7: Horizontal profiles of σ-polarized SR at 930 nm for 8.2 mrad horizontal opening angle. The horizontal beam size is 24.5 µm.

attempt LOCO fits in the source point ($\beta_x \approx 2.3$ m and $\beta_y \approx 18$ m) and measured dispersions of ≈ 3 mm in both planes the vertical emittance is 6.4±0.9 pm rad.

HORIZONTAL BEAM SIZE MEASUREMENTS

SR inherent diffraction effects occurring at large horizontal opening angles (>10 mrad) can be used to resolve the horizontal beam size. Since the diffraction pattern is more pronounced at longer wavelengths this requires imaging of SR in the near infrared. At large opening angles the variation of the magnetic field and the beta functions (Fig. 2) need to be taken into account in the theoretical model. Since the edge of the bending magnet is within the horizontal opening angle dipole edge radiation effects can be studied with this beamline. A thorough characterization and theoretical modeling of the electron beam and the diagnostic beamline is, however, required for accurate measurements under these conditions.

Currently the beamline is misaligned by a few mm such that the optical axis of the beamline deviates from SR emission tangent. This has been found by optical alignment and has been modeled in SRW in a basic approach (Fig. 7). Since the misalignment impedes measuring at the full horizontal opening angle it needs to be corrected to achieve sufficient resolution of the horizontal beam size.

BUNCH LENGTH MEASUREMENTS

An optical sampling oscilloscope is used for longitudinal bunch profile measurements. At low currents (no Landau cavity excitation) bunch length from natural energy spread could be verified, see Fig. 8. To verify bunch lengthening and to distinguish it from longitudinal oscillation a single-shot method is required and is planned to be implemented using a fast photo-diode and an oscilloscope.

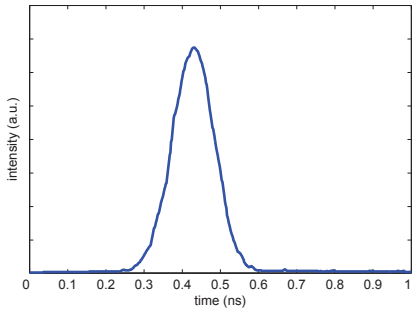

Figure 8: Longitudinal bunch profile measured at <1mA current. The rms bunch length is 55 ps.

REFERENCES

[1] Å. Andersson, M. Böge, A. Lüdeke, V. Schlott, and A. Streun, "Determination of a small vertical electron beam profile and emittance at the Swiss Light Source", *Nucl. Instrum. Meth.*, vol. A591, pp. 437-466, 2008.

[2] J. Breunlin, Å. Andersson, N. Milas, Á. Saá Hernández, and V. Schlott, "Methods for measuring sub-pm rad vertical emittance at the Swiss Light Source", *Nucl. Instrum. Meth.*, vol. A803, pp. 55-64, 2015.

[3] T. Naito and T. Mitsuhashi, "Very small beam-size measurement by a reflective synchrotron radiation interferometer", *Phys. Rev. ST Accel. Beams*, vol. 9, p. 122802, 2006.

[4] T. Mitsuhashi, "Measurement of small transverse beam size using interferometry", in *DIPAC'01*, ESRF, Grenoble, France, May 2001, pp. 26–30 .

[5] O. Chubar and P. Elleaume, "Accurate and efficient computation of synchrotron radiation in the near field region", in *Proc. EPAC'98*, Stockholm, Sweden, Jun. 1998, pp. 1177-1179 .

[6] Synchrotron Radiation Workshop (SRW), Dec. 1997, `http://www.esrf.eu/Accelerators/Groups/InsertionDevices/Software/SRW`

ISBN 978-3-95450-147-2